NASA/CR—2016-219139

A Computationally-Efficient, Multi-Mechanism Based Framework for the Comprehensive Modeling of the Evolutionary Behavior of Shape Memory Alloys

Atef F. Saleeb
The University of Akron, Akron, Ohio

Raj Vaidyanathan
University of Central Florida, Orlando, Florida

November 2016

NASA STI Program . . . in Profile

Since its founding, NASA has been dedicated to the advancement of aeronautics and space science. The NASA Scientific and Technical Information (STI) Program plays a key part in helping NASA maintain this important role.

The NASA STI Program operates under the auspices of the Agency Chief Information Officer. It collects, organizes, provides for archiving, and disseminates NASA's STI. The NASA STI Program provides access to the NASA Technical Report Server—Registered (NTRS Reg) and NASA Technical Report Server—Public (NTRS) thus providing one of the largest collections of aeronautical and space science STI in the world. Results are published in both non-NASA channels and by NASA in the NASA STI Report Series, which includes the following report types:

- TECHNICAL PUBLICATION. Reports of completed research or a major significant phase of research that present the results of NASA programs and include extensive data or theoretical analysis. Includes compilations of significant scientific and technical data and information deemed to be of continuing reference value. NASA counter-part of peer-reviewed formal professional papers, but has less stringent limitations on manuscript length and extent of graphic presentations.
- TECHNICAL MEMORANDUM. Scientific and technical findings that are preliminary or of specialized interest, e.g., “quick-release” reports, working papers, and bibliographies that contain minimal annotation. Does not contain extensive analysis.
- CONTRACTOR REPORT. Scientific and technical findings by NASA-sponsored contractors and grantees.
- CONFERENCE PUBLICATION. Collected papers from scientific and technical conferences, symposia, seminars, or other meetings sponsored or co-sponsored by NASA.
- SPECIAL PUBLICATION. Scientific, technical, or historical information from NASA programs, projects, and missions, often concerned with subjects having substantial public interest.
- TECHNICAL TRANSLATION. English-language translations of foreign scientific and technical material pertinent to NASA's mission.

For more information about the NASA STI program, see the following:

- Access the NASA STI program home page at http://www.sti.nasa.gov
- E-mail your question to help@sti.nasa.gov
- Fax your question to the NASA STI Information Desk at 757-864-6500
- Telephone the NASA STI Information Desk at 757-864-9658
- Write to:
  NASA STI Program
  Mail Stop 148
  NASA Langley Research Center
  Hampton, VA 23681-2199

NASA/CR—2016-219139

A Computationally-Efficient, Multi-Mechanism Based Framework for the Comprehensive Modeling of the Evolutionary Behavior of Shape Memory Alloys

Atef F. Saleeb
The University of Akron, Akron, Ohio

Raj Vaidyanathan
University of Central Florida, Orlando, Florida

Prepared under Grant NNX11AI57A

National Aeronautics and
Space Administration

Glenn Research Center
Cleveland, Ohio 44135

November 2016

Trade names and trademarks are used in this report for identification only. Their usage does not constitute an official endorsement, either expressed or implied, by the National Aeronautics and Space Administration.

Level of Review: This material has been technically reviewed by NASA technical management OR expert reviewer(s).

Available from

NASA STI Program
Mail Stop 148
NASA Langley Research Center
Hampton, VA 23681-2199

National Technical Information Service
5285 Port Royal Road
Springfield, VA 22161
703-605-6000

This report is available in electronic form at http://www.sti.nasa.gov/ and http://ntrs.nasa.gov/

Contents

A Computationally-Efficient, Multi-Mechanism Based Framework for the Comprehensive Modeling of the Evolutionary Behavior of Shape Memory Alloys

Atef F. Saleeb
The University of Akron
Akron, Ohio 44325-3905

Raj Vaidyanathan
University of Central Florida
Orlando, Florida 32816

1.0 Background

The report summarizes the accomplishments made during the 4-year duration of the project. Here, the major emphasis is placed on the different tasks performed by the two research teams; i.e., the modeling activities by the University of Akron (UA) team and the experimental and neutron diffraction studies conducted by the University of Central Florida (UCF) team, during this 4-year period. Further technical details are given in the upcoming sections by UA and UCF for each of the milestones/years (together with the corresponding figures and captions).The project majorly involved the development, validation, and application of a general theoretical model that is capable of capturing the nonlinear hysteretic responses, including pseudoelasticity, shape memory effect, rate-dependency, multi-axiality, asymmetry in tension versus compression response of shape memory alloys. Among the targeted goals for the SMA model was its ability to account for the evolutionary character response (including transient and long term behavior under sustained cycles) for both conventional and high temperature (HT) SMAs, as well as being able to simulate some of the devices which exploit these unique material systems. This required extensive (uni-axial and multi-axial) experiments needed to guide us in calibrating and characterizing the model. Moreover, since the model is formulated on the theoretical notion of internal state variables (ISVs), neutron diffraction experiments were needed to establish the linkage between the micromechanical changes and these ISVs. In addition, the design of the model should allow easy implementation in large scale finite element application to study the behavior of devices making use of these SMA materials under different loading controls. Summary of the activities, progress/achievements made during this period is given below in details for the University of Akron and the University (Section 2.0) of Central Florida (Section 3.0).

2.0 Modeling Activities by UA-Team

This section reports the summary of the activities and achievement made by The University of Akron group during the four year duration of the project. The objectives of the project as stated in the background were:

1. Development of the model
2. Implementation of the model in characterizing different SMA materials
3. Applications of the SMA model in large scale simulations of actuation and other SMA engineering devices
4. Validation of the model.

In addition to the descriptions given in this final report, it should be mentioned that detailed results of many parts of the above activities are documented in two other formats; i.e., (1) published journal papers, conference proceedings and presentations, and (2) Ph.D dissertations of graduate students who participated in project activities. In connection with item (1), the journal papers and conference presentations were produced by various participants in the research project; including work of the PI with two post doctorates (1 year each), two Ph.D graduate students as well as several trained young engineers starting their MS studies in the department of civil engineering at UA. Furthermore with regard to item (2), there are two Ph.D dissertations, one that was completed in Fall of 2013 by Dr. Binod Dhakal and a second that is on-going by Mr. Josiah Sam Owusu-Danquah. Specific references to these publications will be made in the appropriate parts of this report.

2.1 Development of the Mathematical Model

A fully general, three dimensional, constitutive model for Shape Memory Alloys (SMAs), aimed at describing all the salient features of SMA evolutionary response under complex thermomechanical loading conditions was developed during the four year duration of the project. Here, the constructed mathematical model was tested, validated, implemented under different degrees of complexity; uniaxial, multi-axial, proportional, nonproportional, monotonic, cyclic, in conjunction with a wide range of temperature variations. Details of this model formulation and its initial utilization has been given in Saleeb et al., 2011 and was also presented at the Fixed Wing (FW) Fundamental Research Awards Year 1 Review (July, 2012).

The three dimensional model was formulated based on the use of multiple inelastic mechanisms to organize the exchange between the energy stored and energy dissipated during the deformation history of the material. It was based on the well-established mathematical and thermodynamical requirements of convexity, associativity, normality, etc. in formulating the evolution equations governing the model behavior. The two fundamental energy functions used in the model formulation are the Gibb's complementary function, Φ, and dissipation potential, Ω. These thermodynamic/energy functions (stored energy and dissipation) are formulated in terms of the strain-and-stress contributions from each the inelastic mechanisms. These tensorial variables in the model, including the stress tensor, as well as the inelastic strain and internal stress state variables are the key quantities responsible for energy storage-dissipation partitioning that are needed to capture all the unique responses of SMAs. Note that elaborate mathematical equations, assumptions, and tests showing the supermechanical aspects (asymmetry in pseudoelastic and pseudoplastic response in tension and compression, responses in strain/stress-controlled, proportional and nonproportional, multi-axial deformation path tests, major/minor attraction loop character) and supermechanical aspects (One way shape memory behavior (OWSME), Transient response and typical behavior under isobaric tests conditions , evolutionary character under thermomechanical cycling) are presented in Saleeb et al., 2011. For our current utilization of the model, only *six* mechanisms (denoted as "*b*") are used, with *b*=1-3 as the energy *storage* mechanisms, and *b*=4-6 as the energy *dissipative* mechanisms. A summary of how these mechanisms are utilized in a sample material calibration are given in our published papers.

Moreover, in its scheme of application, the model is made general such that the numbers of parameters needed for its utilization are simply classified into (a) *fixed* parameters which are independent on stress/temperature, (b) temperature and/or (c) stress *dependent* parameters. The number of parameters needed for each of these groups depends on the specific material that's being calibrated. Detailed calibration of such materials is given below in the upcoming Section 2.2.

2.2 Material Model Calibration

2.2.1 Shape Memory Alloys

(i) $Ni_{49.9}Ti_{50.1}$ material system

The commercially available binary NiTi alloy which is also designated as 55NiTi (55% Ni by weight in alloy) with at% stoichiometry $Ni_{49.9}Ti_{50.1}$, with fully annealed ingot austenite start temperature A_s of 95 ± 5 °C and an austenite finish temperature (A_f) of 115 °C was among the material systems selected for testing the model capabilities. This material is considered to be one of the *challenging* systems (Manchiraju et al., 2011) for modeling and characterization because of the highly-evolving nature of its response under thermal cycles. Here *isobaric tests* involving extended number of thermal cycles (e.g., 100 cycles or more) under three different deformation modes; i.e., tension (T), compression (C), and shear (S) were needed. However, only extensive *tensile* isobaric test data generated by researchers at GRC were available during this stage of the project.

Specifically, to study the evolutionary character of the 55NiTi material response, isobaric test case of constant tensile engineering stress of 100 MPa with 100 thermal cycles was considered used in the initial evaluation of the fixed parameters. Detailed comparison of the model calibrated response and that of the experiment at the specific 100 MPa stress in Figure 1 shows the evolution of the initial transient response (Cycle 1 to 2) into a more regulated strain evolution (early evolution Cycle 2 to 20 followed by intermediate evolution Cycle 20 to 50), and the final stabilized state (Cycle 50 to 100).

The individual effects in terms of the internal stress components, $\alpha 11$, for each mechanism b =1 to 6 for the simulated isobaric test case under a stress of 100 MPa is also summarized in Figure 2. Here, the variations in the internal stress component, $\alpha 11$, (where 1-1 is the applied stress direction) for each of the six hardening mechanisms during thermal cycling were plotted for 100 cycles in the stress-temperature domain in Figure 2. As can be seen in Figure 2(a), (b), components $\alpha 11$ for the mechanisms 1 and 2 remained always positive in values, experiencing large transient changes in the first two thermal cycles, but with no significant changes during the remaining heat-cool cycles. Note that the response for these two mechanisms does not exhibit hysteresis behavior (i.e., no open-loops) reflecting the energy storing character for these first two hardening mechanisms. On the other hand, with a very high value for the threshold of mechanism 3, the corresponding variation in $\alpha 11$ of this mechanism exhibits an ever-increasing character of evolution with marked hysteresis loops and with a gradually-reducing rate of evolution in the later thermal cycles (Figure 2(c)). In contrast, dissipative mechanisms 4, 5 and 6 evolve with both positive and negative values during the thermal cycling to regulate the evolutionary strain response (Figure 2(d), (e), and (f)). Note the reversal in the direction of the evolution in these three mechanisms as indicated by the arrows in the corresponding figures.

The resulting calibrated model was utilized to simulate the material evolutionary response in the remaining *six* different isobaric tension tests conducted at 10, 50, 80, 150, 200, and 300 MPa, with 100 thermal cycles for each (except in the 200 MPa case where test data was available for only 88 cycles). These experimental tests were provided by the NASA Glenn Research Center team. All the thermal cycles in the tests were performed between 30 and 165 °C. The resulting figures are shown in Figure 3 and Figure 4, which highlight some of the major *accomplishment*s in model calibration of the 55NiTi material. The variation of open-loop strain (ε_{OLS}), actuation strain (ε_{ACT}) with cycles at constant engineering "isobaric" at 100 MPa stress level are shown in Figure 1(c) to (d). From both the qualitative and quantitative viewpoints, the above results clearly demonstrated that the following important experimental characteristics of the evolutionary cyclic response of 55NiTi material were successfully captured by the SMA model:

1. Transient Response:
    - A small increase in strain during the loading to a constant engineering stress level at constant temperature.
    - A significant transient change during the cooling branch of the first thermal cycle at constant stress.
    - A significant drop in strain during heating branch in the second thermal cycle at constant stress.

2. Stages of Evolutionary Response with diminishing rates of evolution:
    - Early Evolution (Cycle 2 to 20)
    - Intermediate Evolution (Cycle 20 to 50)
    - Evolution towards a “nearly” saturated/attraction state (Cycle 50 to 100)

The details regarding the calibration of this material was presented at the 2012 ASME conference and also published in scientific research journals (see Saleeb et. al., 2013a, b, and Padula et al., 2014) as well in the Ph.D dissertation of Dr. Binod Dhakal.

(ii) $Ni_{50.3}Ti_{29.7}Hf_{20}$ material system

Different from the 55NiTi counterpart, the NiTiHf material system which is used in high temperature applications (due to its higher transformation temperatures, i.e., above 100 °C) showed lesser evolutionary pattern. Here, two sets (Set 1 and Set 2) of experimental results were received from NASA Glenn Research Center team for a $Ni_{50.3}Ti_{29.7}Hf_{20}$ material which was heat treated by ageing at 550 °C for 3 hours. The first set included series of test showing changes in bias stress in tension from 100 to 500 MPa with 100 MPa increments followed by compression from –100 to –500 MPa with –100 MPa increments, in a temperature range from 30 to 300 °C (see Figure 5(a)). The second set of experiment included tension isobaric tests on virgin materials at 80, 150, and 200 MPa in extended thermal cycles (100 cycles) in a range of temperature from 30 to 300 °C (see Figure 6(a), (c), (e)). From the result of experimental test Set 1, it was evident that the $Ni_{50.3}Ti_{29.7}Hf_{20}$ alloy exhibits a strong asymmetry under tensile and compressive load-biased thermal cycling. Moreover, the transformation temperatures (M_s, M_f, A_s, A_f) in $Ni_{50.3}Ti_{29.7}Hf_{20}$ shifted towards the higher temperature side with increase in bias stress. From the results of Set 2, the $Ni_{50.3}Ti_{29.7}Hf_{20}$ alloy showed much less strain evolution during the 100 thermal cycles in comparison to the 55NiTi counterpart. We made use of the same formulated SMA model which was used previously to characterize $Ni_{49.9}Ti_{50.1}$ material. Three features which served as a benchmark in the calibration of the model for this material were,

- Remarkable effect of stress magnitude on the corresponding transformation (actuation) strain.
- Marked tension/compression asymmetry (ATC) in the response.
- Significant transient evolution, but small sustained strain evolution, in repeated thermal cycles.

Details of this calibration are also published in Saleeb et al., 2015a. A comparison of the model results with that of the experiment is shown in Figure 5 (Experimental: parts (a) and (c) and SMA Model: parts (b) and (d)). As seen in the figure, the SMA model was able to predict the ATC effect in strain at martensite and austenite as well as the actuation strain for the 2nd thermal cycle at different bias stresses in the series isobaric test. Similar comparisons of the individual isobaric test result from our SMA Model results with the experimental measurements for stress levels of 80, 150, and 200 MPa are also shown in Figure 6 (Experimental: parts (a), (c) and (e) and SMA Model: parts (b), (d) and (f)), respectively.

In addition, the calibrated model and its parameters were also able to capture the behavior of this material at higher levels of stresses. In particular, the 3-D SMA model was used to simulate the experimental tests reported in Benafan et al. 2014, on this same $Ni_{50.3}Ti_{29.7}Hf_{20}$ (but with different heat and aging treatment). Detail results from this calibration exercise were given in the final report of Year 3 as well as at Fixed Wing (FW) Fundamental Research Awards Year 3 Review. Figure 7 and Figure 8 shows such comparisons between the experimental and model simulated –100 to –200 to –0 MPa series test response and –700 MPa, 0 MPa test, respectively. From all these results, we can see that the model was able to capture the experimentally-observed dimensional stability in the $Ni_{50.3}Ti_{29.7}Hf_{20}$ material.

2.2.2 Superelastic Alloys

(iii) A powder metallurgical processed NiTi (PM/NiTi-P) SMA material system

The experimental test results of this specific material system were taken from a powder metallurgically processed material which contains pre-alloyed *NiTi* powder (54.6 wt %Ni and 45.4 wt. %Ti), with two polymer additives; i.e., amide wax and a polyethylene wax (68, 19, and 13 vol%, respectively) (Krone et al., 2005; Christ and Reese, 2009). The details of this material, including its transformation temperatures are stated in above cited references (Krone et al., 2005; Christ and Reese, 2009).The isothermal stress-strain measurements at three different temperatures (–48, 13, 37 °C) were used for the model calibration. This included two load-unload tension tests which were conducted under combined control (strain control to 4% during loading, and stress control to zero stress during unloading) at –48 and 37 °C (Figure 9). In addition, a set of strain-controlled tension tests were conducted to 5% strain without unloading at 13 °C as shown in Figure 9 were used.

The SMA model was utilized to characterize the pseudoplastic and pseudoelastic experimental response of this material system. The stress-strain curves comparing the experimental result (in symbols) with the model prediction (in solid line) are superimposed in Figure 9 to better analyze the model’s capabilities. Qualitatively, the results show that the calibrated model simulation successfully predicted each stress-strain response of the material at all the three selected temperatures with negligible differences. The superelastic response at 37 °C, the end of the loading stage differs by only 3 MPa. For the psuedoplastic case (–48 °C), the end of the loading and unloading branches were captured perfectly by the model, indicating a significant residual strain (3.61%) after unloading. It is interesting to note that in the experiments conducted to 5% strain for the 13 °C case, the material demonstrates a rehardening behavior which is also well captured. See Saleeb et al., 2015a for details.

(iv) $Ni_{50.7}Ti_{49.3}$ SMA material system

A $Ni_{50.7}Ti_{49.3}$ (at.%) SMA material (also termed SE 508) was selected to investigate the superelastic SMA behavior, which is considered appropriate for biomedical applications such as self-expanding stents. The experimental test results of the commercially available superelastic $Ni_{50.7}Ti_{49.3}$ alloy (at.%) medical grade *wire* with a diameter of 0.5 mm were taken from Liu et al., 2008. The austenite finish (A_f) temperature for this material is 19 °C (lower than body temperature) as measured using differential scanning calorimetry (DSC) under a stress-free condition.

Figure 10 shows the experimental stress-strain response (in symbols) for the $Ni_{50.7}Ti_{49.3}$ (at.%) sample under tensile loading. The calibrated model response for this superelastic material was done based on the simple experimental test results described in the above reference (Liu et al., 2008). The stress-strain curves comparing the experimental result (in symbols) with the model prediction (in solid line) are superimposed in Figure 10 to better analyze the model`s capabilities. Qualitatively, there is a good agreement between the experimental result and model counterpart. From the quantitative viewpoint, the model successfully captured the initial steep increase in stress during the initial 0.8% strain increment (path ‘1’-‘2’) as well as the onset of the stress plateau at 500 MPa (path ‘2’-‘3’). Indeed, almost all of the loading curve (path ‘1’-‘2’-‘3’) lies directly on top of the experimental data, with only a 16 MPa difference at the end of the load-up. In the unloading branch, the rapid decrease in stress over the first 0.5% unloading strain (path ‘3’-‘4’) was also captured reasonably well. However, the lower stress plateau region (path ‘4’-‘5’) showed a gradual decrease until 200 MPa whereas the experimental curve exhibited a constant stress (250 MPa) until 0.5% strain. Lastly, the final unloading branch (path ‘5’-‘6’) was captured with nearly complete strain recovery of almost 0.05%. Hence, despite a slight deviation in the unloading branch ‘5’-‘6’, the model was capable of accurately capturing the superelastic behavior of the $Ni_{50.7}Ti_{49.3}$ (at. %).

2.2.3 Accomplishments in Streamlining the Model Calibration

Considering the details of the parameterization/calibration exercise for the four different classes of the SMA materials ($Ni_{49.9}Ti_{50.1}$, $Ni_{50.3}Ti_{29.7}Hf_{20}$, PM/NiTi-P, and superelastic $Ni_{50.7}Ti_{49.3}$ utilized above in Section 2.0) it is worth mentioning that although these material systems had different characteristics, the model was well able to capture their individual responses. Here, the degree of *complexity* of the calibration procedure depended upon the number and details of the experimental responses available and/or required for the SMA material. For example, the parameterization of the superelastic NiTi which is targeted for biomedical stent application was much simpler in contrast to that of the far more difficult cases involving NiTi-based actuation materials. Also, the key modeling ingredient in providing such calibration *flexibility* for the different SMA systems is the convenient *grouping* of the material parameters into the *fixed* set (17 parameters) and the *functionally*-(temperature/stress) dependent set (maximum of 8 parameters) as shown in Table 1. The degree of temperature and/or stress-state dependency to be utilized for these latter 8 material parameters determines the *complexity* of the parameterization. Details procedure for calibrating these four different materials is presented in our recent paper, Saleeb et al., 2015a.

2.3 Assessing Model Predictive Capabilities—From Isothermal Characterization to Prediction of Shape Memory and Stress Relaxation Behavior

The SMA model calibrated for the PM/NiTi-P SMA material (described in the previous section) was used to predict the well-known shape memory behavior, the experimentally observed observed stress relaxation and isostrain responses. The simulated/predicted thermomechanical responses are discussed below.

(i) Prediction of shape memory cyclic behavior

Here, the SMA Model calibrated on the basis of the few given isothermals test results for the PM-NiTi-P material (see description in Section 2.0) was exploited to predict the isobaric/shape memory test responses. The material specimen was loaded to a bias-stress level at UCT = 90 °C and then thermally cycled between LCT = –50 °C and UCT=90 °C for 10 thermal cycles. The bias-stress levels studied here were 50, 100, 150, 200, 300, 400, and 500 MPa. The strain versus temperature response for the isobaric tests at bias stress levels of 100, 150, 200, 300, 400, and 500 MPa are shown in Figure 11(a) to (f). At all the bias-stress levels, the basic SMA features, i.e., the transient behavior followed by generation of a significant strain in the subsequent first cooling, which is recovered in the following heating branch are exhibited. The evolution of strain was observed at both the LCT and UCT with thermal cycles. Moreover, the actuation strain increases with increasing level of bias-stress, with the maximum actuation strain attained at the 400 MPa stress level, after which there’s no significant difference in the actuation strain for the subsequent stress levels. Also as seen in the plot of Figure 11, we observed *shifting* of the transformation region (towards the higher temperature) with increasing bias-stress levels. This behavior has been observed in the isobaric tests of high-temperature $Ni_{50.3}Ti_{29.7}Hf_{20}$ actuation materials (Bigelow et al., 2011).

(ii) Prediction of isostrain thermal cyclic behavior

The SMA Model calibrated for the PM-NiTi-P materials on the basis of the isothermals test results was also exploited to predict the isostrain test responses. Two different ways were considered in holding the strain constant during thermal cycles. In the first case, the specimen was loaded in the strain-controlled mode at LCT = –50 °C (pseudoplastic state) whilst in the second case, the specimen is loaded in any stress- and/or strain-controlled mode at LCT = –50 °C (pseudoplastic) till the significant stress/strain is reached, then the specimen in unloaded to zero stress in stress-controlled mode. There is a significant value of residual strain due to the pseudoplastic response of the material at -50 °C. This value of residual strain is held constant and the thermal cycles are performed. The latter case is also termed as constrained-recovery thermal cycling.

The bias-strain levels studied here were 0.25, 0.5, 0.75, 1, 1.5, 2, 3, 4, and 5%. The stress versus temperature responses are shown in Figure 12(a) to (i) for the isostrain thermal cycles (i.e., case 1) at the different bias strains and Figure 13(c) for the second case, respectively. The details of the thermomechanical processes for the constrained recovery thermal cycling (second case) are depicted in Figure 13(a) and (c). See the second quarter of Year 4 report for the additional detail regarding this study.

(iii) Prediction of the stress relaxation and inverse-relaxation behavior

Here, the responses of SMAs under sustained loading conditions involving material creep, relaxation, etc., which have been observed experimentally for various equi-atomic NiTi SMA Materials was investigated. In particular, Figure 14(a) to (c) show the experimental evidence for such time-dependent response as reported by Helm (2001). It clearly shows the periods of relaxation under constant strain, at both high temperature above A_f (Figure 14(a)), and low temperature below M_f (Figure 14(b)) for the NiTi alloy. The counterpart creep behavior during periods of constant stress at low temperature is also shown in Figure 14(c).

The model responses of the calibrated PM/NiTi-P material was first studied in uniaxial, strain-controlled (strain rate=1×10^{-4}/s), isothermal, tension tests at temperatures higher than Af and lower than Mf, with multiple periods (of 3-hr duration each) during which the strains are held constant, during both the loading and unloading branches of the test. The model results are shown in Figure 14(d) (with strain holding at 1, 2, and 3%), and Figure 14(e) (with strain holding at 0.5, 1.5, 2.5, and 3.5%), respectively. These model responses during the loading branches in both tests performed at T=37 °C (>A_f) and at T = –48 °C (<M_f) exhibit the “conventional” phenomena of stress relaxation where the magnitude of tensile stress decreases during the periods of constant strain. This is in conformity with the experimental evidence indicated in Figure 15(a) and (b). On the other hand, there is a significant difference in the character of the stress changes occurring during the strain-hold periods along the unloading branch of the test at high temperature (T = 37 °C), where an *inverse-relaxation* phenomena occurs resulting in an increase in the magnitude of the tensile stress at the periods of strain-holds. This is also in agreement with the counterpart experimental result shown in Figure 15(a). Finally, the model simulation for stress-controlled (stress rate=0.125 MPa/s), tensile test conducted at low temperature, T=–48 °C, with multiple periods of stress-holds (at stress values of 100, 150, 200, and 225 MPa) shows the conventional creep phenomena resulting in an increase in the tensile strain magnitude during stress-hold periods. This behavior is also supported by the experimental evidence in Figure 15(c). Details of this investigation have been presented in our recently published paper, Saleeb et al., 2015b.

2.4 Large-Scale Simulation of SMA Structures

After detail study into the above mentioned materials, we began to simulate different shape memory alloy (SMA) actuator geometries which are likely to operate under a large number of thermo-mechanical cycles. To this end, our calibrated SMA model was implemented for the large scale simulation of actuation and biomedical devices.

2.4.1 Actuation Devices

(i) Helical spring actuator

A four four-coil helical spring actuator was simulated using the SMA multi-mechanism framework calibrated for $Ni_{49.9}Ti_{50.1}$. The SMA helical spring geometry and dimensional details shown in Figure 15 was used for this purpose. One end of the spring was fixed against rotation and translation whereas the other end was made free (hence allowing translations and rotations degrees of freedom). The free end was subjected to an axial *force* of 3.373 N at room temperature, to produce an average value of approximately 50 MPa for the distribution of effective stresses ($\sqrt{3 s_{ij} s_{ij} / 2}$, where s_{ij} is the stress deviator tensor) in the SMA coils. At the constant load of 3.373 N, 25 thermal cycles here were performed between the room temperature of 30 °C (LCT, lower-cycle temperature) and 165 °C (UCT, upper-cycle temperature). This simulation procedure has been elaborated in Saleeb et al., 2013c.

In particular, a significant *spatial variation* (ranging from 3 to 68 MPa) was observed in the effective stress distribution (i.e., stress-state "intensity") as can be clearly observed in Figure 15(b) and (c). High magnitudes of stresses were observed in all six stress components along the length and sections of the coils, having different signs for some of these components. In Figure 15(d) and (e), the evolutionary response of the (primary) axial displacement (δ), as well as the (secondary) twist angle θ (rotation about axis of helix), respectively, were plotted during the thermal cycles. Here, we observed the very neat and logical correspondence in the evolutionary character of the "global" axial-displacement results in this section (see Figure 15(d) for axial displacement (δ) versus temperature plot) and their "material-point" counterparts depicted in Figure 1. There was also a secondary response (i.e., angle of twist, θ, at free end) observed in the helical-coil structure. In particular, referring to Figure 15(e), the angle of twist increased significantly, reaching a magnitude of approximately –31° and 9°, at the martesite and austenite sides, respectively, by the end of the 25th thermal cycle).

(ii) Tube actuators

The large-scale simulation of a tubular actuator was studied, utilizing the two different actuation materials; namely $Ni_{49.9}Ti_{50.1}$ (55NiTi) and a high-temperature $Ni_{50.3}Ti_{49.7}Hf_{20}$. Here the SMA model, calibrated for the $Ni_{49.9}Ti_{50.1}$ material system and the $Ni_{50.3}Ti_{49.7}Hf_{20}$ (Extrusion-124) material was used for the finite element analysis of the actuators. See Figure 16 for the geometrical details of the tube. The iso-axial force and isotorque loading conditions under 50 thermal cycles (see Figure 17) were considered in each SMA tube. Details of qualitative and quantitative comparison (i.e., the similarities and differences) in the cyclic deformation response of the $Ni_{49.9}Ti_{50.1}$ and $Ni_{50.3}Ti_{49.7}Hf_{20}$ SMA tube actuators, under the different mechanical (axial tensile/compressive, torque) loading conditions, was presented at the Fixed Wing (FW) Fundamental Research Awards Year 3 Review, and have also been published in Owusu-Danquah et al., 2015.

The tube actuator was analyzed under the individual stress states of (i) tension (by applying tensile force), (ii) compression (by applying compressive force) and (iii) shear (by applying torque) in the thin SMA tube (see Figure 17(a) for magnitude of stresses). The state of stresses in the $Ni_{49.9}Ti_{50.1}$ and $Ni_{50.3}Ti_{29.7}Hf_{20}$ tube actuators at the end of load-up under the isotorque loading condition is shown in

Figure 18(a) and (b), respectively. Here, we observe very small non homogeneity (i.e., about 8 % in the $Ni_{49.9}Ti_{50.1}$ tube and 10 % in the $Ni_{50.3}Ti_{29.7}Hf_{20}$ tube) in the distribution of effective stresses across the section of the two SMA tube actuators.

The comparison of the variation of the axial displacement with time and temperature as well as the actuation displacements for the $Ni_{49.9}Ti_{50.1}$ and $Ni_{50.3}Ti_{29.7}Hf_{20}$ tube actuators, under the tensile and compressive forces are shown in Figure 19 and Figure 20, respectively. Similar to the isoforce loading cases, the plots of angle of twist versus time and angle of twist versus temperature (Figure 21) show the initial transient and evolutionary response during the thermal cycles in both the $Ni_{49.9}Ti_{50.1}$ and the $Ni_{50.3}Ti_{29.7}Hf_{20}$ tube actuator. Note that additional study involving these same materials but with different actuations configurations (tubes, and solid bars) were presented in the second quarter report of Year 4. In view of the results obtained from this study, the following conclusions were made:

a. Each of the two SMA material tube actuators under the inhomogeneous state of stress exhibited similar pattern of cyclic deformation with respect to their simple homogeneous isobaric uniaxial experimental tests which were used in calibration the material parameters of the theoretical model.
b. The $Ni_{49.9}Ti_{50.1}$ tube was able to produce more axial and angular actuation strokes with less energy input (i.e., using less mechanical force and lesser upper cycle temperature) than its $Ni_{50.3}Ti_{29.7}Hf_{20}$ counterpart. On the other hand, the $Ni_{50.3}Ti_{29.7}Hf_{20}$ appears to be far more dimensionally stable in all cases of pure-mode (i.e., tension/compression or torsion) loading. As a consequence of its improved dimensional stability, the $Ni_{50.3}Ti_{29.7}Hf_{20}$ will certainly provide some benefits over the $Ni_{49.9}Ti_{50.1}$ material in actuation systems where space limitations and weight considerations are important in a given tube actuator design.
c. The amount of actuation stroke and the dimensional stability of the actuator during thermal cycles (i.e., heating and cooling) significantly depend on the selected SMA material system as well as the applied load mode (tension, compression or torque).
d. Under the applied isotorque loading condition, both SMA tubes produced a secondary “axial displacement” deformation response which is relatively insignificant with respect to the primary “angle of twist” response (see Figure 22).

(iii) Wave spring actuator

The SMA material model was also used to investigate the effect of the interaction between the 55NiTi material’s evolutionary response and a wave spring’s geometric features (i.e., bending-to-membrane transition in the structural response as the geometry of the wave spring changes during thermal cycling). This proved practically very significant in providing an effective means to limit the dimensional instability of the 55NiTi actuator. The geometrical details of the wave spring utilized are shown in Figure 23. The base end of the wave spring was fixed to all active degree of freedom, where on the top end, a surface traction of 0.25 N/mm^2 (load equivalent to 2.4 N) is applied at 30 °C. The load is kept constant during the 25 thermal cycles performed between LCT=30 °C and UCT=165 °C, thus this test can be seen as an isoforce thermal cycling, despite the isobaric (constant stress) tests which were utilized to calibrate the SMA model. A mesh containing a total of 2515 elements of the type C3D20R (quadratic, 20-noded, three-dimensional, brick) was used for this simulation. To study the effect of the wave spring’s geometric constraints, the load-deflection analysis was performed, considering an elastic material of E=60,000 MPa (similar as 55NiTi). As can be seen in Figure 24a, initially the force required to deform the wave spring is small which increases rapidly with time; showing the rehardening nature with the increase in the displacement. This indicates the transition between the bending-membrane interaction in the wave collar geometry, as demonstrated by the variation of maximum and minimum principal stress at a generic element in the wave collar, with the applied displacement. See the contour in Figure 25 for the variation of the bending stresses, S11. All the details for this study were presented in the first quarter report of Year-4.

In order to study the effect of geometric configuration on the dimensional stability of the 55NiTi, the evolutionary deformation response (for 25 thermal cycles) obtained from the current wave spring actuator is compared with that from the torque tube actuator described earlier. The displacement response from both actuators is normalized with respect to their respective reading obtained at the end of the 1st cooling branch. As can be seen in Figure 26 the displacement evolved by 75% for torque tube actuator in contrast to 50% for wave spring actuator, based upon the value obtained at the end of 1st cooling branch in each case. This particular study led to the following remarks:

a. Despite its highly evolving character under simple modes of loading (such as in wires and torque tubes), the 55NiTi material will be exhibiting far *improved* dimensional stability characteristics when used in wave springs undergoing “bending-to-membrane” mode conversion.
b. As a corollary to above item, this study opens the door for the exploring further the possibility of taking advantage of the variation in the geometric constraints of the actuator to enhance the cyclic dimensional stability of the binary 55NiTi.

(iv) SMA/PMC composite

The excellent strength properties of PMCs are one of the major reasons for their use in the aerospace industry. In our use of the SMA model here, we investigated the interaction effects of an embedded SMA plate on the host PMC. Different SMA/PMC composite layup configurations/architecture was considered. Figure 27 shows the geometrical details of the reference architecture. It is seen that the actuation capability of the SMA/PMC composite is affected by the directions/arrangement of the individual layers constituting the panel. In particular, the less stiff layup is able to generate more actuation stroke than the very stiff case (see Figure 28). Moreover, it is seen that the host material (PMC) has significant effect on the constitutive response of the embedded SMA and vice-versa. In particular, the PMC forces the SMA to actuate under variable stress whilst the SMA on the other hand forces the elastic PMC to evolve (see Figure 29 for the variation of bending stresses with temperature for each material layer). The presence of the PMC laminates helped to reduce the evolutionary behavior of the NiTi SMA system (see Figure 30(c)). Understanding these interactions is critical for tailoring desired SMA/PMC composite behavior for effective utilization. For details see the Fixed Wing (FW) Fundamental Research Awards Year 3 Review presentation by this group.

2.4.2 Biomedical Devices

(v) Simulation of the PM/NiTi-P bone staple

The shape memory effect in the PM/NiTi-P SMA material presented in previous Sections 2.0 and 3.0 were used this biomedical application. Our study involved, the initial phase of deforming the staple in the martensite state (–48 °C in the experiment of Krone et al., 2005) and the subsequent development of a large clamping force when the staple legs come into contact with the bone surfaces. Next to this, we assessed the post-surgical performance of the SMA staple. The overall chart of this procedure is shown in Figure 31. The geometrical details of the staple and the bone are shown in Figure 32(a) and (b), respectively. The stages involved in the procedure are summarized in Figure 32(d). All the simulation details can be found in our recent publication Saleeb et al., 2015b.

Here, assessing the clamping force produced by the bone staple using this mathematical model was the key factor in this investigation. As a measure of the effectiveness of this surgical procedure in generating significant forces, the results from the constrained recovery/actual case (stages i-ii-iii-iv-v) is compared with that of the free recovery (stages i-ii-iii-iv-v') case where the SMA staple was allowed to freely recover all the deformations fully. As the developed stress and strain in the NiTi SMA staple occur primarily in the base of the staple, data was taken from point 'C' (Figure 32(a)) which is located at the top of the staple base 1.9 mm from the centerline. When the uniformly distributed force is applied to the inside surface of the staple legs, the staple base bends easily allowing the staple legs to separate. The stress in the material increases gradually with the strain, then plateau just past 150 MPa, peaking at 194 MPa (2.9% strain) at the end of loading as is characteristic of the psuedoplastic behavior. Upon unloading, there is a slight strain recovery consistent with the strain recovery observed upon unloading in the experimental results (Krone et al., 2005) (compare Figure 11 with Figure 27(b)).

In the next step, the staple is heated to body temperature transforming back to the austenite state from the martensite state and initiating the one-way shape memory effect in the NiTi. The development of the stresses in the bone and staple during this period of heating is depicted in Figure 33. In the "free OWSME" case the staple returns to its original shape (almost all strains are recovered) and the stress in the staple base diminishes. In contrast when the staple is restricted by the bone ("constrained OWSME"), a complete shape (strain) recovery is no longer possible causing a marked increase in stress as seen in Figure 34. This sharp rise in stress translates into the compressive clamping force as the staple clinches into the bone segment. The detailed characterization of the material model, as well as its implementation in assessing the immediate and post-surgical performance of the staple has been given in our published journal, Saleeb et al., 2015b. Amongst the conclusions gathered from this investigation are:

a. Despite the simplicity of the test data used in its calibration, the present SMA material model was able to handle the rather complex conditions involved in simulating the stapling procedure to mimic the actual operational environment.
b. It was found that adequate compressive forces were developed by the PM/NiTi-P bone staple, with the tendency of this force to even increase under sustained thermal loading due to the intrinsic "inverse relaxation phenomena" in the SMA material.
c. The simulation results correlated well with those from experimental measurements.
d. The body-temperature-activated PM/NiTi-P staple was proved to be clinically viable, providing a stable clamping force needed for speedy coaptation of the fractured bones.
e. These realistic assessments of the clinical performance of the SMA staple crucially depend on the use of mathematical SMA material models that are sufficiently accurate and comprehensive in scope to capture the experimentally-observed behavior; i.e., to simultaneously capture the three important characteristics of superelasticity, shape memory effect, and inverse-relaxation due to the time-dependent nature of the material response.

(vi) Simulation of superelastic Ni50.7Ti49.3 self-expanding stent

The calibration of the test results for the biocompatible superelastic $Ni_{50.7}Ti_{49.3}$ SMA material was used for a self-expanding stent application. Considering that a stent is simply a scaffolding for the vessel, providing a mechanical support to a biological tissue (Sigwart, 1997), the mechanical performance of the material at body temperature is critical to the proper design of the device (Xia et al., 2007). Understanding how stresses will form in the stent structure, as well as the host tissue, under the effect of the oscillatory (systolic/diastolic) pressure cycles, and how to mitigate them becomes the key to optimizing the SMA stent designs. A tubular, honeycomb patterned stent geometry was chosen for the large scale simulation (see Figure 35 for the dimensional details). Two alternative routes were taken during the simulation of the different important stages of the stenting procedure (see Figure 36).

More specifically, the first one is related to the crushing/crimping of the memory stent configuration at the superelastic (SE) regime of the SMA material i.e., at temperature higher than the characteristic austenite finish (Af) temperature. This is then followed by the deployment of the crushed stent inside the artery while maintaining the crimping force. Afterwards, the crimped stent is activated/released inside the diseased artery (host tissue) to re-expand against the impediment of the vessel wall (thus establishing contact interaction between the stent and host tissue). The final state of self-expansion of the stent will result in the increase of the clear opening of the clogged/blocked artery. See Figure 37 for the variation of axial force with the stent diameter for this specific case.

In contrast, the second scheme for the stenting procedure utilizes the shape memory effect (SME) of the SMA material. In this case, the initial memory configuration of the stent (to which the material will try to return upon activation) exists at a temperature lower than the characteristic martensite finish (Mf) temperature. The crushing of the stent at this low temperature is achieved mechanically and the crimping force is immediately released (thus, causing small “elastic” rebound/spring-back/recoil) at this same low temperature. The crushed stent is then delivered to the diseased artery region and its self-expansion stage is activated by the shape memory effect occurring in the SMA material due to the gradual increase in temperature of the stent to attain the body temperature.

The long-term performance of these stents inside the diseased artery measured in terms of vessel patency/restenosis and the mechanical characteristics of the device (Tan et al., 2001) were investigated for the two schemes. Desisting from all the simulations details, readers are referred an elaborate discussion; including mesh convergence, loading scenarios and results in Saleeb et al., 2015c. Here, our target was determining which of these alternative schemes proved to be more clinically viable in reducing a plaque occluded artery. The following remarks were made from this investigation:

a. The SMA model calibrated for simple, uniaxial, tensile isothermal tests was successfully implemented in the large-scale boundary value problem of the surgical stenting procedure involving complex stent geometry, large displacements and rotations, contact interactions, cyclic thermomechanical loadings, etc.
b. The stent programmed memory configuration was more-favorably crimped with lesser force to a higher crushing ratio in the thermal activation scheme compared to its mechanical counterpart.
c. At the end of the activation stage in the stenting procedure, for an initial stenosis of 60% blockage, the vessel blockage is reduced to ~18% in the mechanical activation case and ~15% in the thermal counterpart.
d. The thermal activation protocol showed a more favorable stress distribution in the host tissue, which directly translates into an important clinical performance index (i.e., patient comfort) in the stenting surgery.
e. The use of the present SMA model in simulating NiTinol self-expanding stenting surgeries has provided important information that are extremely difficult to obtain from the physical experiments. This indicates the great potential of utilizing such material models as a tool to ultimately optimize the procedural controls and clinical forces in other SMA medical devices.
f. There is no indication of any detrimental functional fatigue/degradation in the cured stenotic artery during cyclic pressure oscillations.

2.5 Experimental Validation of the SMA Model Using the $Ni_{49.9}Ti_{50.1}$(at.%) Helical-Coil Actuator

The calibrated model for the $Ni_{49.9}Ti_{50.1}$ material system was successfully implemented in the large scale simulation of a helical spring actuator (Saleeb et al.2013c). Here, an experimental study was carried on a helical spring actuator at the University of Central Florida using $Ni_{49.9}Ti_{50.1}$ (at.%) wires supplied by Dr. Santo A. Padula II (NASA-GRC) to validate the simulated test results. The helical spring used in the simulation had a spring index $(I = D_m/d)$ of 10.7, an initial pitch angle of 4.7° (pitch height, P = 6 mm) and 3 active coils. Where the mean coil diameter D_m = 23.1 mm and wire diameter d = 2.16 mm, as shown in Figure 38. For the purpose of modeling and finite element discretization, we used ABAQUS standard program (ABAQUS, 2012), in which the calibrated SMA multi-mechanism model for the $Ni_{49.9}Ti_{50.1}$ (at.%) material system was implemented through a UMAT routine.

The computational model of the helical-coil was created based on the three-dimensional theory of *continuum* mechanics. This proved convenient in handling all the stress *multi-axiality* effects anticipated in the use of the helical structure during the thermal actuation cycles under the bias axial load. The boundary conditions were made to ensure that *three* coils remained active to contribute in actuation, approximately similar to the experimental conditions. An axial load of 8.8 N was estimated analytically (using methodology presented in Ancker and Goodier, 1958) to be applied at the reference point at 30°C to produce a maximum effective stress magnitude of approximately 100 MPa in the coils. The applied axial load was kept constant while performing a single thermal cycle (henceforth referred to isoforce) in the temperature range of 30 and 165 °C (spanning the whole transformation temperature regime of the present 55NiTi material). Also, here, the axial displacement produced during the isoforce thermal cycling test was measured as the primary deformation response. Two cases of end boundary conditions were implemented at the reference point in the loading end with respect to the experiments: Case (1) the loading end is *restrained* against twist, and Case (2) the loading end is *free* to twist.

The simulation for both boundary condition Cases (1) and (2) showed that the axially applied load of 8.8 N at 30 °C produced an estimated effective stress of around 100 MPa. The effective stress and six individual stress components (three normal and three shear stresses) at the end of load-up for Case (1) boundary condition are shown in Figure 39. Note that the two different cases led to the *same* variation (within error) in magnitude of the effective stress, thus only Case (1) was shown. There was a significant *spatial variation* of the effective stress distribution (i.e., stress intensity) indicating a range of values from 3 to 116 MPa (with an average value of nearly 60 MPa) on the wire cross section, and ranging from 70 to 116 MPa along the length of the coils. Similarly, as evident from Figure 39, the distributions of *all* six individual stress components were all significant in magnitude and distribution, thus showing the true *three-dimensional* nature of the state of stress, despite the application of simple axial load. Given the complexity of stress state, these results from simulation could not be “exactly” validated directly by experiment.

The numerical simulation and experimental counterpart for the transient deformation response of Case (1) are shown in Figure 40. This includes screen captures from the animation of the numerical simulation and from a video of the experiment showing all the four distinct deformation states (labeled 1 to 4). The helical-coil was initially loaded axially to 8.8 N at 30 °C and that constituted the first loading stage from the initial undeformed state 1 to the mechanically deformed state 2 at the end of isothermal loading phase of the experiment. Keeping the applied axial load constant (thus, isoforce condition), the spring was heated to 165 °C (i.e., from state 2 to state 3) and then cooled to 30°C (i.e., from state “3” to state 4), thus completing the first thermal cycle. These deformation states (1, 2, 3 and 4) are marked in the experimental axial displacement versus temperature response for this first thermal cycle in the inset of Figure 15.

Moreover, although the initial undeformed helical-coil has an initial helix angle of 4.7° (state 1), after the first thermal cycle (state 4), the helix angle increased to 90° in the numerical simulation and 93° in the experiment. The numerical model exhibited very similar deformation states with respect to the experimental counterpart, showing identical patterns of the significant bending and twisting of SMA wires (see state 4 in Figure 40). At the end of initial isothermal loading, one can observe a small increase in the helix angle in both the numerical simulation and the experiment (comparing the screen captures at state 2 with respect to 1 in Figure 40).

Figure 41 shows axial displacement (mm) verses temperature (°C) response for the transient deformation of Case (1) and Case (2). With regard to the evolution of the axial displacement in 10 thermal cycles, the FEA result exhibited relatively similar patterns of evolution of the axial displacement with respect to the experiment results during the 10 thermal cycles, (see Figure 42 for Case (1) and Figure 43 for Case (2)). Elaborate discussion of the procedures involved in this experimental validation has been given in Part iii of Section 3.2 as well in the Ph.D dissertation of Dr. Dhakal (Dhakal, 2013). Several of these results were also presented at the 2014 SMASIS conference.

In conclusion, the experimental validation of the numerical simulation results for the 55NiTi helical-coil actuator, using the calibrated SMA model, was successful. Against the background gained from the results obtained in this investigation, the following conclusions can be made.

a. The experimental results for the helical-coil actuator under two different boundary conditions were found to be very close (both qualitatively and quantitatively) to their counterparts in the numerical simulation which were performed prior to the experiments.
b. Both the simulation and experimental results demonstrated similar transient deformation response characteristics under complex stress/deformation states developed in the actuator, and these were identical in character to the simple strain versus temperature response obtained for a material-point under simple, uniaxial, isobaric tensile test condition.
c. In both the numerical simulation and the experiment, the boundary condition where the axially loading end is free to twist showed a higher axial displacement magnitude at the end of the cooling branch of the thermal cycle compared to the case where loading end was restrained to twist. There was no significant difference change in displacement during isothermal loading and the first heating branch.

2.6 References

Saleeb, A. F., Padula, S. A., and Kumar, A. (2011). A multi-axial, multimechanism based constitutive model for the comprehensive representation of the evolutionary response of SMAs under general thermomechanical loading conditions. *International journal of Plasticity*, *27*(5), 655-687

Manchiraju et al., 2011, “Thermal cycling and isothermal deformation response of polycrystalline NiTi: Simulations vs. experiment”. Acta Materialia 59, 5238-5249

R.D. Cook and W.C. Young, 1985, Advanced Mechanics of Materials, Macmillan Publishing Company, New York, USA

A. F. Saleeb, B. Dhakal, S. Dilibal, J. S. Owusu-Danquah, and S. A. Padula, On the modeling of the thermo-mechanical responses of four different classes of NiTi-based shape memory materials using a general multi-mechanism framework. 2015, *Mech. Mater.*, **80**, p 67-86.

Christ, D., and S. Reese. “A finite element model for shape memory alloys considering thermomechanical couplings at large strains.” *International Journal of solids and Structures* 46.20 (2009): 3694-3709.

Krone, L., J. Mentz, M. Bram, H.-P. Buchkremer, D. Stver, M. Wagner, G. Eggeler, D. Christ, S. Reese, D. Bogdanski, M. Kller, S. Esenwein, G. Muhr, O. Prymak, M. Epple. “The Potential of Powder Metallurgy for the Fabrication of Biomaterials on the Basis of Nickel-Titanium: A Case Study with a Staple Showing Shape Memory Behaviour.” *Advanced Engineering Materials* 7.7 (2005): 613-619.

Liu, X., Y. Wang, D. Yang, and M. Qi. “The effect of ageing treatment on shape-setting and superelasticity of a nitinol stent.” *Materials Characterization*, 59(2008):402-406.

Saleeb, A.F., B. Dhakal, M.S. Hosseini, and S.A. Padula II. “Large Scale Simulation of NiTi Helical Spring Actuators under Repeated Thermo-mechanical Cycles.” *Smart Materials and Structures,* 22.9(2013):094006.

Ancker, C.J. and J.N. Goodier. “Pitch and Curvature Corrections for Helical Springs.” *Journal of Applied Mechanics*, (1958):466-487.

Benafan, O., A. Garg, R.D. Noebe, G.S. Bigelow, S.A. Padula II, D. J. Gaydosh, and R. Vaidyanathan, (2014). Mechanical and functional behavior of a Ni-rich $Ni_{50.3}Ti_{29.7}Hf_{20}$ high temperature shape memory alloy. Intermetallics, 50, 94-107

Bigelow, G.S.,A. Garg, S. A. Padula II, D.J. Gaydosh and R.D. Noebe, R.D, 2011. “Load-biased shape-memory and superelastic properties of a precipitation strengthened high-temperature $Ni_{50.3}Ti_{29.7}Hf_{20}$ alloy.” *Scripta Materialia,* 64, 725-728.

Helm, D. (2001). Shape memory alloys: Experimental investigation, phenomenological modelling and numerical simulation of the thermomechanical material behaviour (Doctoral dissertation, Ph. D. thesis, Institute of Mechanics, Department of Mechanical Engineering, University of Kassel).

Tan, R. P., Kini, A., Shalouh, E., Marmur, J. D., and Sharma, S. K. (2001). Optimal treatment of nonaorto ostial coronary lesions in large vessels: Acute and long-term results. Catheterization and cardiovascular interventions, 54(3), 283-288.

Xia, Z., Ju, F., and Sasaki, K. (2007). A general finite element analysis method for balloon expandable stents based on repeated unit cell (RUC) model. *Finite Elements in Analysis and Design*, *43*(8), 649-658.

Sigwart, U. (1997). Stents: a mechanical solution for a biological problem? European Heart Journal 18 (7), 1068-1072.

3.0 Experimental and Neutron Diffraction Studies by UCF-Team

3.1 Summary of Neutron Diffraction Experiments

This section provides a summary of key experiments and analyses that were performed and are organized by the respective SMA system used (i.e., shape memory or superelastic). Such investigations included the use of the Spectrometer for MAterials Research at Temperature and Stress (SMARTS) at Los Alamos National Laboratory and the VULCAN engineering diffractometer at Oak Ridge National Laboratory (ORNL). Also, a portable axial/torsion load frame developed by the University of Tennessee, Knoxville (UTK) was utilized at the Neutron Residual Stress Mapping Facility (NRSF2) at ORNL. While the results are summarized here, more detailed descriptions of each experiment can be found in papers and previous quarterly reports, with the exception of experiments performed in the current quarter (Year 4, Quarter 4). Experiments performed at VULCAN in Year 4 Quarter 4 are provided at the end of this section.

3.1.1 Shape Memory NiTi

The material used during the first two experiments listed below was a binary NiTi alloy (nominal composition 49.9 at.% Ni), produced by Special Metals (now SAES Smart Materials, New Hartford, NY). Ten-millimeter rods were produced in the hot-rolled/hot-drawn and hot-straightened condition. Cylindrical dog-bone samples were machined to 5.08 mm in diameter and a 15.24 mm gauge length with threaded ends. Two stress-free thermal cycles (i.e., isobaric loading at 0 MPa) between room temperature (RT) and 200 °C were performed prior to every experiment after the specimen was installed in the load frame. This was done to relieve any residual stresses produced by processing, machining or installation of the sample and to establish initially, a self-accommodated B19′.

i. **Reverse loading of shape memory NiTi**.—All experiments were performed at room temperature at SMARTS. Compression-tension and tension-compression cyclic deformation was performed in strain control to ±2 and ±4% for 10 cycles at room temperature. Neutron diffraction spectra were acquired at 2% strain increments for the 1st, 2nd and final cycles. To insure adequate statistics for analysis a hold time of 30 min was used to acquire each spectrum. During all experiments a strain rate of 10^{-4} s^{-1} was maintained.

ii. **Isostrain, isostrain and isobaric loading of shape memory NiTi**.—Two experiments performed at SMARTS include: one compression-tension (i.e., compression followed by tension) isothermal loading cycle to ±4% strain, then back to 0% strain at RT; and one isostrain loading cycle at 2% tensile strain between 40 and 165 °C. Isobaric and isothermal loading was performed at VULCAN in one experiment in the following order: one isobaric loading cycle at 100 MPa tension between RT and 165 °C; compressive isothermal loading to –1.0% strain; two isobaric loading cycles at 0 MPa between RT and 165 °C; and isothermal loading to 3.9% tension at RT. Neutron diffraction spectra were acquired at select points throughout all experiments as shown in context of the results.

3.1.2 Superelastic NiTi

The material used for next three experiments was a commercially available, biomedical grade binary NiTi (nominal composition 50.8 at.% Ni), produced by Fort Wayne Metals (Fort Wayne, IN). Solid cylindrical dog-bone samples were machined to three sizes with threaded ends as follows (gauge diameter x gauge length): 5.08- by 17.8-mm; 5.08- by 50.8-mm; and 7.00- by 50.8-mm designated as *S1* and *S2*; *S3;* and *S4*, respectively. Following machining, the samples were heat treated at 350°C for 1 hour, in air, then ice-quenched. Sample *S1* and *S2* was designed for an axial torsion gripping system available at the VULCAN engineering diffractometer and samples *S3* and *S4* were designed for a portable axial-torsion load frame employed at NRFS2, see References 1 and 2, respectively, for further details.

iii. **Torsional and uniaxial loading and heating of superelastic NiTi at VULCAN**.—The following experiments were performed at VULCAN. One sample with geometry *S1* was subjected to two cycles of pure torsional (0 MPa axial stress) between 0 and 60° in angle control mode and then heated from room temperature to above the austenite finish (A_f) under no-load.

iv. **Torsional loading of superelastic NiTi at NRSF2**.—Two samples of geometries *S3* and *S4* were subject to pure torsional loaded up to 550 MPa with different diffraction orientations and geometries (in order to investigate the principle stress and hoop and radial directions, respectively) using the NRSF2. Neutron diffraction spectra were acquired at shear stress values chosen to target regions of transformation and will presented in context of the results. At these specific shear stress values diffraction spectra were acquired for diffraction volumes defined in Figure 44a and Figure 45a for samples *S3* and *S4*, respectively.

3.1.3 VULCAN experiments performed in March 2015

The material used during the first set experiments listed below uses the same binary NiTi alloy, sample geometry, setup and heat treatment as described above under *shape memory NiTi.* All experiments below were performed at room temperature.

v. **Bi-axial loading of shape memory NiTi**.—One sample was isothermal loaded to 2% strain (in strain control). Then displacement was held constant (in displacement control while the sample was loaded and unloaded in torque control to 10 N·m (in torque control). Finally the sample was loaded back to the initial angle of twist (in angle control). This experiment was repeated two more samples at 4% tensile strain and 2% compressive strain. Neutron data was acquired by continuous scanning during all experiments.

The material used during the first set experiments listed below uses the same superelastic NiTi alloy, sample geometry, setup and heat treatment as described above under *superelastic NiTi,* experiment iii. All experiments below were performed at room temperature.

vi. **Reverse loading of R-phase in superelastic NiTi**.—Sample *S2* as described above was previously subjected to six cycles of pure tension loading (0 MPa shear stress) between 0 and 500 MPa. The same sample was subjected to compression-tension cyclic loaded between ±0.5% strain. Neutron data was acquired by continuous scanning during all experiments.

3.2 Review of Results

Results from the aforementioned experiments done during the latter part of this NASA award and SMA spring experiments will be summarized in context of the following three bodies of work as part of Douglas Nicholson's Ph.D dissertation at UCF. He has accepted a position with the Boeing Company and will finish his Ph.D part time.

1. D.E. Nicholson, O. Benafan, S.A. Padula II, R.D. Noebe and R. Vaidyanathan. "Isothermal, Isostrain and Isobaric Loading of Polycrystalline Shape Memory NiTi," *Appl. Phys. Lett.*, in preparation

2. D.E. Nicholson, S.A. Padula II, O. Benafan, J.R. Bunn, E.A. Payzant, D. Penumadu and R. Vaidyanathan, “Mapping of Texture and Phase Fractions in Non-uniform Stress States during Multi-axial Loading of Superelastic NiTi” *Adv. Mater.* in preparation
3. B. Dhakal, D.E. Nicholson, A.F. Saleeb, S.A. Padula II and R. Vaidyanathan. “Three-dimensional Deformation Response of Shape-memory NiTi Helical-coil Actuators during Thermo-mechanical Cycling: Experimental Validation of Model Prediction,” *J. Mech. Phys. Solids* in preparation

i. Isothermal, isostrain and isobaric loading of polycrystalline shape memory NiTi

The overall objective of this work is to provide micromechanical and microstructural insight into the isothermal (deformation at constant temperature), isobaric (thermal cycling to temperatures above and below the phase transformation temperatures under constant stress), and isostrain (thermal cycling to temperatures above and below the phase transformation temperatures under constant strain) loading of shape memory alloys (SMAs) with emphasis on providing connections between these loading paths.

Figure 46 shows inverse pole figures (IPFs) for the loading direction and corresponding macroscopic response of B19′ martensitic NiTi under isothermal compressive followed by tensile, then compressive reverse loading (as shown by the solid black line). Also shown are the macroscopic positions of Points III-VI of Figure 47 (as indicated by ▲). Isothermal compressive loading immediately followed by tensile loading showed that martensite variants preferentially selected in compression reorient to a near random self-accommodated orientation when the load is reversed and the macroscopic strain approaches zero. Similarly, loading in tension resulted in preferred variants that again reoriented to a near random self-accommodated orientation once the load is reversed to obtain zero strain. In all cases of such isothermal reverse loading (i.e., compression followed by tension or tension followed by compression), the resulting martensite variant structure correlated with the macroscopic uniaxial strain and did not correlate with the compressive or tensile state of stress.

The correlation between the resulting variant structure and the macroscopic strain was also noted when a sample was isothermally strained and then thermally cycled to temperatures above and below the phase transformation while keeping strain constant (isostrain loading). Figure 48 shows IPFs for the loading direction and corresponding macroscopic response of B19′ martensitic NiTi at before (Point II) and after (Point IV) one thermal cycle to temperatures above and below the phase transformation under a constant strain of 2%. In this experiment, the macroscopic stress from the isothermal strain relaxed to near zero with no concomitant change in the variant structure following the first thermal cycle.

Lastly, the experiments examined the variant structure obtained through isothermal deformation followed by heating and cooling under stress following deformation (isobaric loading). Figure 47 shows inverse pole figures (IPFs) for the loading direction corresponding to mixed isothermal (indicated by solid arrows) and isobaric (indicated by dashed arrows) loading in the same experiment. During isobaric loading the sample was thermally cycled to temperatures above and below the room temperature, once from Points II to III and twice from Points VII to VIII. The corresponding macroscopic position is given above each IPF. The load-bias cycle resulted in the 3.7% transformation strain and preferred selection of tension variants occurred (as correlated to an increase in m.r.d. near the B19′ 010 pole). The sample was then loaded isothermally in compression to –1.0% strain at RT during which martensite variants reoriented to near random distribution with a small amount of tension variants. The sample was unloaded and two no-load thermal cycles were performed (UCT=165°C) resulting in a near zero stress and strain. Finally, the sample was strained monotonically to 3.7% strain. Following the two no-load the thermal cycles martensite variant orientation moved closer to random. When the sample was strained to 3.7% tension variants were once again selected. Thus, the variant structures were equivalent for the corresponding strain and more importantly, the reversibility and equivalency was immediately evident in a variant structure that was first formed isobarically but then reoriented to a near random self-accommodated structure by isothermal deformation. These results are consistent as well with variant reorientation and detwinning correlating well with uniaxial strain and not correlating well with uniaxial stress.

ii. Mapping of texture and phase fractions in nonuniform stress states during multi-axial loading of superelastic NiTi

Four biomedical grade superelastic NiTi (nominal composition 50.8 at.% Ni) cylindrical samples were investigated using *in situ* neutron diffraction. Two samples (denoted *S1* and *S2*) were heated from room temperature to above the austenite finish (A_f) and compression-tension cyclic loaded between ±0.5% strain, respectively, at the “time-of-flight” VULCAN diffractometer at the SNS at ORNL. Two samples (denoted *S3* and *S4*) were subject to pure torsional loading (up to 550 MPa) with different diffraction orientations and geometries (in order to investigate the principle stress and hoop and radial directions, respectively) using the NRSF2 at the steady-state High Flux Isotope Reactor (HFIR) at ORNL. More details regarding sample preparation, experimental setups and procedures can be found in the experimental section.

Figure 49(a) shows a section of normalized neutron diffraction spectra acquired during isobaric cooling from austenite to R-phase of sample *S1* under no stress. The austenite to R-phase transformation occurs by way of elongating the B2 cube along one of its (111) axis, i.e., the triad axis (Ref. 3). Thus, a total of four variants can be formed during this transformation. One variant (henceforth called variant A) corresponds to the elongated triad of the cube. The other three variants (henceforth called variant B, C or D) correspond to the three contracted triads. This was demonstrated experimentally by the splitting of the $(111)_A$ austenite peak into $(11\text{-}1)_R$ and $(111)_R$ R-phase peaks during cooling from above the austenite finish (A_f) to room temperature, as shown in Figure 49(a). At room temperature the system was shown by Rietveld refinement to be primarily R-phase with up to ~20% austenite. Rietveld Refinements were performed with phase volume fractions constrained to be equal between both spectra acquired from lattice planes perpendicular (with diffraction vector $Q_{\parallel}$ parallel to the loading axis) and parallel (with diffraction vector $Q_{\perp}$ perpendicular to the loading axis) to the length of the sample. The ratio of intensities of the $(11\text{-}1)_R$ and $(111)_R$ peaks, Y_{111}/Y_{11-1}, was found to be 27.96 and 19.27% corresponding to $Q_{\parallel}$ and $Q_{\perp}$, respectively, which was comparable to that of sample *S2* (found to be 28.96 and 20.05% corresponding to $Q_{\parallel}$ and $Q_{\perp}$, respectively) following heat treatment prior to loading. In both cases this R-phase variant orientation was formed by cooling from austenite under no-load and was thus considered to be self-accommodated. Note the self-accommodated R-phase variant orientation in this system was not random and had fiber texture along the length of the samples. The intrinsic texture in this system was formed during processing and has been observed in comparable NiTi systems following similar processing (Ref. 4).

The experimentally measured strains ($\varepsilon_1 = 0.86\%$ and $\varepsilon_2 = -0.4\%$, as shown in Figure 49(a)) correlated well with the single crystal Bain strains calculated from crystallographic theory for this alloy (i.e., the Bain strain associated with R-phase variant A and B, C, or D w.r.t. the $\langle 111\rangle_{B2}$ direction was found to be $\varepsilon_{111}^{A} = 0.96\%$ and $\varepsilon_{111}^{B} = -0.32\%$, respectively) and allowed for the identification of these specific R-phase variants. By comparing crystallographic theory to experiment it becomes apparent that the $(111)_R$ and $(11\text{-}1)_R$ peaks correspond to R-phase variant A and B, C or D, respectively. In the following discussion, variants A and B, C or D refer to R-phase variants w.r.t. the $\langle 111\rangle_{B2}$ direction and by employing symmetry variants B, C or D will be referred to as variant B unless otherwise stated (e.g., in the Year 3 annual report). Details of the Bain strain calculations for the $(111)_A$ to R-phase transformation (as shown in Figure 49(a)) as well as for the $(110)_A$ to R-phase transformation (not shown here) can be found in the Year 3 annual report.

Figure 49(b) shows a section of normalized neutron diffraction spectra acquired during isothermal uniaxial tension-compression (between ±0.5% macroscopic strain) reverse cyclic loading of R-phase at room temperature in sample *S2*. At zero strain, the ratio of intensities of variant A and variant B, $Y_\mathrm{A}/Y_\mathrm{B}$, was found to be 56.99 and 14.64% corresponding to $\mathrm{Q}_{\|}$ and $\mathrm{Q}_{\perp}$, respectively. Therefore, at zero strain as shown Figure 49(b) in sample *S2* the R-phase variant structure was not self-accomodated, as previously defined. During loading in compression (from zero to –0.5%) macroscopic strain the intensity of variant A decreases at the expense of variant B indicating reorientation and/or detwinning of R-phase variants. Note, increases in R-phase peak intensities may also be attributed to the formation R-phase from austenite under stress. However, the amount of austenite at room temperature was limited to at most 20% volume fraction, therefore the major contribution of peak intesnity changes in R-phase was attributed to reorientation and/or detwinning of R-phase variants. At ~–0.175% strain the ratio $Y_\mathrm{A}/Y_\mathrm{B}$, was found to be 32.49 and 22.5% corresponding to $\mathrm{Q}_{\|}$ and $\mathrm{Q}_{\perp}$, respectively, therefore indicating a near self-accommdated R-phase variant structure. The intensities at -0.175% strain will be arbitrarily chosen as the references (i.e., $Y^\mathrm{A}_{-0.175}/Y^\mathrm{A}_o = 1$ and $Y^\mathrm{B}_{-0.175}/Y^\mathrm{B}_o = 1$ at -0.175% strain) for the normalization of intensities given in the proceeding discussion. Therefore, intensites of R-phase variants at macroscopic strain ε are normalized w.r.t. self-accommodation as opposed to zero macroscopic strain.

When deformation was continued to –0.5% strain the normalized intensity of variant B ($Y^\mathrm{B}_{-0.5}/Y^\mathrm{B}_o$) had increased to 1.286, while the normalized intensity of variant A ($Y^\mathrm{A}_{-0.5}/Y^\mathrm{A}_o$) had decreased to 0.452. This provided direct evidence of preferred selection of R-phase variant B under compressive tensile loading. These variants preferentially selected in compression reoriented to a near random self-accommodated orientation (as indicated by $Y^\mathrm{A}_{-0.175}/Y^\mathrm{A}_o = 1.012$ and $Y^\mathrm{B}_{-0.175}/Y^\mathrm{B}_o = 1.011$) when the deformation was reversed (from –0.5 to –0.175% strain) and the macroscopic strain approached –0.175%, thus indicating the reversibility of variant reorientation and detwinning processes. When deformation was continued in tension to 0.5% strain preferred selection of R-phase variants was observed as an increase and decrease in variants A and B to 2.261 and 0.296, respectively. This provides direct evidence that variant A was the preferred R-phase variant under uniaxial tensile loading. These variants preferentially selected in tension reoriented to a near random self-accommodated orientation when the deformation was reversed again and the macroscopic strain approached –0.175%, further demonstrating the reversibility of variant reorientation and detwinning processes. Analogous preferred variant selection (Ref. 5) and the isothermal reversibility of variant selection (as demonstrated in the previous section) by variant reorientation and/or detwinning of B19′ variants has been observed in martensitic NiTi.

The aforementioned R-phase variants followed during uniaxial loading and heating at VULCAN were investigated in the principle stress directions during pure torsional loading at NRSF2. Figure 44(a) shows an idealized cross-section of cylindrical specimen *S3* and the cross-section of the two diffraction gauge volumes with the load frame tilted to 43° (about the x-axis). Note the load frame was titled to 43° during this experiment and was assumed to be tilted to the ideal 45° when referring to the planes of maximum and minimum normal stress in the following discussion. This configuration produced reflections representative of the principle stress directions under negative (location 1, with plane normals along the direction of minimum normal stress, or diffraction vector $\mathrm{Q}_{-\theta z}$,) and positive (location 2, with plane normals along the direction of maximum normal stress or diffraction vector $\mathrm{Q}_{+\theta z}$) shear stress. To facilitate the following discussion, the directions of maximum tensile and compressive stress will henceforth be referred to as the “tensile direction” and “compressive direction,” respectively. Shear stress values shown in Figure 44(b) and (c) represent the maximum applied shear stress at the surface. Figure 44(b) shows sections of normalized spectra from lattice planes perpendicular to the compressive direction (location 1) under pure torsional loading up to 500 MPa. The intensity of variant B increased with shear stress and there was no detectable formation of variant A. Figure 44(c) shows sections of normalized spectra from lattice planes perpendicular to the tensile direction (location 2) under pure torsional loading up to 550 MPa. The intensity of variant A increased with shear stress as variant B decreased. Therefore, variant reorientation and detwinning occurred under torsional loading with preferred selection of variant A and variants B in the tensile and compressive directions, respectively.

Overall, tension-compression asymmetry observed in the preferred selection of specific R-phase variants was consistent between uniaxial and torsional loading when the principle directions of the stress state were considered (for the crystallographic directions investigated here). At the maximum shear stress under torsional (as indicated by the red lines, in Figure 44(b) and (c)) the R-phase peaks had decreased, but were still observable as, globally, the system had only partially transformed to B19′ martensite. This result is not surprising as the diffraction volumes used (at location 1 and 2 in Figure 44(a)) covered a large portion of the samples radius and thus represented reflections averaged over a heterogeneous stress state.

Figure 50(a) shows a section of normalized spectra from lattice planes perpendicular to the tensile direction (at location in Figure 44(a)). Upon loading from –110 to 100 MPa the $(200)_R$ peak shifted to the right (indicating lattice strain) with negligible change intensity (indicating minimal detwinning and variant reorientation). This result is consistent with crystallographic theory which is explained as follows. The $(200)_R$ peak forms by an invariant transformation from $(200)_A$ peak along the $\langle 100 \rangle_{B2}$ direction and variant conversion is not possible in this crystallographic direction (as described in detail in Year 3 annual report). At a maximum shear stress of 550 MPa the $(030)_M$ martensite peak was observed (as depicted by the red line). The $(030)_M$ martensite was undetectable in the compressive direction (at location 1 in Figure 44(a)) at a maximum shear stress of 550 MPa. The formation of a $(030)_M$ peak w.r.t. the tensile direction and not in the compressive direction under torsional loading is indicative of preferred selection of B19′ variants variant in martensitic NiTi. Furthermore, $(030)_M$ martensite has previously been observed as a preferred variant formed under uniaxial tensile loading (Ref. 5). This result suggests that martensite variant selection, like R-phase variant selection, is consistent between uniaxial and torsional loading when the principle directions of the stress state were considered. However, this result cannot be deemed conclusive as only one of 12 correspondent variant pairs of B19′ martensite was considered here.

Figure 50(b) shows strains (indicated by ■) and Full Width at Half Maximum (FWHM, indicated by ●) determined from changes in d-spacing and peak breadth, respectively, of the $(200)_R$ peaks shown in Figure 50(a). Results shown in Figure 50(b) summarize and facilitate the above discussion regarding the $(200)_R$ peaks shown in Figure 50(a). An increasing linear relationship between shear stress and lattice strain for $(200)_R$ peak was observed which indicates tensile strain. The relationship remains linear above 100 MPa when the $(200)_R$ peak begins to decrease as shown in Figure 50(a). Thus, the $(200)_R$ decreased due to the phase transformation from R-phase to martensite with no contributions from variant and reorientation of R-phase variants. An increasing linear relationship between the FWHM and shear stress was observed and attributed to peak broadening caused by the averaging of strain over a heterogeneous stress state.

In order to further investigate the heterogeneity of the stress state under torsional loading variant B was tracked and spatially resolved in the radial and hoop directions during pure torsional loading at NRSF2. Figure 45(a) shows the cross-section of cylindrical specimen *S4* and the cross-section of six diffraction gauge volumes within the cylinder. The load frame was positioned vertical to produce reflections from lattice planes perpendicular to the radial (location 1-5, Q_{radial}) and hoop (location 6, Q_{hoop}) directions of the specimen. Note, strains in these directions are negligible under pure torsional loading, however phase fraction and texture evolution can still be observed as changes in peak intensity. Figure 45(b) shows the normalized intensity (arbitrary units) of variant B as a function of the radial (mm) distance from the center of the sample to the center of the spatially resolved diffraction volumes shown in Figure 45(a). All stress values shown represent the applied shear stress at the surface the specimen.

The uncorrected integrated intensity denoted as Y_i^{I} is shown in Figure 45(b) (as indicated by the black dashed line) I_i^{I} and depicts the absorption profile in the initial condition. The data was corrected for absorption, normalized to point (1,I) and is defined as follows:

$$NI_i^j = \frac{Y_1^{\mathrm{I}}}{Y_i^{\mathrm{I}}} \cdot \frac{Y_i^j}{Y_1^j} \tag{1}$$

where subscript *i* increments through spatial locations 1-6, superscript *j* increments through shear stress values I-VIII, I is uncorrected integrated intensity and *NI* is the normalized intensity shown in Figure 45(b). The increase in intensity from points I to III corresponds to the preferred selection of variant B in the radial direction by R-phase detwinning and variant reorientation. Furthermore, the intensity increases with radius (points 1-5) corresponding to increasing stress with radius. From Points III-VI intensity decreases with stress due to transformation of detwinned/reoriented R-phase to B19′. At a maximum shear stress of 500 MPa (shown as Point VI) the intensity varies from 1 to 0 from the center of the cylinder to near the surface of cylinder corresponding to a near zero stress at the center to maximum stress near the surface. This is consistent with classical torsional loading, however the distribution of stress cannot be assumed to be linear with radius.

Locations 5 and 6 are the same radial distance from the center of the sample. Location 5 corresponds to reflections from lattice planes perpendicular to the radial direction, while location 6 corresponds to reflections from lattice planes perpendicular to the hoop direction. During loading from 0 to 150 MPa (shown as points I-III) intensity at locations 5 and 6 evolves differently with increasing shear stress. Following the onset of the phase transformation from R to B19′ (points IV-VI); intensity at locations 5 and 6 evolves similarly with increasing shear stress. This result suggests that preferred variant selection of R-phase variants is different between the radial and hoop direction during torsional loading. This result is not expected during uniaxial loading in which lattice planes in both the radial and hoop are parallel to the loading direction (i.e., plane normal are in the $Q_{\perp}$direction) and are under a homogenous compressive stress state as governed by the Poisson effect.

Aforementioned deformation mechanisms (e.g., elastic deformation, variant reorientation and detwinning in R-phase and phase transformation from R-phase to martensite) investigated by recourse to *in situ* neutron diffraction are typically observed as changes in moduli in the macroscopic response. To facilitate the connection between aforementioned results and macroscopic behavior, Figure 45(c) shows the macroscopic stress-strain response under pure torsional loading (up to 500 MPa) of sample *S4* at room temperature. Note extensometry could not be used due the large deformations seen here. Therefore, the shear strain shown in Figure 45(c) was calculated at the surface from the angle of twist measured at the grips and the effective gauge length of the cylindrical specimen. The shear stress values for which neutron data was presented in Figure 45(b) and labeled I-VIII are shown in Figure 45(c). Deformation caused by loading from 0 to 200 MPa (points I to IV) is attributed to elastic deformation and detwinning and variant reorientation of R-phase. Point IV represents the onset of the phase transformation from R-phase to martensite. Deformation caused by loading from 200 to 500 MPa (points IV to VI) is attributed to the phase transformation from R-phase to martensite with additional but limited contributions from variant reorientation and detwinning and elastic deformation of martensite. Deformation caused by unloading from 500 to 0 MPa (points V to VIII) is attributed to the reverse phase transformation from martensite to R-phase with additional but limited contributions from variant reorientation and detwinning and elastic recovery of martensite and R-phase.

iii. 55NiTi spring experiments

a) Spring fabrication

Wire was Electro Discharge Machined (EDM) (to a wire diameter of 2.16 mm) from the same 55NiTi extrusion used to calibrate the SMA model. The 55 NiTi wire was wound onto a mandrel with a helical grove (with the geometric parameters of the modeled spring) at room temperature. A sleeve was slid over the wire and mandrel to ensure that the wire maintained its desired spring shape throughout the shape-setting process. The spring was shape-set at 450 °C for 30 min. and then ice-quenched. It has previously been shown that the shape-setting process does not have a significant effect on subsequent thermomechanical behavior in this particular material system. The as-shape-set spring consisted of three active coils (four in total), with a coil diameter of 23.1 mm and a free length of 19 mm. This process was repeated to produce a total of two identical springs, one for each of the two aforementioned cases.

b) Experimental setup

A modular test setup (Figure 51) for the purpose of testing SMA springs (with various end constraints) was designed and assembled. A detailed description of the experimental setup can be found in Reference 6. The following two configurations were used to experimentally validate case (1) and case (2). For case (1), one spring mount was coupled to the torque cell (with a range of 0 to 176.5 N·mm), to measure the torque produced during actuation when the spring was constrained from rotating. For case (2), one spring mount was coupled to a rotary encoder, to measure the degree of twist produced during actuation when the spring was free to rotate. For both cases care was taken to ensure the boundary conditions mirrored (as close as possible) the boundary conditions applied in the simulation (i.e., rigid with no conductive heat loss at the point of contact with each spring mount).

c) Thermomechanical cycling

Using the setup described in Section 3.2, paragraph iii.a), the following tests were performed. Two stress-free thermal cycles (between room temperature and 165 °C) were performed (to relieve any residual stresses produced by processing, machining or installation of the spring) prior to the experiment after the spring was installed in the setup. Following the two no-load thermal cycles an axial tensile load of 8.8 N was applied to the spring at room temperature. Under this constant load, up to 20 thermal cycles were performed between an LCT=35 °C and UCT=165 °C. This thermomechanical loading procedure was performed for case (1) and Case (2) using an as shape set spring for each case.

Figure 52 shows a summary of the experimental results for thermal cycling of a 55NiTi spring actuator (Spring 1) under 8.8 N for both cases (1) and (2). The results have been previously reported on and are summarized here. Results for both cases show that the displacement increased (without bound, however the rate of increase of displacement decreased) during each thermomechanical cycle (for up to the 20 thermomechanical cycles tested). The stroke for each case was the same (within error) and increased, for the first 3 to 5 cycles. For case (1) the stroke stabilized after approximately 5 cycles. For case (2) the stroke began decreasing after approximately 5 cycles. Hence, over the entire 20 cycles the rotationally unconstrained case produced a larger stroke. For both cases, the angle of twist and reaction moment (so called secondary responses), respectively, also increased with each thermomechanical cycle.

Increases in the secondary responses were larger (near an order of magnitude) in the austenite than in the martensite. This indicates the secondary responses were minimized in the martensite due to martensite variant reorientation and detwinning, which allowed for favorable selection of martensite variants.

3.3 References

1. O. Benafan, S.A. Padula II, H.D. Skorpenske, K.A. and R. Vaidyanathan, “Design and implementation of a multiaxial loading capability during heating on an engineering neutron diffractometer,” Rev. Sci. Instrum. 85 (2014) 103901.
2. R. Woracek, J.R. Bunn, D. Penumadu and C. Hubbard, “Method to determine hkl strains and shear moduli under torsion using neutron diffraction,” Appl. Phys. Lett. 100 (2012) 191904-5.
3. S. Miyazaki and C. Wayman, “The R-phase transition and associated shape memory mechanism in Ti-Ni single crystals,” Acta metall. 36 (1988) 181-192.
4. S. Cai, J. Schaffer, Y. Ren and C. Yu, “Texture evolution during nitinol martensite detwinning and phase transformation,” Appl. Phys. Lett. 103 (2013) 241909.
5. S. Qiu, B. Clausen, S.A. Padula II, R.D. Noebe and R. Vaidyanathan, “On elastic moduli and elastic anisotropy in polycrystalline martensitic NiTi,” Acta Mater. 59 (2011) 5055-5066.
6. D.E. Nicholson, O. Benafan, S.A. Padula II, R.D. Noebe and R. Vaidyanathan. “Thermomechanical behavior of NiTiPdPt high temperature shape memory alloy springs,” Smart Mater. Struct. 23 (2014) 125009.

4.0 Journal Papers and Other Publications to Disseminate Project Results

A number of journal papers and conference proceeding articles were produced based on results from several parts of the work accomplished during the four year period of the project:

4.1 Modeling Activities (UA-Team)

4. Saleeb, A. F., Dhakal, B., Padula II, S. A., and Gaydosh, D. J. (2013a). Calibration of SMA material model for the prediction of the ‘evolutionary’load-bias behavior under conditions of extended thermal cycling. *Smart Materials and Structures*, *22*(9), 094017.
5. F. Saleeb, B. Dhakal and S. A. Padula II, 2012. “Theoretical Development, Characterization, and Application of a 3D Multi-mechanism SMA Material Model for the Analysis of SMA based Actuators,” ASME 2012 Conference on Smart Materials, Adaptive Structures and Intelligent System, September 19-21, 2012 in Stone Mountain, Georgia (Symposium 2 on Mechanics and Behavior of Active Materials).
6. S. A. Padula II, D.J. Gaydosh, A. F. Saleeb, and B. Dhakal, 2012. “Transients and Evolutions in 55NiTi,” ASME 2012 Conference on Smart Materials, Adaptive Structures and Intelligent System, September 19-21, 2012 in Stone Mountain, Georgia (Symposium 2 on Mechanics and Behavior of Active Materials).
7. Fixed Wing (FW) Fundamental Research Awards Year 1 Review and the Aeronautical Sciences (AS) NRA Review, July 2012, Ohio Aerospace Institute (OAI) Cleveland, OH.
8. Fixed Wing (FW) Fundamental Research Awards Year 2 Review and the Aeronautical Sciences (AS) NRA Review, Aug. 2013, Ohio Aerospace Institute (OAI) Cleveland, OH.
9. Fixed Wing (FW) Fundamental Research Awards Year 3 Review and the Aeronautical Sciences (AS) NRA Review, June 2014, Ohio Aerospace Institute (OAI) Cleveland, OH.
10. D.E. Nicholson, B. Dhakal, A.F. Saleeb, S.A. Padula II, R.D. Noebe and R. Vaidyanathan, “Thermomechanical Behavior of Shape Memory NiTi Springs for Model Validation,” ASME 2014 SMASIS, Newport, RI, September 8-10, 2014.
11. Saleeb, A. F., Padula, S. A., and Kumar, A. (2011). A multi-axial, multimechanism based constitutive model for the comprehensive representation of the evolutionary response of SMAs under general thermomechanical loading conditions. *International journal of Plasticity*, *27*(5), 655-687.
12. Saleeb, A. F., Kumar, A., Padula, S. A., and Dhakal, B. (2013b). The cyclic and evolutionary response to approach the attraction loops under stress controlled isothermal conditions for a multi-mechanism based multi-axial SMA model. *Mechanics of Materials*, *63*, 21-47.
13. Padula II, S. A., Gaydosh, D., Saleeb, A., and Dhakal, B. (2014). Transients and Evolution in NiTi. *Experimental Mechanics*, *54*(5), 709-715.
14. F. Saleeb, B. Dhakal and S. A. Padula II, 2012. “Theoretical Development, Characterization, and Application of a 3D Multi-mechanism SMA Material Model for the Analysis of SMA based Actuators,” ASME 2012 Conference on Smart Materials, Adaptive Structures and Intelligent System, September 19-21, 2012 in Stone Mountain, Georgia (Symposium 2 on Mechanics and Behavior of Active Materials).
15. S. Dilibal, A. F. Saleeb, B. Dhakal, A.E. Hurley, J. S. Owusu-Danquah, S. A. Padula II, R. D. Noebe and G. S. Bigelow, 2013. “Characterization Capabilities of a 3D Multi-mechanism Material Model for the Prediction of the Thermo-mechanical Behavior of Different Classes of Shape Memory Materials,” ASME 2013 Conference on Smart Materials, Adaptive Structures and Intelligent Systems, September 16-18, 2013 in Snowbird, Utah, USA (Symposium 2 on Mechanics and Behavior of Active Materials).

16. B. Dhakal, D.E. Nicholson, A. F. Saleeb, S. A. Padula II and R. Vaidyanathan, 2013. “Prediction of the Evolving Multi-dimensional Deformation Response of a Shape Memory NiTi Spring under Thermo-mechanical Cycling,” ASME 2013 Conference on Smart Materials, Adaptive Structures and Intelligent Systems, September 16-18, 2013 in Snowbird, Utah, USA (Symposium 2 on Mechanics and Behavior of Active Materials)
17. J.S. Owusu-Danquah, A. F. Saleeb, B. Dhakal, A.E. Hurley , S. Dilibal, S. A. Padula II, R. D. Noebe, and G. S. Bigelow, 2013. “Large-scale Simulation of a Torque-Tube Actuator Using a 3D Multi-mechanism Material Model: A Comparative Study with $Ni_{49.9}Ti_{50.1}$ and $Ni_{50.3}Ti_{29.7}Hf_{20}$ Shape Memory Alloys,” ASME 2013 Conference on Smart Materials, Adaptive Structures and Intelligent Systems, September 16-18, 2013 in Snowbird, Utah, USA (Symposium 2 on Mechanics and Behavior of Active Materials).
18. S. A. Padula II, D.J. Gaydosh, A. F. Saleeb, and B. Dhakal, 2012. “Transients and Evolutions in 55NiTi,” ASME 2012 Conference on Smart Materials, Adaptive Structures and Intelligent System, September 19-21, 2012 in Stone Mountain, Georgia (Symposium 2 on Mechanics and Behavior of Active Materials).
19. Saleeb, A. F., Dhakal, B., Dilibal, S., Owusu-Danquah, J. S., and Padula, S. A. (2015a). On the modeling of the thermo-mechanical responses of four different classes of NiTi-based shape memory materials using a general multi-mechanism framework. *Mechanics of Materials*, *80*, 67-86.
20. Saleeb, A. F., Dhakal, B., Hosseini, M. S., and Padula II, S. A. (2013c). Large scale simulation of NiTi helical spring actuators under repeated thermomechanical cycles. *Smart Materials and Structures*, *22*(9), 094006.
21. Owusu-Danquah, J. S., Saleeb, A. F., Dhakal, B., and Padula II, S. A. (2015). A Comparative Study of $Ni_{49.9}Ti_{50.1}$ and $Ni_{50.3}Ti_{29.7}Hf_{20}$ Tube Actuators. *Journal of Materials Engineering and Performance*, *24*(4), 1726-1740.
22. Saleeb, A. F., Dhakal, B., and Owusu-Danquah, J. S. (2015b). Assessing the performance characteristics and clinical forces in simulated shape memory bone staple surgical procedure: The significance of SMA material model. *Computers in biology and medicine*, *62*, 185-195.
23. Saleeb, A. F., Dhakal, B., and Owusu-Danquah, J. S. (2015c). On the role of SMA modeling in simulating NiTinol self-expanding stenting surgeries to assess the performance characteristics of mechanical and thermal activation schemes. *Journal of the mechanical behavior of biomedical materials*, *49*, 43-60.
24. Dhakal, B., Characterization of a 3D multi-mechanism SMA material model for the prediction of the cyclic “evolutionary” response of NiTi for use in actuations, 2013, Doctoral dissertation, *Ph. D. thesis*, Department of Civil Engineering, University of Akron.

4.2 Experimental Activities (UCF-Team)

1. D.E. Nicholson, S.A. Padula II, O. Benafan, H.D. Skorpenske, K. An, E.A. Payzant and R. Vaidyanathan, “Investigation of the R-phase during Stress- and Temperature- Induced Phase Transformation in NiTi,” TMS 2015 Annual Meeting, Orlando, FL, March 15-19, 2015.
2. D.E. Nicholson, S.A. Padula II, O. Benafan, R. Woracek, S.B. Puplampu, J.R. Bunn, E.A. Payzant, D. Penumadu and R. Vaidyanathan, “Mapping of Texture and Phase Fractions in Non-uniform Stress States during Torsional Loading of Superelastic NiTi,” TMS 2015 Annual Meeting, Orlando, FL, March 15-19, 2015.
3. D.E. Nicholson, B. Dhakal, A.F. Saleeb, S.A. Padula II, R.D. Noebe and R. Vaidyanathan, “Thermomechanical Behavior of Shape Memory NiTi Springs for Model Validation,” ASME 2014 SMASIS, Newport, RI, September 8-10, 2014.

4. D.E. Nicholson, O. Benafan, S.A. Padula II, R.D. Noebe and R. Vaidyanathan, "Optimizing Loading and Heating Sequences to Obtain Optimal Textures in NiTi Shape Memory Alloy Actuators," ASME 2014 SMASIS, Newport, RI, September 8-10, 2014.
5. D.E. Nicholson, O. Benafan, S.A. Padula II, R.D. Noebe and R. Vaidyanathan, "Isobaric, Isothermal and Isostrain Loading of polycrystalline Shape Memory NiTi," ASME 2013 SMASIS, Snowbird, UT, September 16-18, 2013.
6. D.E. Nicholson, O. Benafan, S.A. Padula II, R.D. Noebe and R. Vaidyanathan, "Asymmetry and Control Mode Effects in Polycrystalline NiTi," TMS 2013 Annual Meeting, San Antonio, TX, March 3-7, 2013.
7. D.E. Nicholson, O. Benafan, S.A. Padula II, R.D. Noebe and R. Vaidyanathan, "Neutron Diffraction Investigation of Tension-Compression Cyclic Deformation in Polycrystalline NiTi," ASME 2012 SMASIS, Stone Mountain, GA, September 19-21, 2012.
8. D.E. Nicholson, O. Benafan, S.A. Padula II, R.D. Noebe and R. Vaidyanathan, "An In Situ Neutron Diffraction Study of Tension-Compression Cyclic Deformation in Polycrystalline NiTi," European Symposium on Martensitic Transformations, St. Petersburg, RU, September 9-16, 2012.
9. R. Vaidyanthan (invited): "In situ Neutron Diffraction Study of Shape Memory Alloys under Isothermal, Isobaric and Isostrain loads," TMS 2013 Annual Meeting, San Diego, CA, February 16-20, 2014.
10. R. Vaidyanthan (invited): "Microstructural and Geometrical Size Scale Effects in Shape Memory Alloys," TMS 2013 Annual Meeting, San Diego, CA, February 16-20, 2014.
11. R. Vaidyanthan (invited):"Dependence of the Deformation Behavior of Shape Memory NiTi on Thermomechanical Loading Paths," THERMEC 2013, Las Vegas, NV, December 2-6, 2013.
12. D.E. Nicholson, O. Benafan, S.A. Padula II, R.D. Noebe and R. Vaidyanathan. "Thermomechanical behavior of NiTiPdPt high temperature shape memory alloy springs," Smart Mater Struct 23 (2014) 125009
13. O. Benafan, A. Garg, R.D. Noebe, G.S. Bigelow, S.A. Padula II, D.J. Gaydosh, N. Schell, J.H. Mabe and R. Vaidyanathan, "Mechanical and functional behavior of a Ni-rich Ni 50.3Ti29.7 Hf20 high temperature shape memory alloy," Intermetallics, 50 (2014) 94-107
14. O. Benafan, R.D. Noebe, S.A. Padula II, D.W. Brown, S. Vogel and R. Vaidyanathan, "Thermomechanical cycling of a NiTi shape memory alloy macroscopic response and microstructural evolution," Int J Plasticity, 56 (2014) 99-118.
15. O. Benafan, R.D. Noebe, S.A. Padula II, D.J. Gaydosh, B.A. Lerch, A. Garg, G.S. Bigelow, K. An and R. Vaidyanathan, "Temperature dependent behavior of a polycrystalline NiTi shape-memory alloy around the transformation regime," Scripta Mater, 68 8 (2013) 571.
16. O. Benafan, S.A. Padula II, R.D. Noebe, D.W. Brown, B. Clausen and R. Vaidyanathan, "An in situ neutron diffraction study of shape setting shape-memory NiTi," Acta Mater, 61 10 (2013) 3585-3599.
17. O. Benafan, R.D. Noebe, S.A. Padula II, and R. Vaidyanathan, "Microstructural Response during Isothermal and Isobaric Loading of a Precipitation Strengthened Ni-29.7Ti-20Hf High-Temperature Shape Memory Alloy," Met Trans A, 43 A (2012) 4539.
18. S. Padula II, S. Qiu, D. Gaydosh, R. Noebe, G. Bigelow, A. Garg and R. Vaidyanathan, "Effect of Upper-Cycle Temperature on the Load-biased, Strain-Temperature Response of NiTi," Met Trans A, 43 A (2012) 4610.
19. O. Benafan, S.A. Padula, II, R.D. Noebe, T.A. Sisneros, and R. Vaidyanathan, "Role of B19′ martensite deformation in stabilizing two-way shape-memory behavior in NiTi," J Appl Phys, 112 (2012) 093510.

5.0 Table

TABLE 1.—THE ROLE OF MATERIAL-PARAMETERS GROUPING AND ACTIVATION-DEACTIVATION MODELING FEATURES IN HANDLING THE CONCURRENT PARAMETERIZATIONS OF FOUR SMA MATERIALS INTENDED FOR WIDELY-VARYING APPLICATIONS (SEE SECTION 2.2.3).

Model parameters	Material system			
	$Ni_{50.3}Ti_{29.7}Hf_{20}$	$Ni_{49.9}Ti_{50.1}$	Powder metallurgical NiTi	Superelastic NiTi
Fixed parameters	E, υ; n, μ, d; $H(b)$, $\beta(b)$ for b=1-6	E, υ; n, μ; $H(b)$, $\beta(b)$ *for* b=1-6	E, υ; n, μ, κ; $\kappa(b)$ for b=3, 5, and 6, $H(b)$, $\beta(b)$ for b=1-6	E, υ; n, μ, κ; $\kappa(b)$, $H(b)$, $\beta(b)$ for b=1-6
Temperature-dependent thresholds parameters	$\kappa(b)$ for b=1, 2, and 4	κ; $\kappa(b)$ for b=1, 2, 4, and 5	$\kappa(b)$ for b=1, 2, and 4	X
Stress-dependent thresholds parameters	κ; $\kappa(b)$ for b=1, 2, 3, and 5	κ; $\kappa(b)$ for b=1, 2, 5, and 6	X	X
ATC parameters	c (stress dependent)	X	X	X
T_{shift} parameter	Stress dependent	X	X	X

Note: X= deactivated

Elastic (standard/handbook) parameters: E, υ

Flow and ATC parameters: n, μ, κ, c, d

Hardening-mechanism parameters: $\kappa(b)$, $H(b)$ and $\beta(b)$ for b = 1 to 6

6.0 Figures

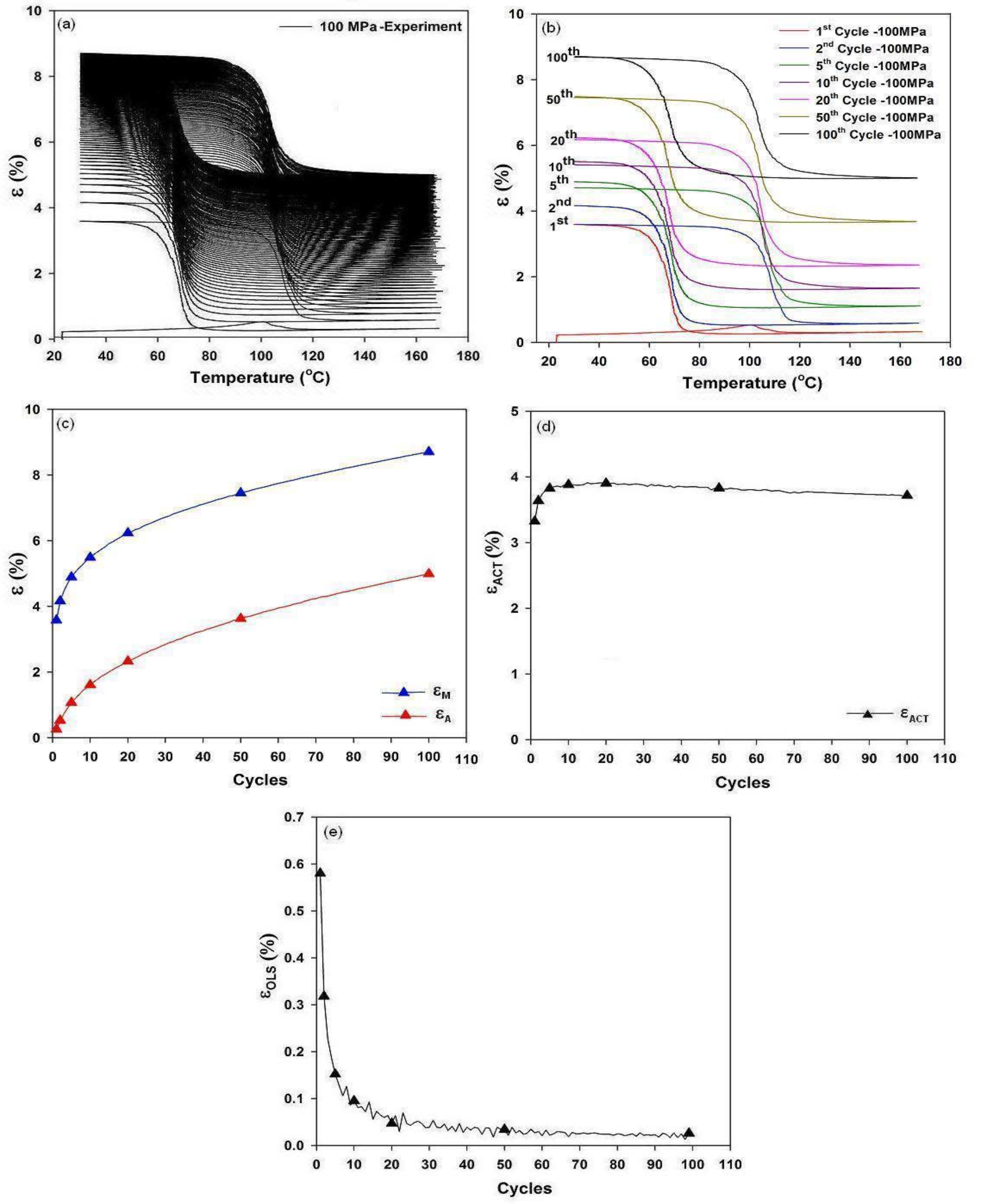

Figure 1.—Cyclic response (100 thermal cycles) for an isobaric test at bias stress of 100 MPa and a UCT of 165 °C: (a) experimental (Courtesy: Dr. Santo A. Padula II, NASA GRC), (b) 3D multimechanism SMA model, (c) strain at martensite (ε_M) and austenite (ε_A) with cycles, (d) actuation strain (ε_{ACT}) with cycles, and (e) open loop strain (ε_{OLS}) at martensite with cycles.

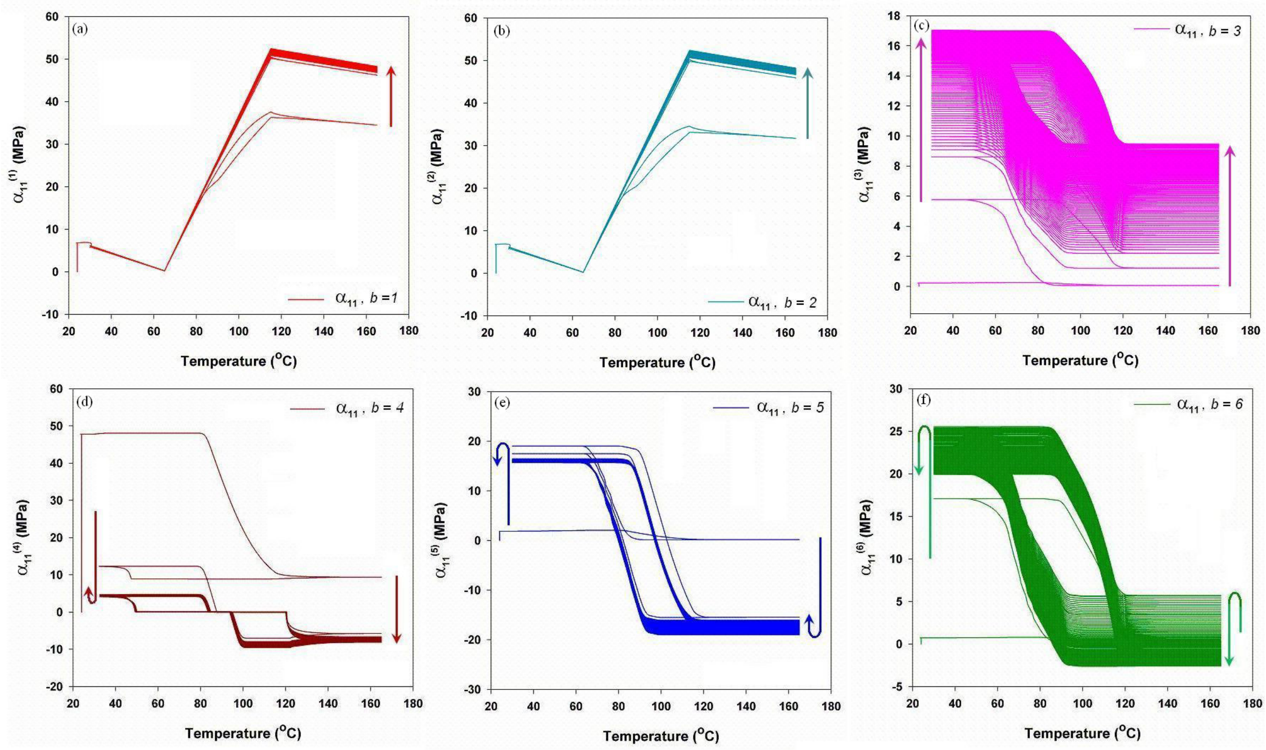

Figure 2.—Evolution of internal stress, α_{11}, during isobaric test at 100 MPa using SMA Model in the calibration of $Ni_{49.9}Ti_{50.1}$, for: (a) mechanism b =1, (b) mechanism b =2, (c) mechanism b =3, (d) mechanism b =4, (e) mechanism b =5, and (e) mechanism b =6.

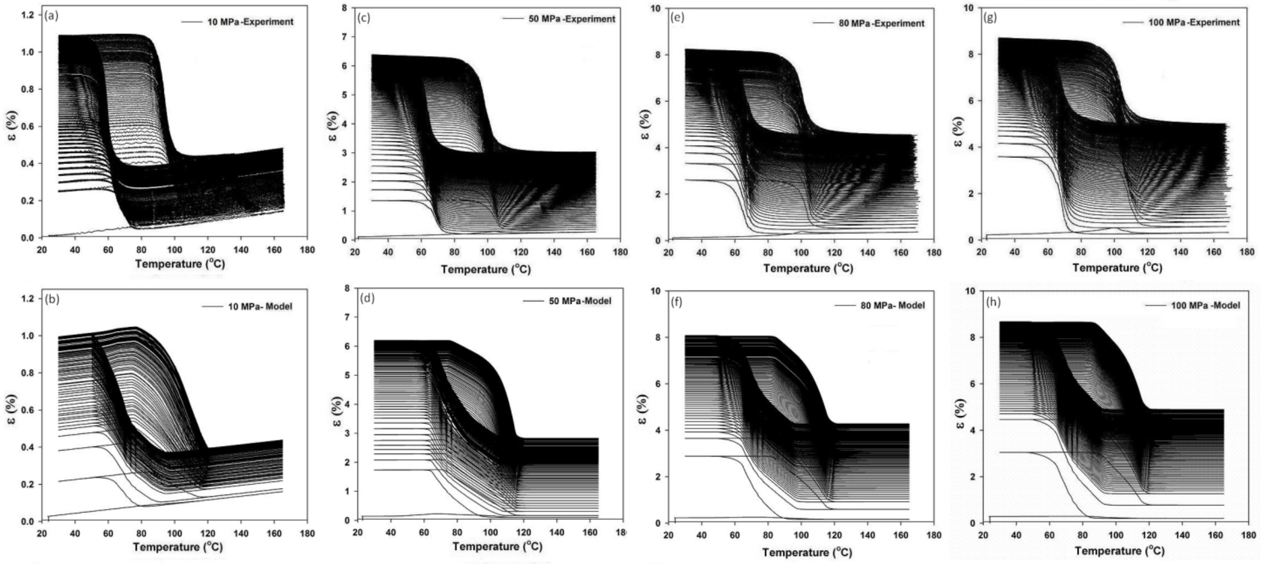

Figure 3.—Strain versus temperature response (100 cycles) for a isobaric test of $Ni_{49.9}Ti_{50.1}$: (a) 10 MPa-Experimental, (b) 10 MPa-SMA Model, (c) 50 MPa-Experimental,(d) 50 MPa-SMA Model, (e) 80 MPa-Experimental,(f) 80 MPa-SMA Model, (g) 100 MPa-Experimental, and (h) 100 MPa-SMA Model.

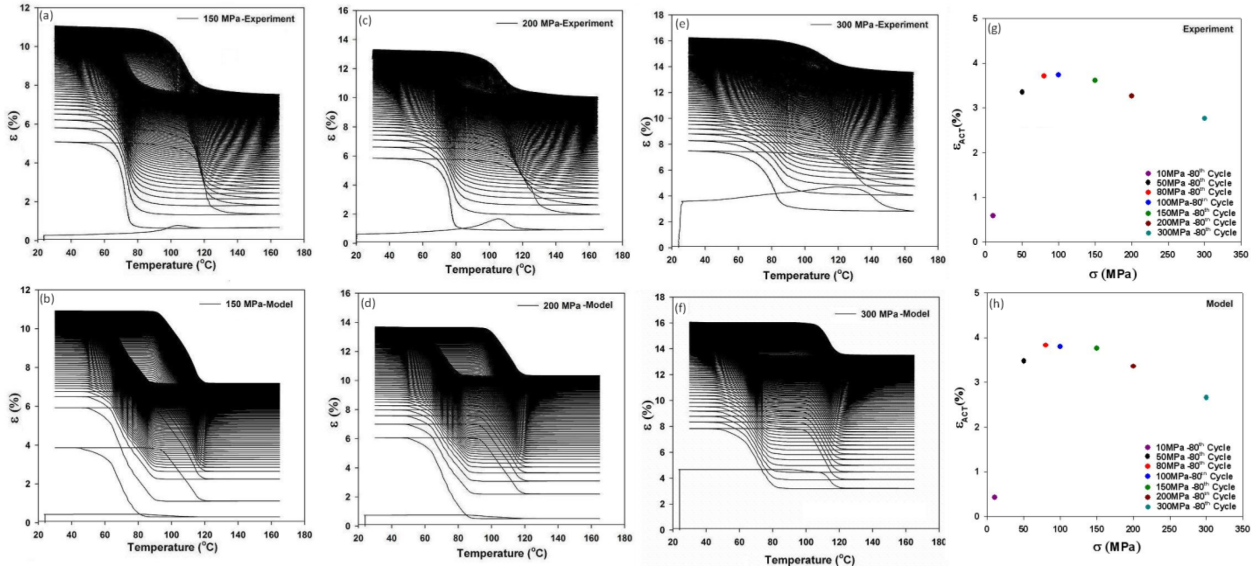

Figure 4.—Strain versus temperature response (100 cycles in all except 88 cycles in the 200 MPa case) for a isobaric test of $Ni_{49.9}Ti_{50.1}$: (a) 150 MPa- Experimental,(b) 150 MPa-SMA Model, (c) 200 MPa-Experimental, (d) 200 MPa-SMA Model, (e) 300 MPa-Experimental, and (f) 300 MPa-SMA Model. Variation of actuation stain with engineering stress levels 10, 50, 80, 100, 150, 200, and 300 MPa: (g) Experimental, and (h) SMA Model.

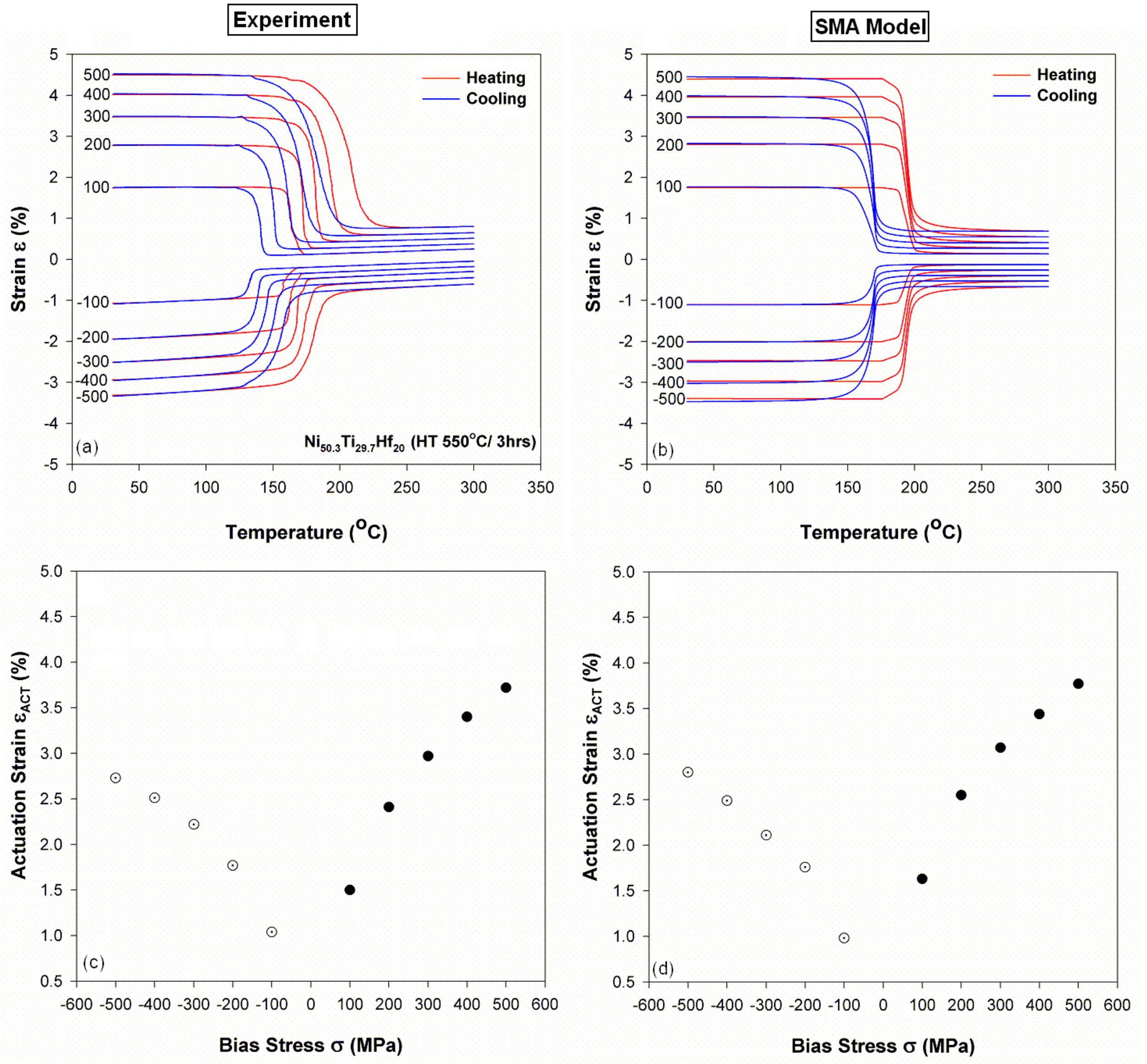

Figure 5.—Calibration of the SMA material model for Ni$_{50.3}$Ti$_{29.7}$ Hf$_{20}$: (a), (b): Cyclic response (2nd thermal cycle) for a series isobaric test between LCT of 30 °C and UCT of 300 °C at bias stress in tension (from 100 to 500 MPa with increment of 100 MPa) followed by compression (from –100 to –500 MPa with increment of –100 MPa): (a) Experiment, and (b) SMA Model. (c), (d): Actuation strains at each stress levels in this test: (c) Experiment, and (d) SMA Model.

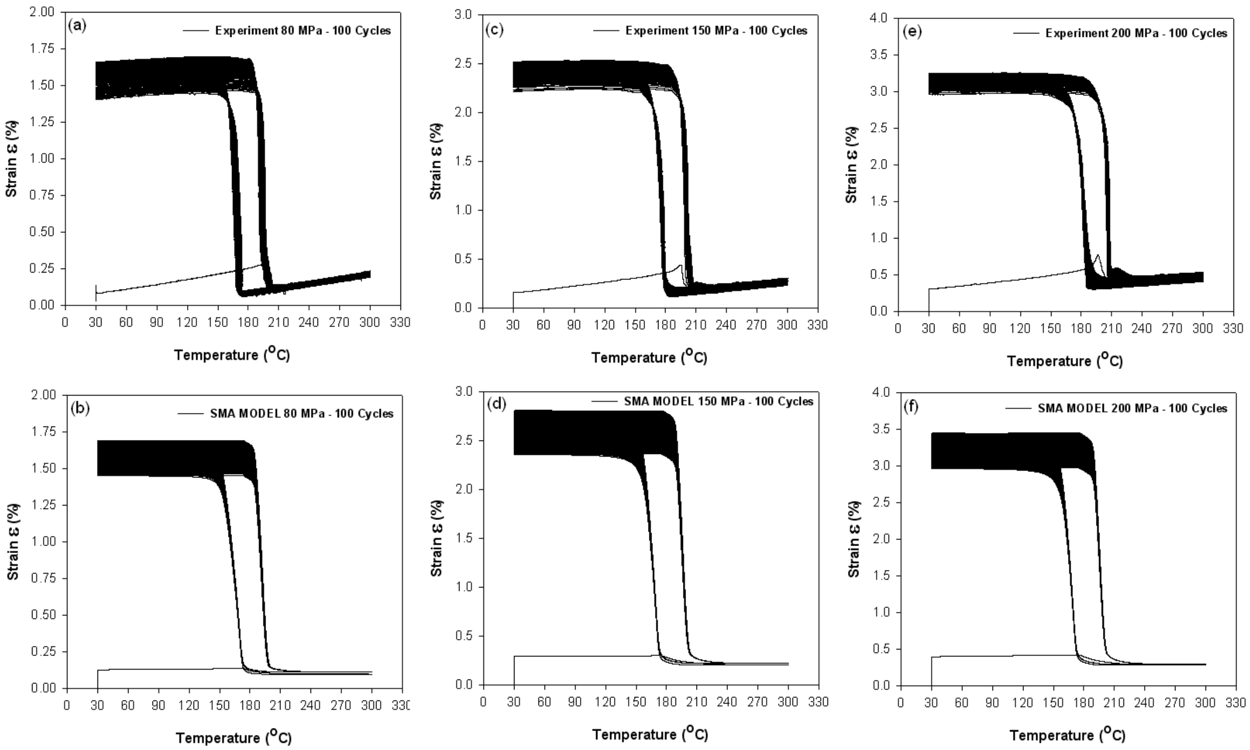

Figure 6.—Strain versus temperature response (100 cycles) for $Ni_{50.3}Ti_{29.7}Hf_{20}$: (a) 80 MPa-Experimental, (b) 80 MPa-SMA Model, (c) 150 MPa-Experimental, (d) 150 MPa-SMA Model, (e) 200 MPa-Experimental, and (f) 200 MPa-SMA Model.

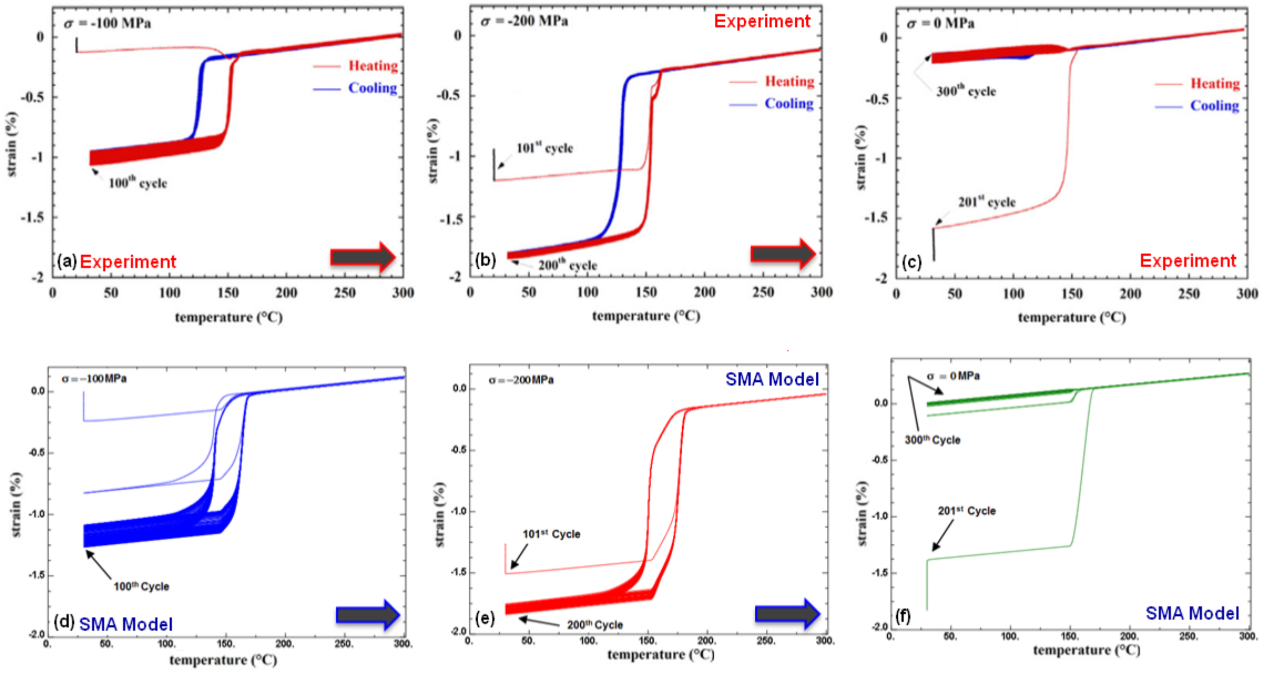

Figure 7.—Experimental ((a) → (b) → (c)) and model ((d→ (e) → (f)) isobaric strain versus temperature response of the $Ni_{50.3}Ti_{29.7}Hf_{20}$ alloy at a series of –100 → –200→ 0 MPa stress histories. One hundred thermal cycles are performed on the specimen after each stress level.

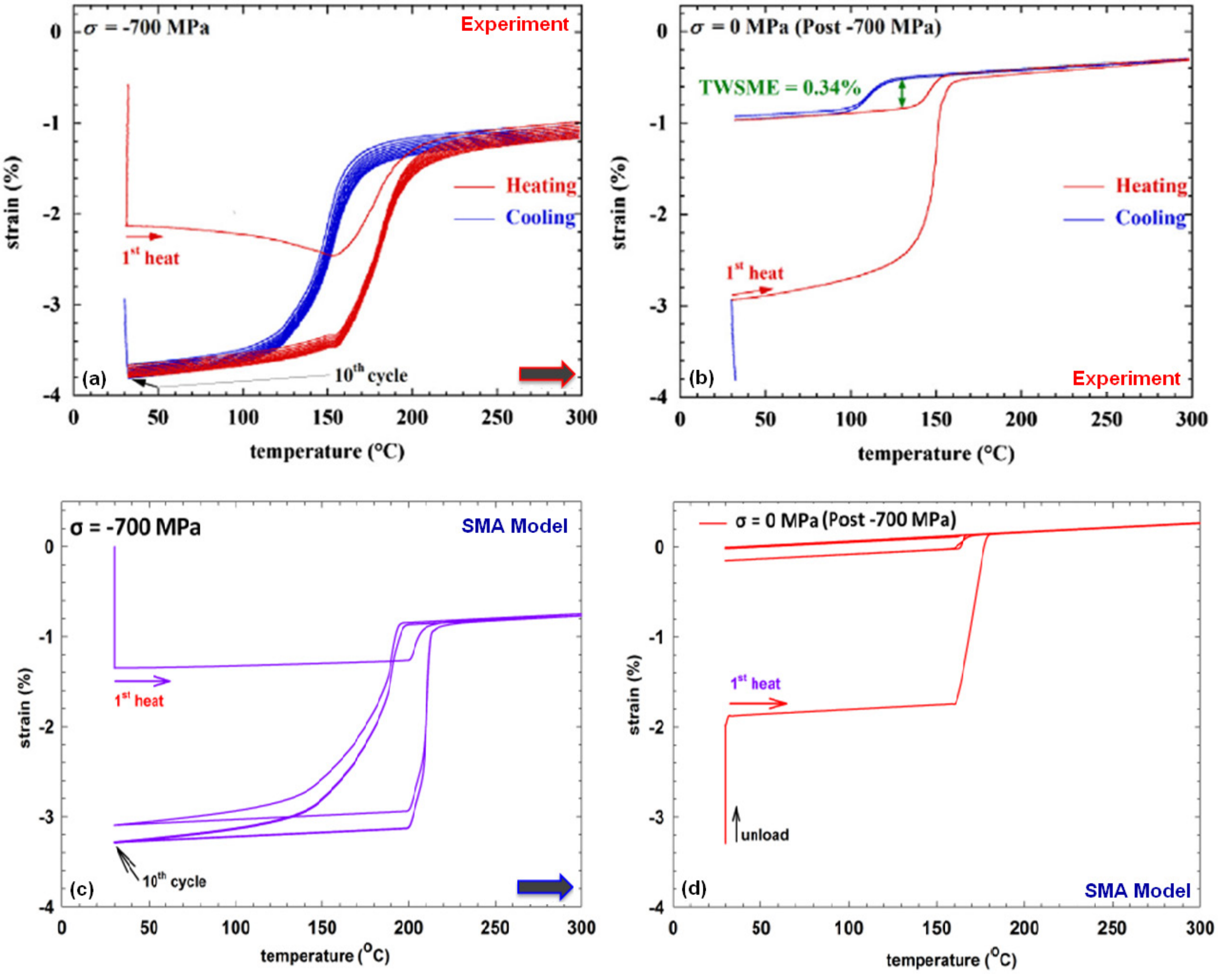

Figure 8.—Experimental ((a) → (b)) and model ((c) → (d)) compressive isobaric strain versus temperature response of the $Ni_{50.3}Ti_{29.7}Hf_{20}$ alloy at stresses of –700 and 0 MPa. Ten thermal cycles are performed at the end of the –700 MPa stress level as well as at the stress-free (0 MPa) stages of the test procedure.

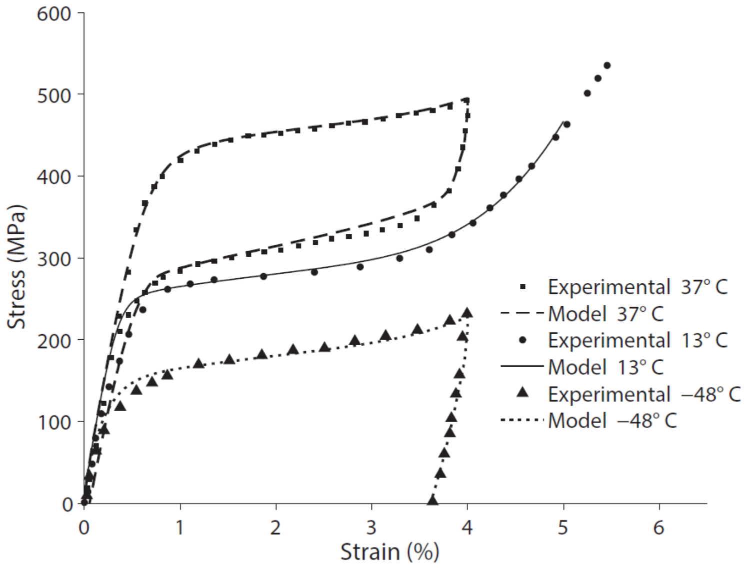

Figure 9.—Isothermal stress-strain diagram for a powder metallurgically processed NiTi tested at 37, 13, and –48 °C showing a comparison of the experimental and model results. Test data was taken from Krone et al. (2005) and Christ and Reese (2009).

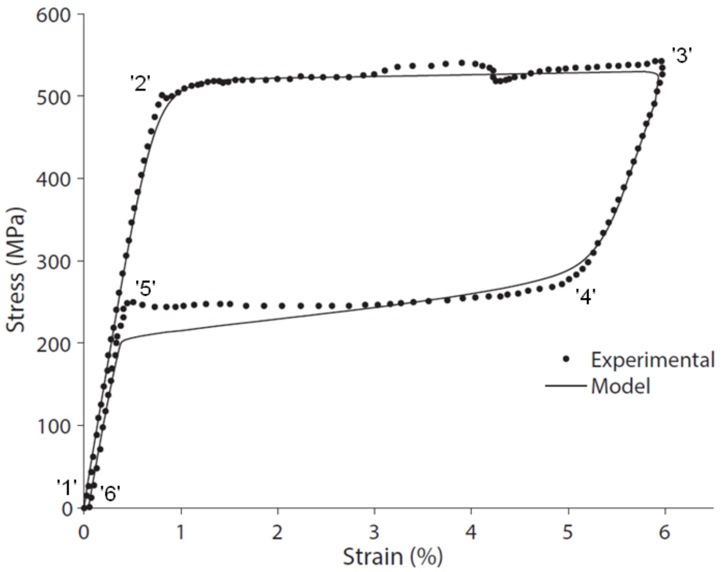

Figure 10.—Comparison of calibrated SMA model and experimental (Liu et al. 2008): stress versus strain response for the superelastic $Ni_{50.7}Ti_{49.3}$ at body temperature 37 °C, under combined control, i.e., strain control during loading to 6% and stress control to zero stress at end of the unload.

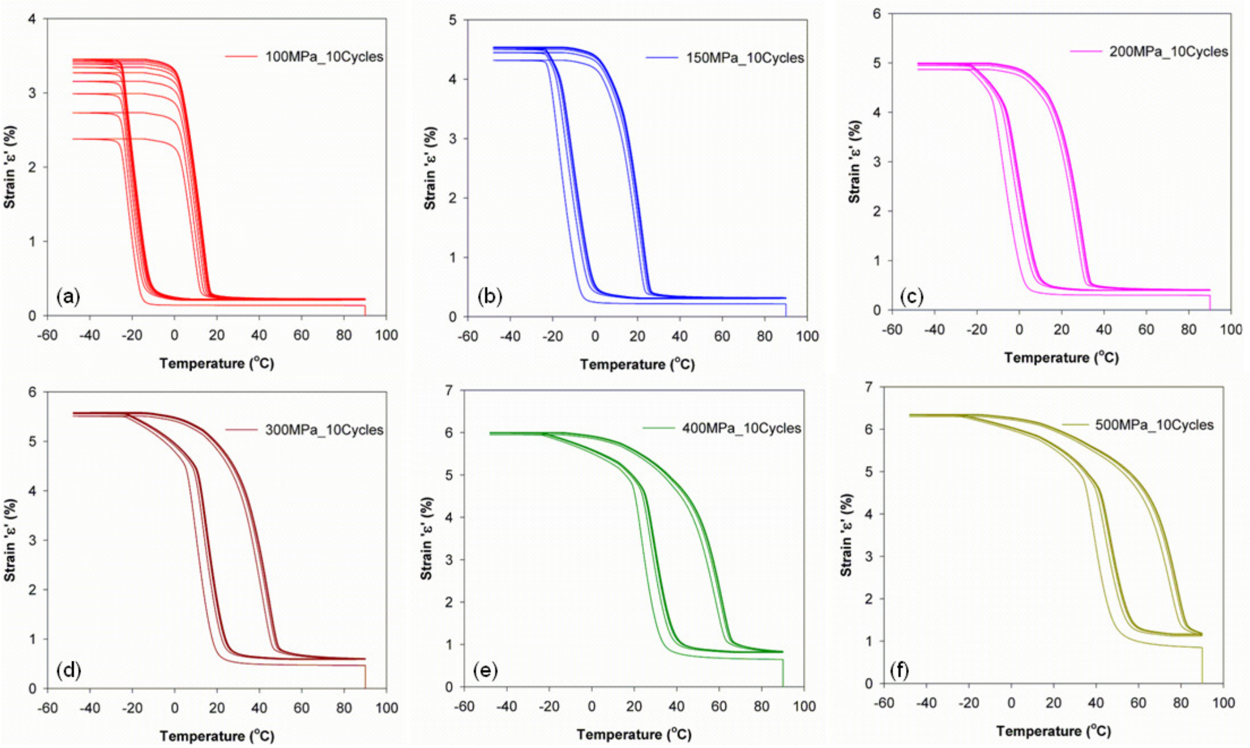

Figure 11.—Strain versus temperature response of the isobaric test for thermal cycles between LCT of –50 °C and UCT of 90 °C at different bias-stress levels of: (a) 100 MPa, (b) 150 MPa, (c) 200 MPa, (d) 300 MPa, (e) 400 MPa, and (f) 500 MPa. The isothermal loadings to this bias-stress levels were performed at UCT = 90 °C.

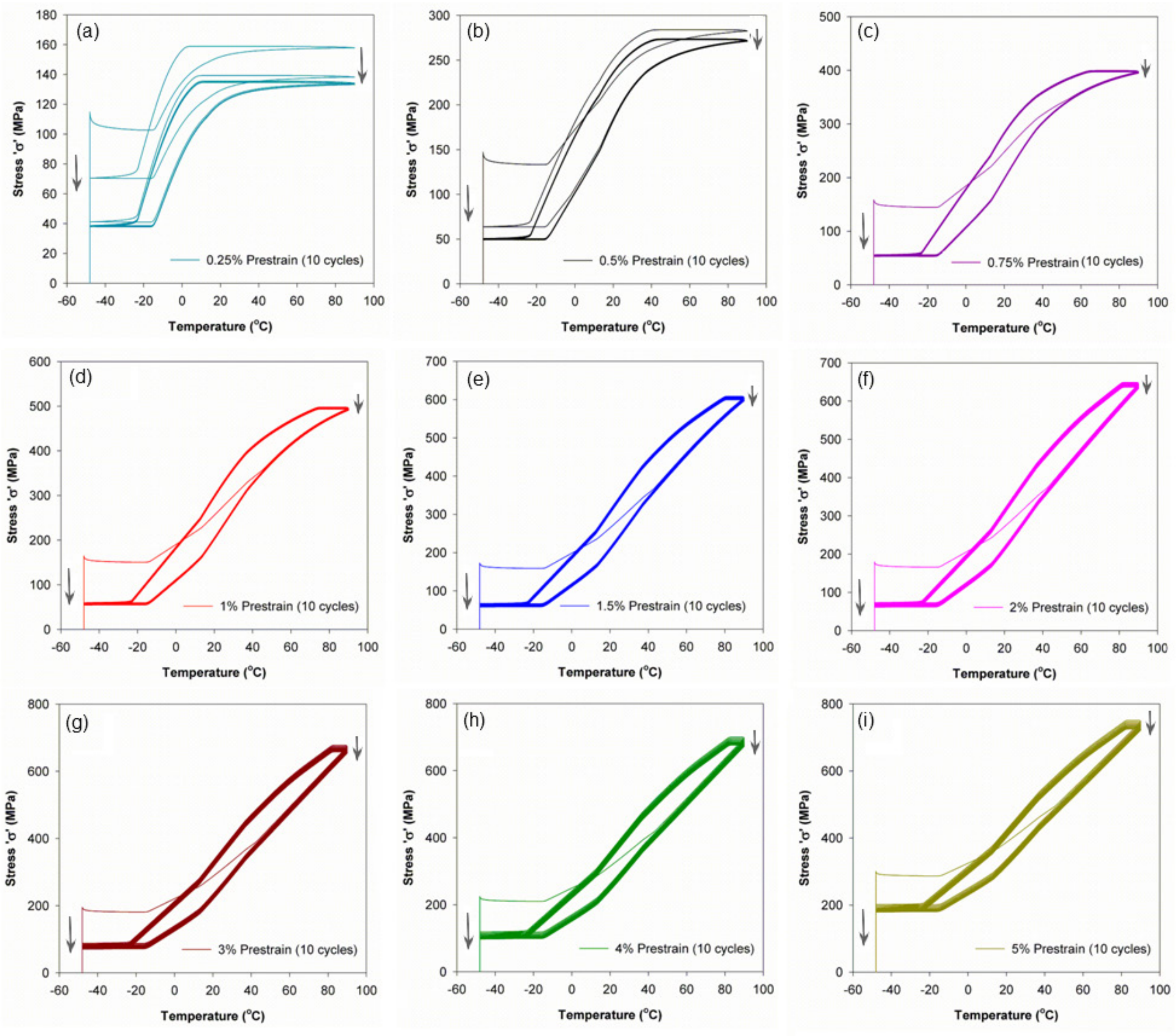

Figure 12.—Stress versus temperature response of the isostrain test for thermal cycles between LCT of –50 °C and UCT of 90 °C at different bias-strain levels of : (a) 0.25%, (b) 0.5%, (c) 0.75%, (d) 1%, (e) 1.5%, (f) 2%, (g) 3%, (h) 4%, and (i) 5%. The isothermal loadings to this bias-strain levels were performed at LCT = -50 °C.

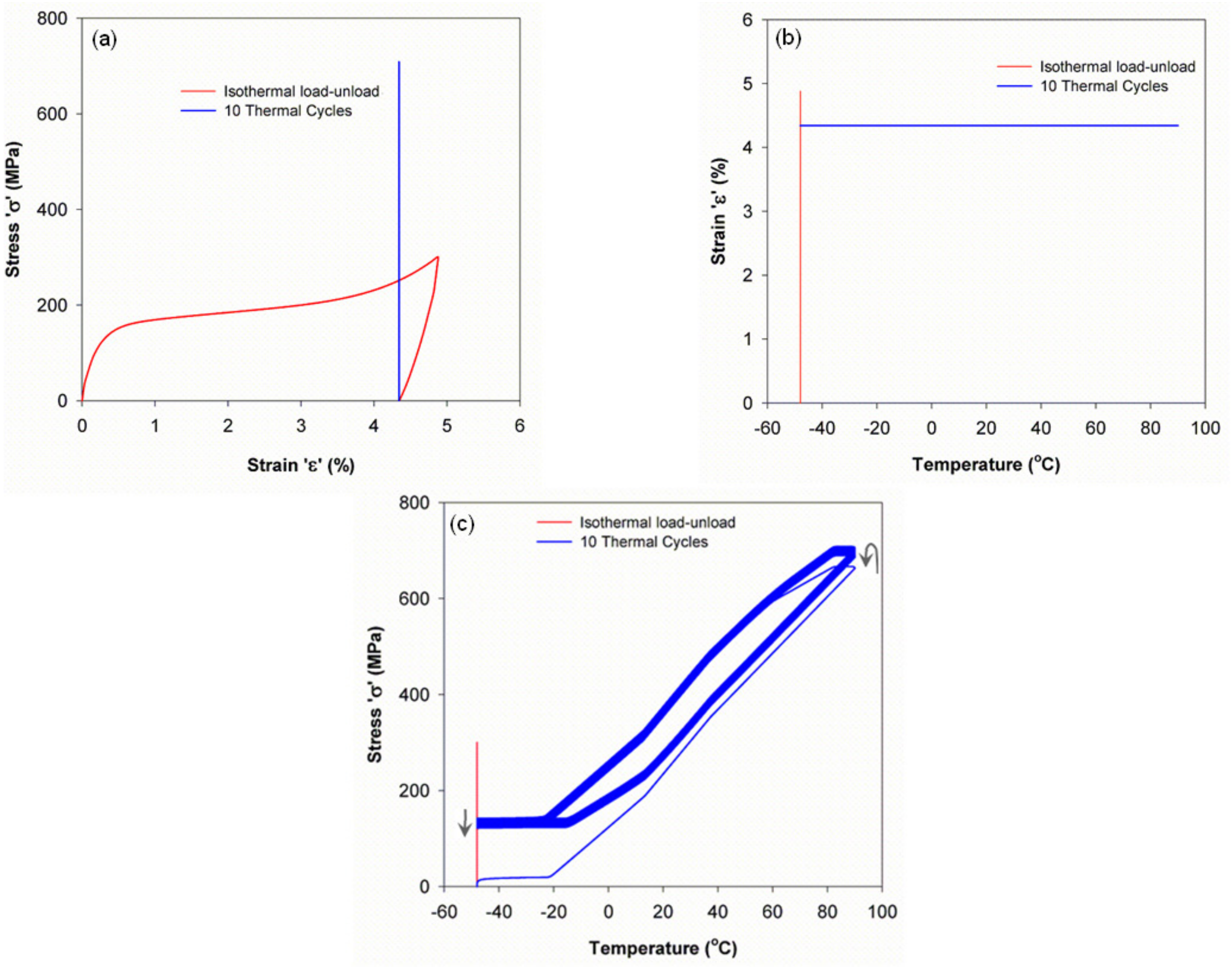

Figure 13.—Constrained recovery test involving the isothermal load-unload at LCT = –50 °C, followed by10 thermal cycles between LCT = –50 °C and UCT = 90 °C at the constrained strain (residual strain after the unload at –50 °C) condition: (a) stress versus strain response, (b) strain versus temperature response, and (c) stress versus temperature response.

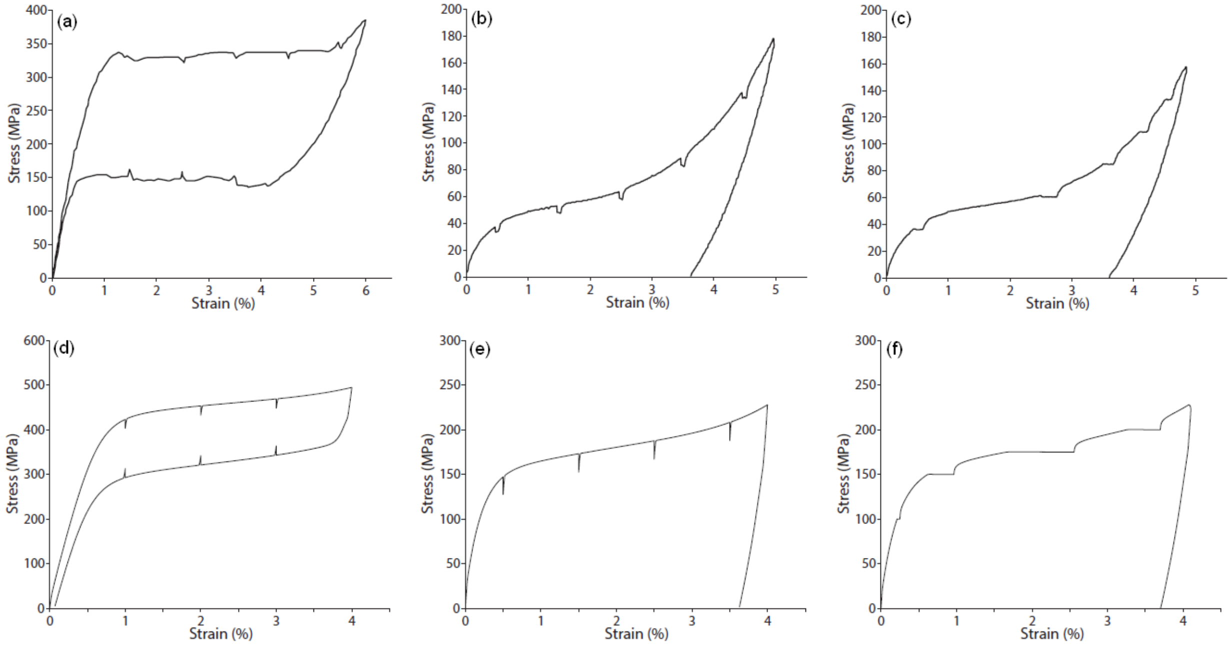

Figure 14.—Parts (a) and (b) demonstrates the stress relaxation phenomena during multiple periods of strain holding at temperature higher than A_f (a) and lower than M_f (b), and Part (c) shows the creep phenomena during the multiple periods of stress holding at temperature lower than Mf, as experimentally determined by Helm (2001). The respective Parts (d) to (e) show analogous results as obtained from the simulation of the characterized PM-NiTi-P SMA material uniaxial, isothermal, tension tests.

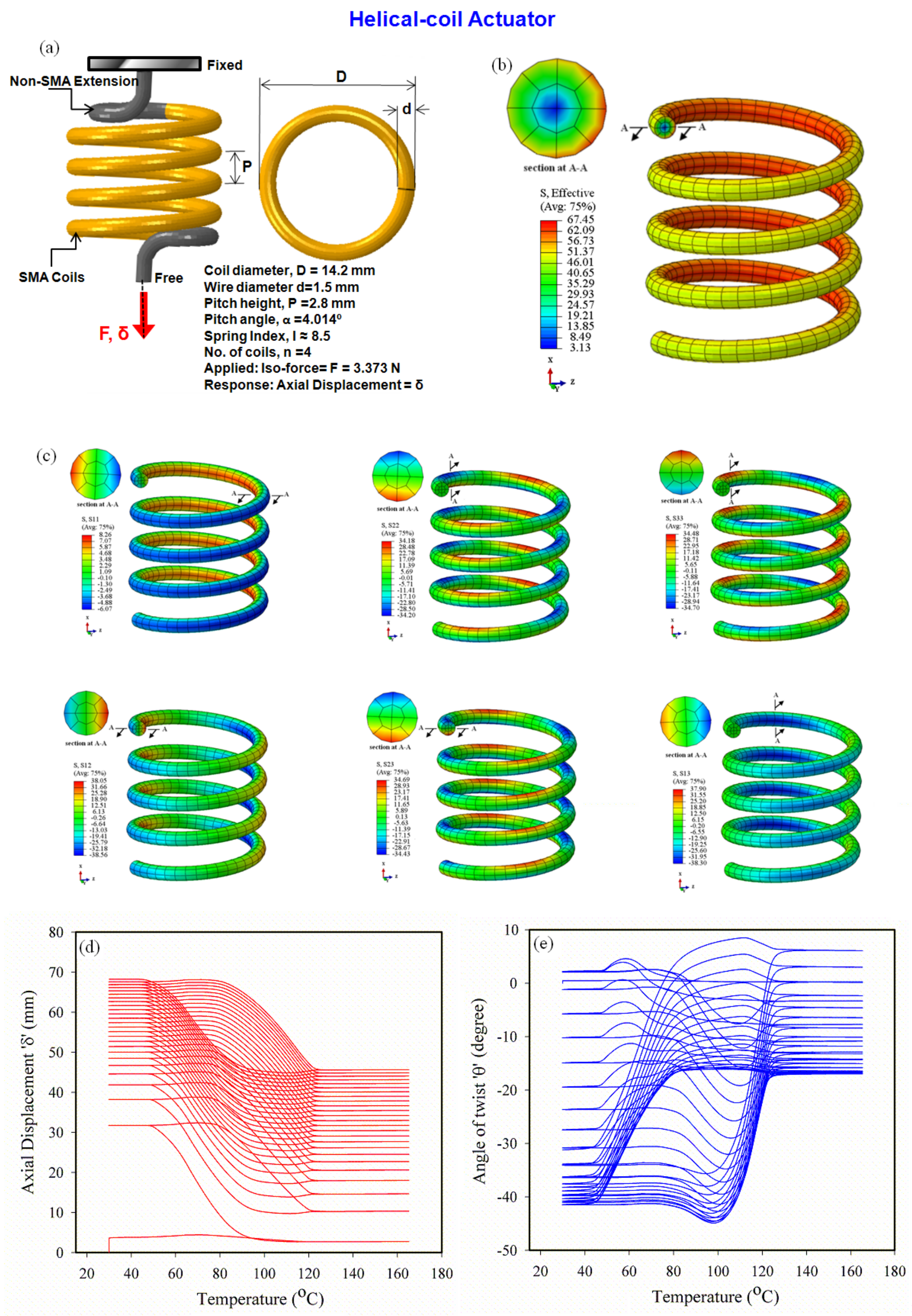

Figure 15.—Large scale simulation of four-coil helical spring actuator using SMA multi-mechanism framework calibrated for Ni$_{49.9}$Ti$_{50.1}$: (a) Geometry, load and boundary conditions, (b) distribution of effective stress in SMA coil at the end of applied load (3.373 N) (note the significant nonuniformity/inhomogeneity in different parts of the coils, and especially over the cross section of the wire), (c) distribution of the components of the stress state in SMA coils at the end of applied load, clearly demonstrating the genuine three-dimensionality of the state, (d) axial displacement(primary response) ‘δ’ versus temperature (25 cycles), and (e) angle of twist (secondary response) ‘θ’ versus temperature (25 cycles). Demonstrating the genuine three-dimensionality of the state, (d) axial displacement (primary response) ‘δ’ versus temperature (25 cycles), and (e) angle of twist (secondary response) ‘θ’ versus temperature (25 cycles).

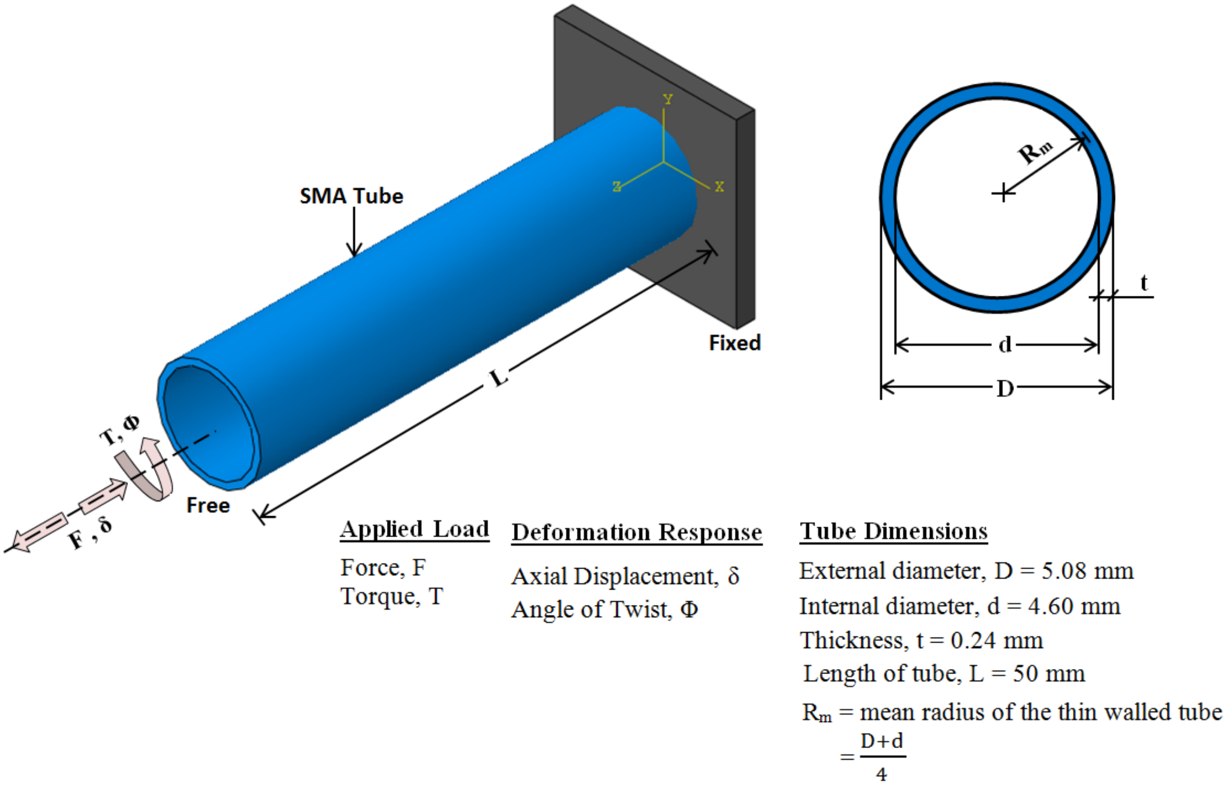

Figure 16.—Geometric details and load conditions for the SMA tube being utilized in the study.

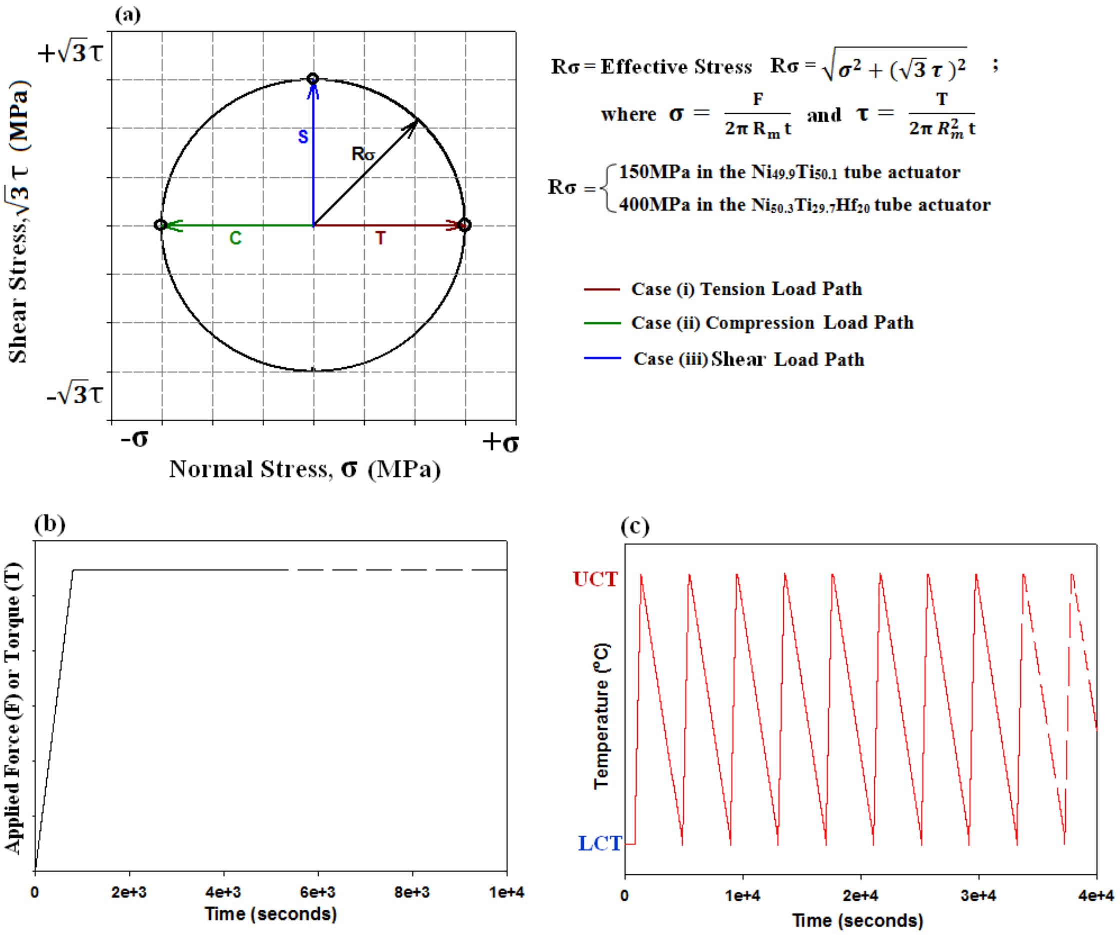

Figure 17.—Details of the “isobaric” loading programs considered in the study highlighting (a) a description of the loading paths taken for the different tests (i.e., tension, compression and/or shear), (b) the nature of the isothermal loading phase, and (c) aspects of the subsequent thermal-cycling phase.

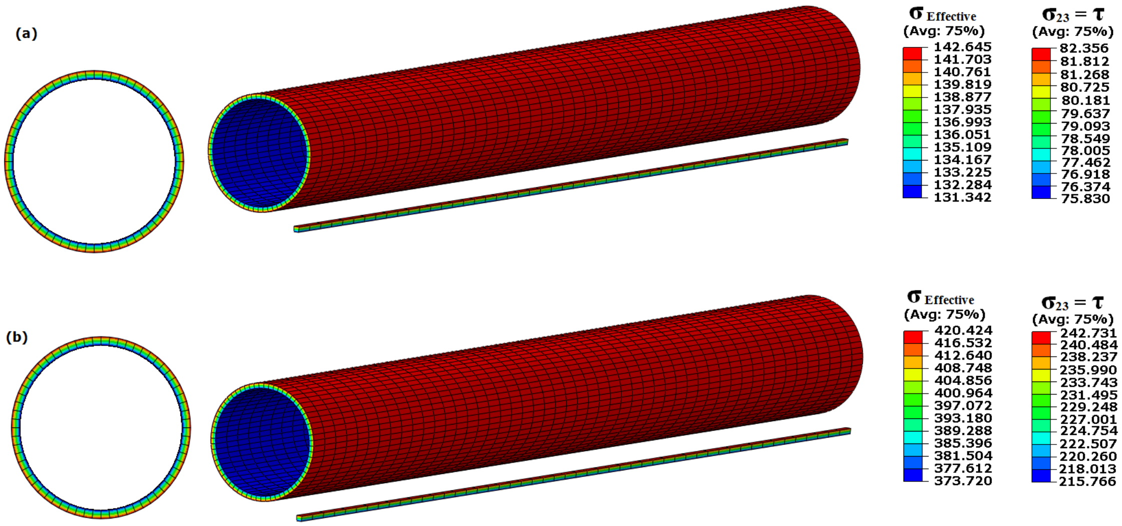

Figure 18.—Distribution of the effective and shear stresses in (a) the $Ni_{49.9}Ti_{50.1}$, and (b) the $Ni_{50.3}Ti_{29.7}Hf_{20}$ SMA tube at the end of the isothermal, torsional loading phase. Note the nonuniformity/inhomogeneity in the distribution of the stresses over the cross section of the relatively thin tube (here, the axisymmetric tube model is swept about 360° to show the full view of tube).

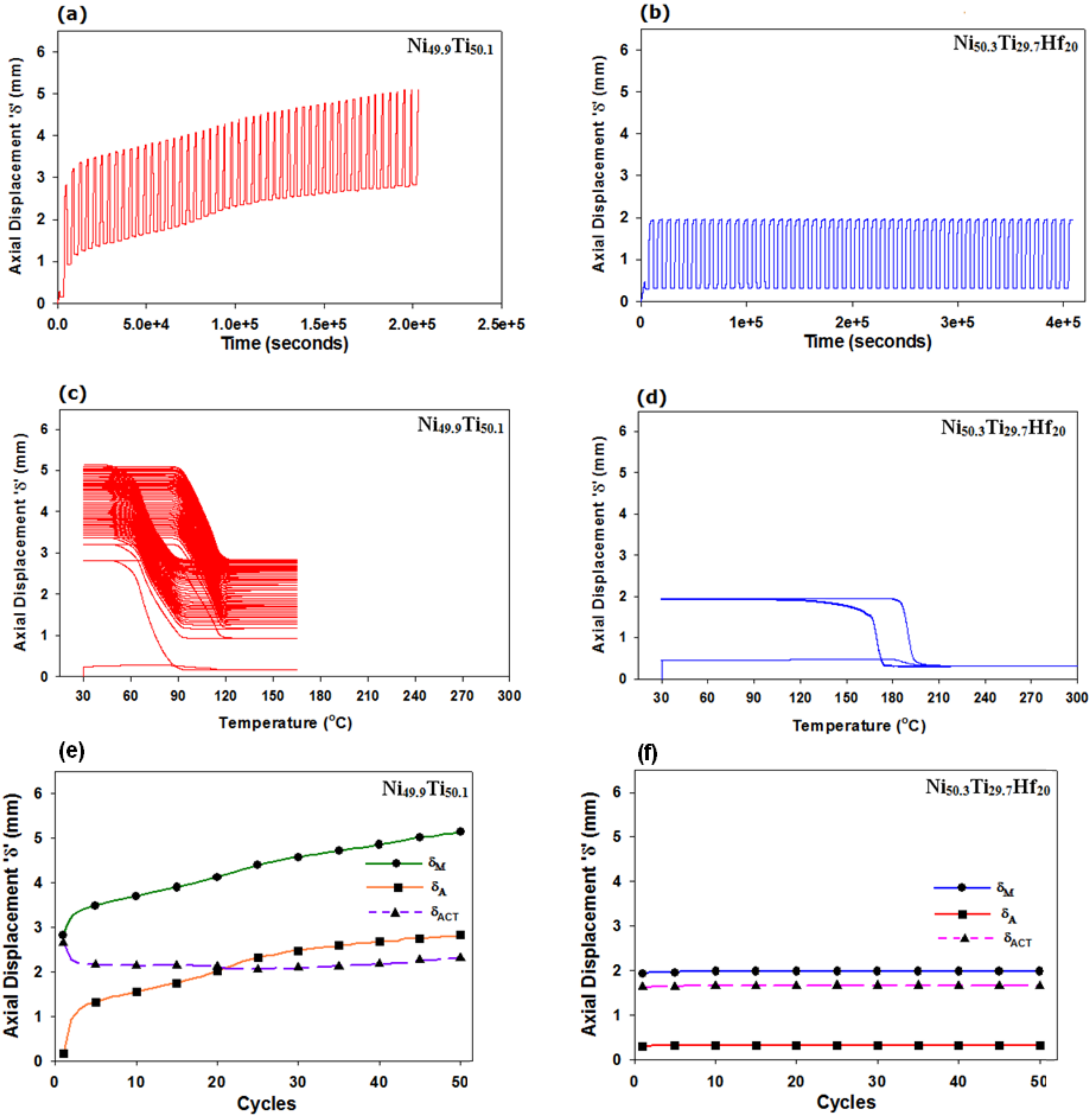

Figure 19.—Evolutionary response of the axial displacement versus time, axial displacement versus temperature, and axial displacements at martensite (δ_M), austenite (δ_A) with the corresponding actuation stroke $\delta_{ACT} = \delta_M - \delta_A$ for 50 thermal cycles under tensile, isoforce thermal cycling condition for ((a), (c), (e)) $Ni_{49.9}Ti_{50.1}$ and ((b), (d), (f)) $Ni_{50.3}Ti_{29.7}Hf_{20}$ tube actuators, respectively.

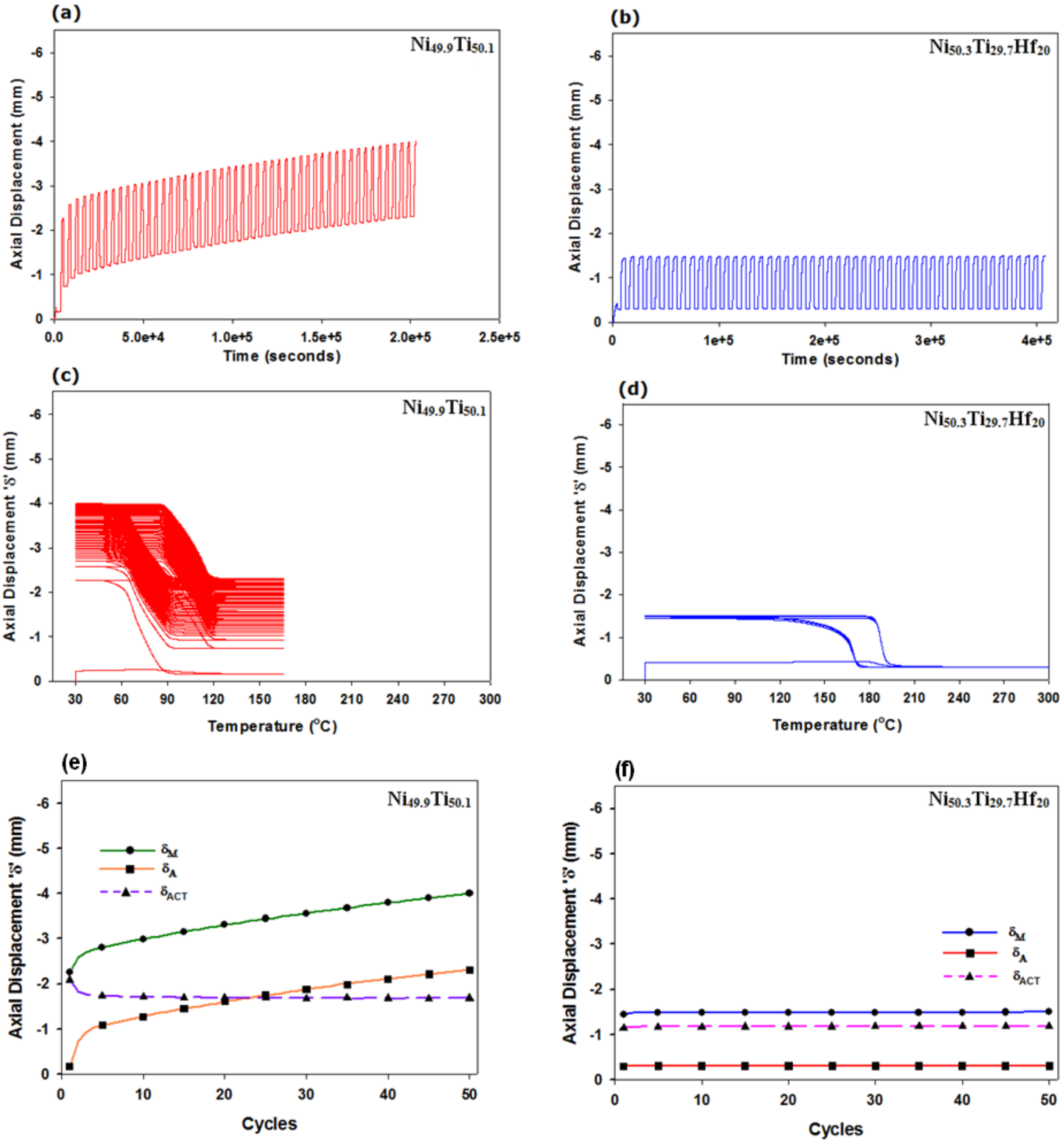

Figure 20.—Evolutionary response of the axial displacement versus time, axial displacement versus temperature, and axial displacements at martensite (δ_M), austenite (δ_A) with the corresponding actuation stroke $\delta_{ACT} = \delta_M - \delta_A$ for 50 thermal cycles under compressive, isoforce thermal cycling condition for ((a), (c), (e)) $Ni_{49.9}Ti_{50.1}$ and ((b), (d), (f)) $Ni_{50.3}Ti_{29.7}Hf_{20}$ tube actuators, respectively.

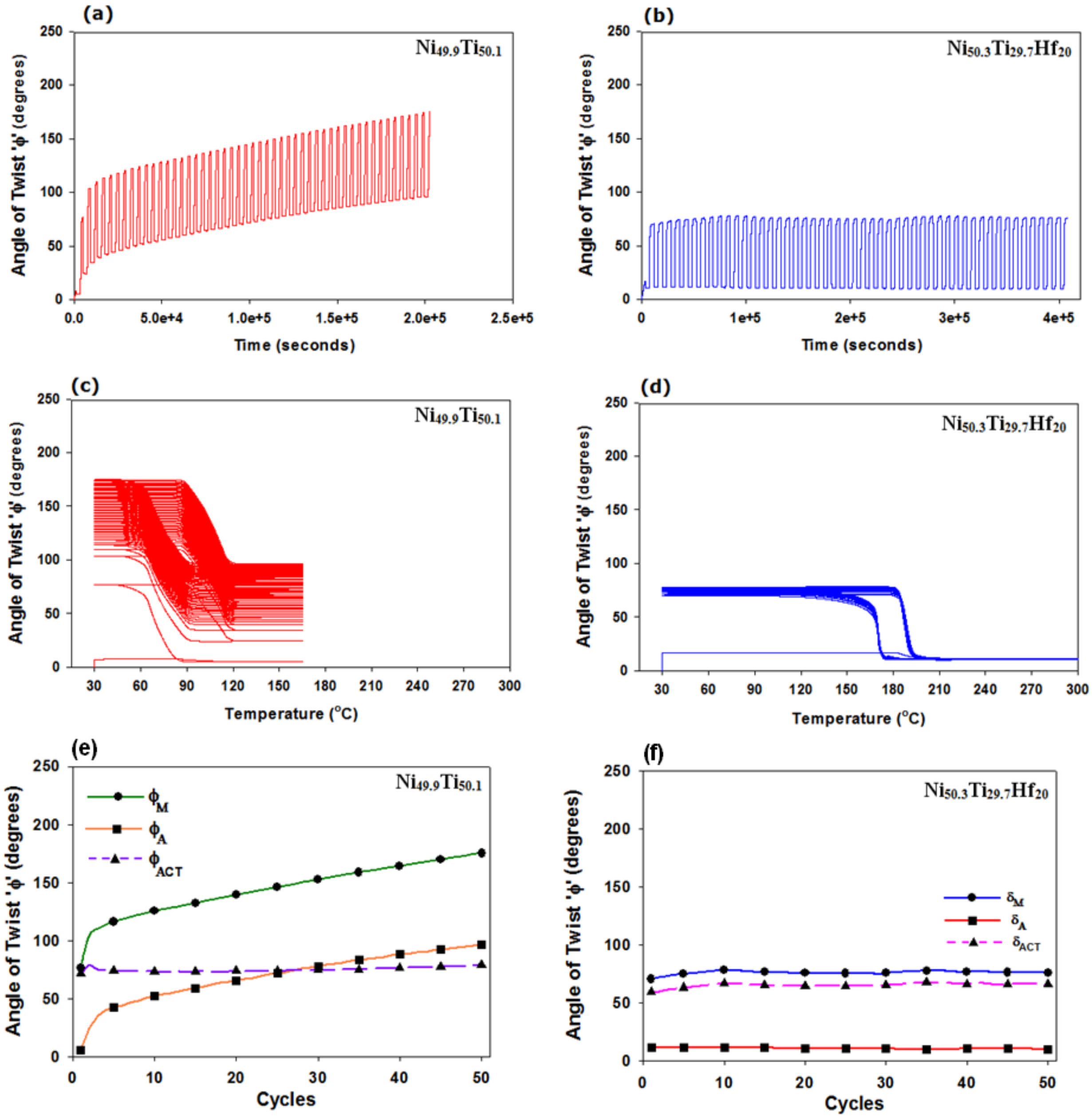

Figure 21.—Evolutionary response of the angle of twist versus time and angle of twist versus temperature, and angle of twist at martensite (Φ_M),austenite (Φ_A) with the corresponding actuation stroke $\sqrt{}_{ACT} = \Phi_M - \Phi_A$ for 50 thermal cycles under isotorque thermal cycling condition for (a, c, e) $Ni_{49.9}Ti_{50.1}$ and (b, d, f) $Ni_{50.3}Ti_{29.7}Hf_{20}$ tube actuators, respectively.

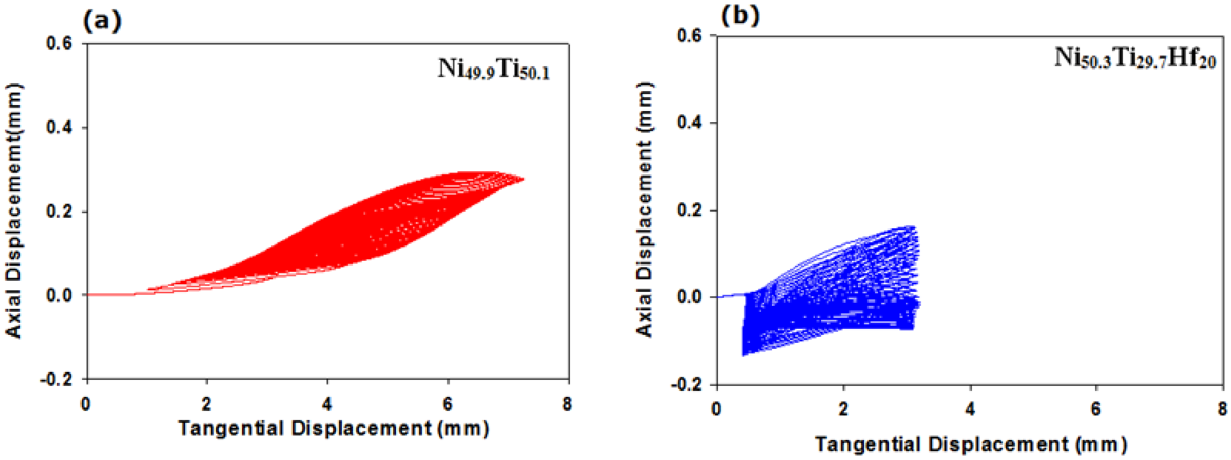

Figure 22.—Plots of the secondary axial displacement response versus the associated primary tangential displacement for: (a) the $Ni_{49.9}Ti_{50.1}$ and (b) the $Ni_{50.3}Ti_{29.7}Hf_{20}$ tube actuators under isotorque thermal cycling. Note that the scale of secondary axial displacement response is one-tenth of the scale of the primary tangential displacement response. Also note that the tangential displacement defined in these figures is calculated as $(R_m \cdot \Phi)\sqrt{3}$, where Φ is the angle of twist (in radians) at the free-end of the tube and R_m is the mean radius of its section.

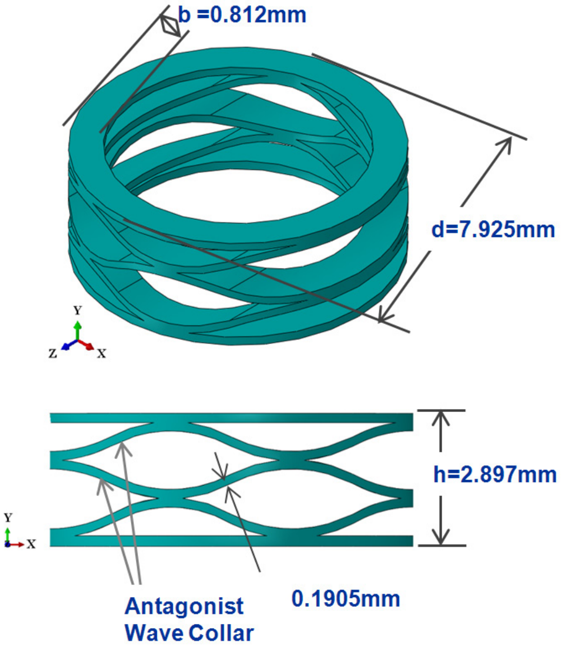

Figure 23.—Geometric details of the wave spring.

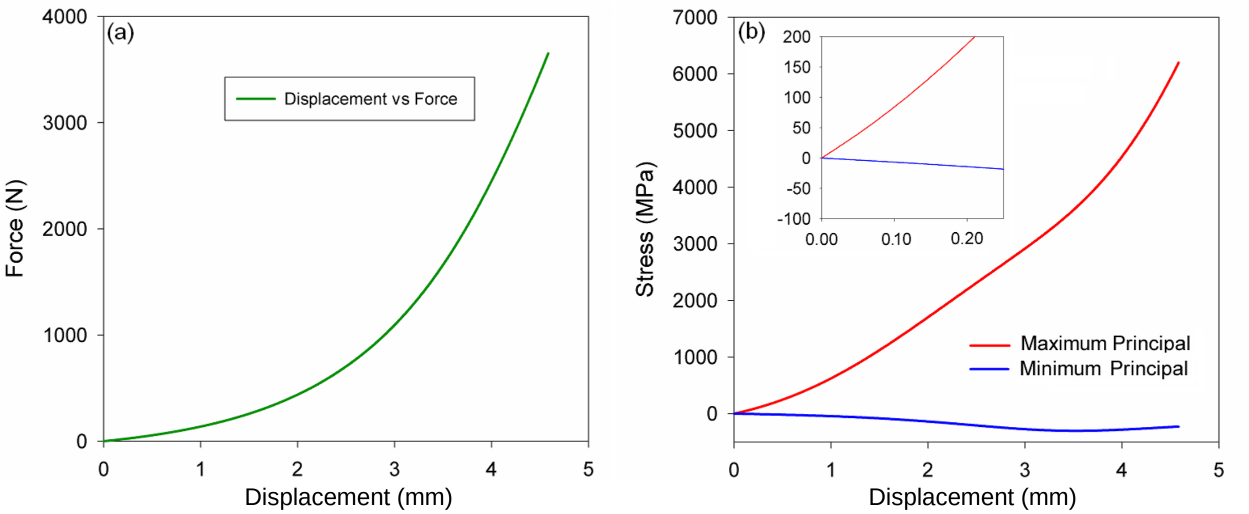

Figure 24.—(a) Load versus deflection response of the elastic wave spring; and (b) Maximum and minimum principal stresses at a generic element in the mid of the wave spring collar with respect to the applied displacement.

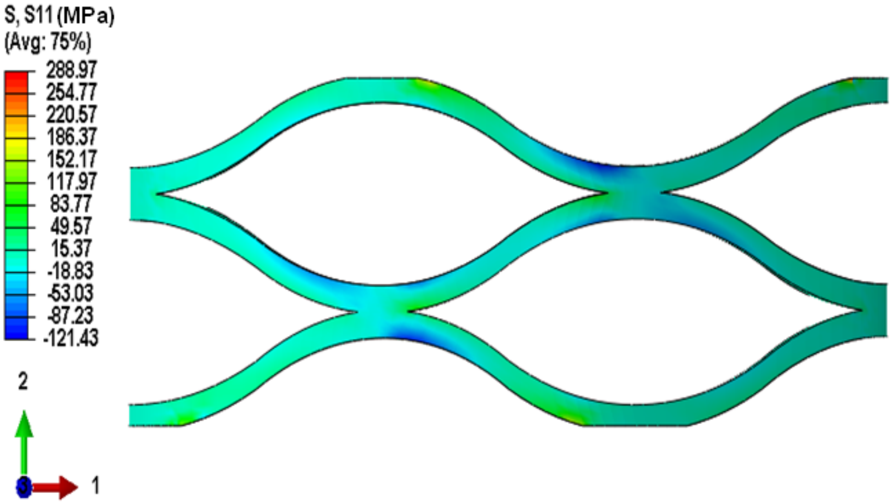

Figure 25.—Distribution of the bending stress, S11 (MPa) in the 55NiTi ($Ni_{49.9}Ti_{50.1}$) wave spring at the end of the loading at 30 °C. Note the variation of the stress magnitude from tension(+ve) to compression(-ve) in the thickness of the collar of the wave spring.

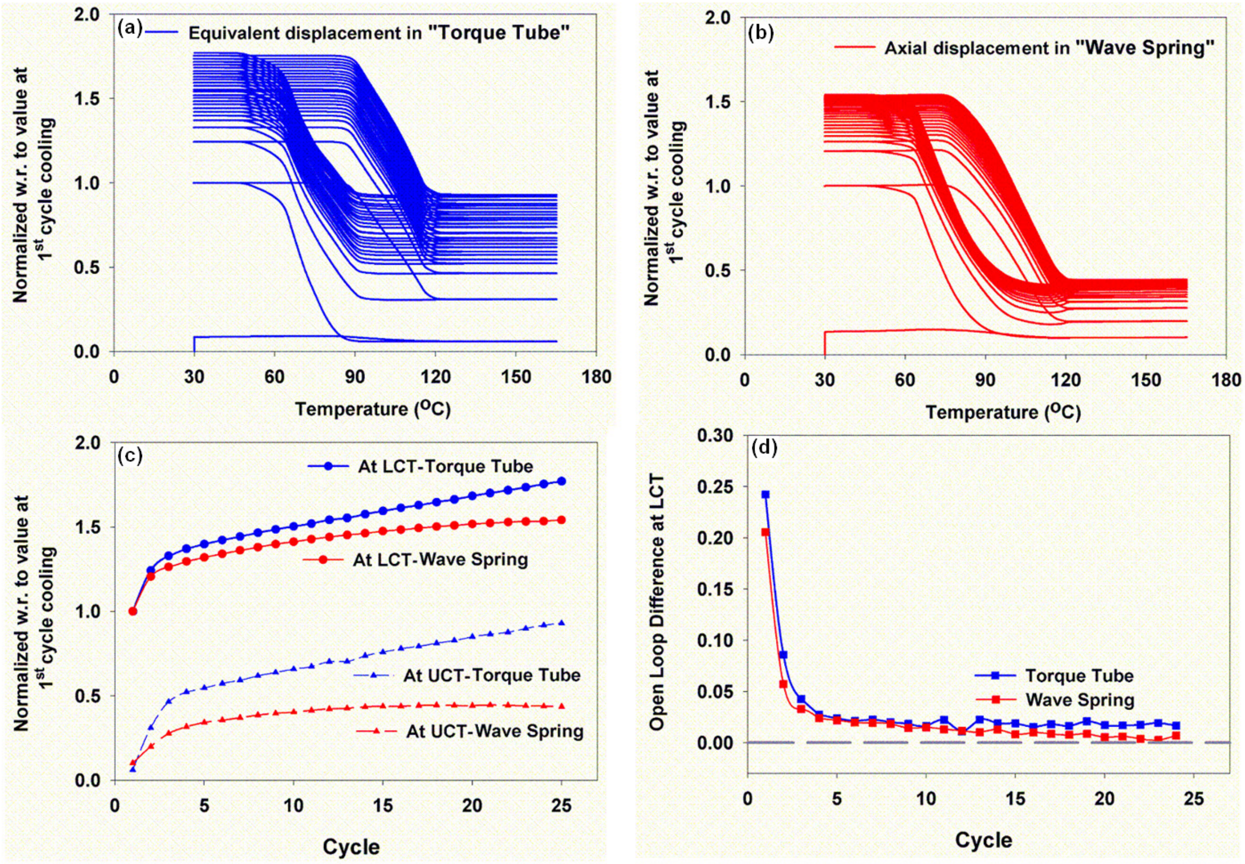

Figure 26.—Isoforce thermal cycling (25 cycles between 30 and 165 °C) test of the 55NiTi torque tube and the 55NiTi wave spring actuator. (a) evolution of the displacement in thermal cycling for 55NiTi torque tube actuators; (b) evolution of the displacement in thermal cycling for 55NiTi wave spring actuators; (c) comparison of the evolution of the displacements at the martensite (LCT=30 °C), austenite(UCT=165 °C) states with cycles for the 55NiTi torque tube and the 55NiTi wave spring actuator ; and (d) comparison of the variation of the open-loop displacement with cycles for the 55NiTi torque tube and the 55NiTi wave spring actuator. Note that the displacements presented here are normalized with respect to the value at the end of 1st cycle cooling.

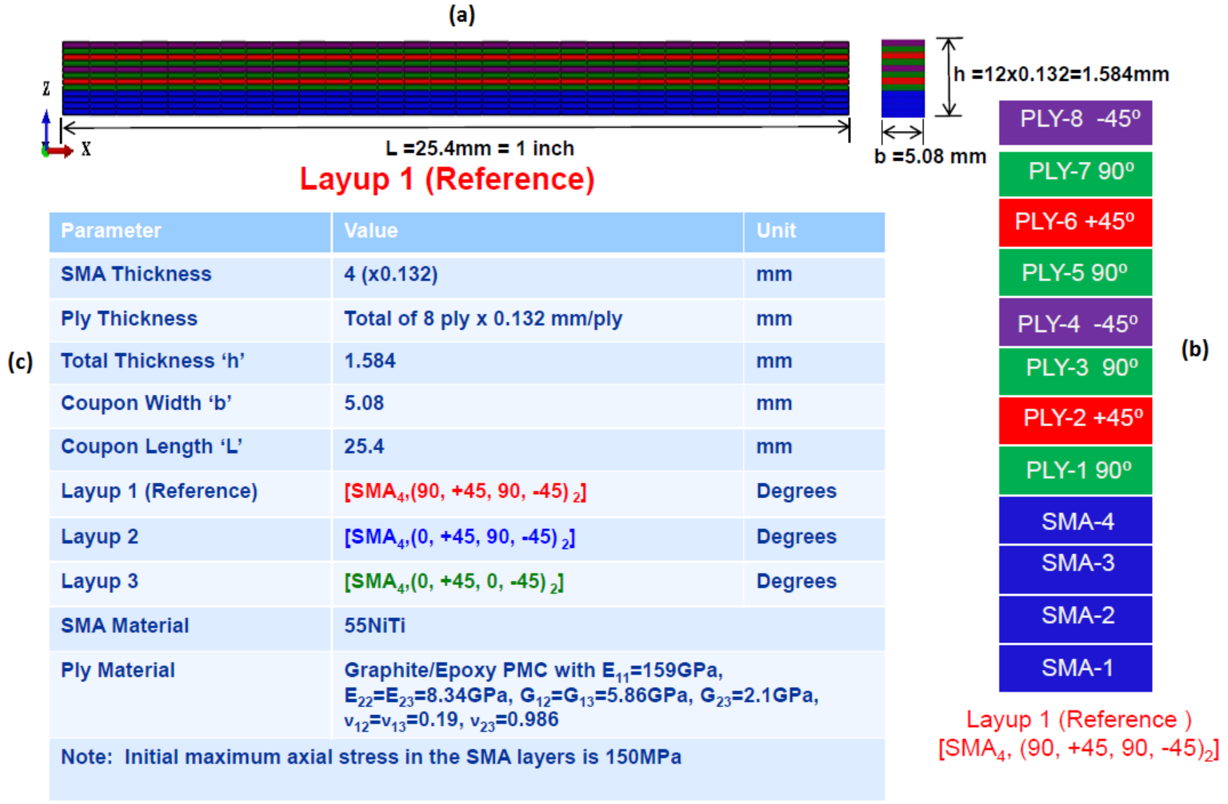

Parameter	Value	Unit
SMA Thickness	4 (x0.132)	mm
Ply Thickness	Total of 8 ply x 0.132 mm/ply	mm
Total Thickness 'h'	1.584	mm
Coupon Width 'b'	5.08	mm
Coupon Length 'L'	25.4	mm
Layup 1 (Reference)	[SMA$_4$,(90, +45, 90, -45) $_2$]	Degrees
Layup 2	[SMA$_4$,(0, +45, 90, -45) $_2$]	Degrees
Layup 3	[SMA$_4$,(0, +45, 0, -45) $_2$]	Degrees
SMA Material	55NiTi	
Ply Material	Graphite/Epoxy PMC with E_{11}=159GPa, E_{22}=E_{23}=8.34GPa, G_{12}=G_{13}=5.86GPa, G_{23}=2.1GPa, ν_{12}=ν_{13}=0.19, ν_{23}=0.986	
Note: Initial maximum axial stress in the SMA layers is 150MPa		

Figure 27.—SMA/Elastic material composite panel (a) Longitudinal dimensions of the panel; (b) the transverse arrangements of the layups (c) the material properties and dimensions of the panel.

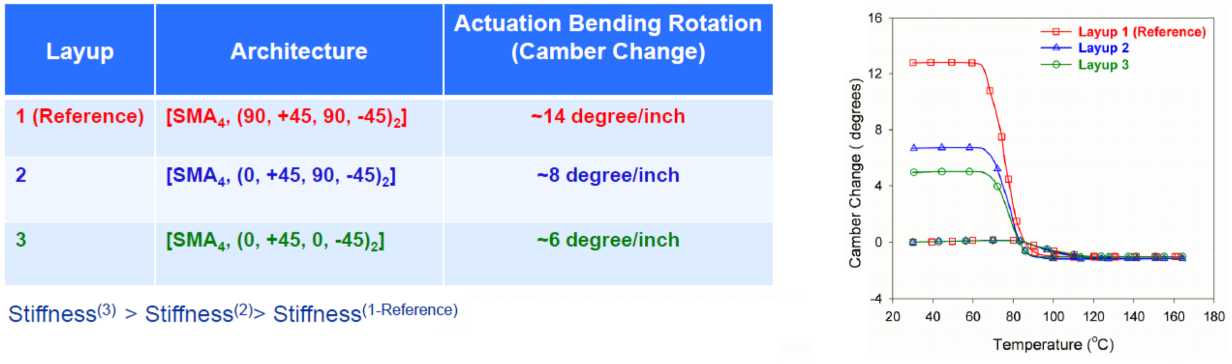

Layup	Architecture	Actuation Bending Rotation (Camber Change)
1 (Reference)	[SMA$_4$, (90, +45, 90, -45)$_2$]	~14 degree/inch
2	[SMA$_4$, (0, +45, 90, -45)$_2$]	~8 degree/inch
3	[SMA$_4$, (0, +45, 0, -45)$_2$]	~6 degree/inch

Stiffness$^{(3)}$ > Stiffness$^{(2)}$> Stiffness$^{(1\text{-Reference})}$

Figure 28.—The variation of camber with temperature for the different layup configurations.

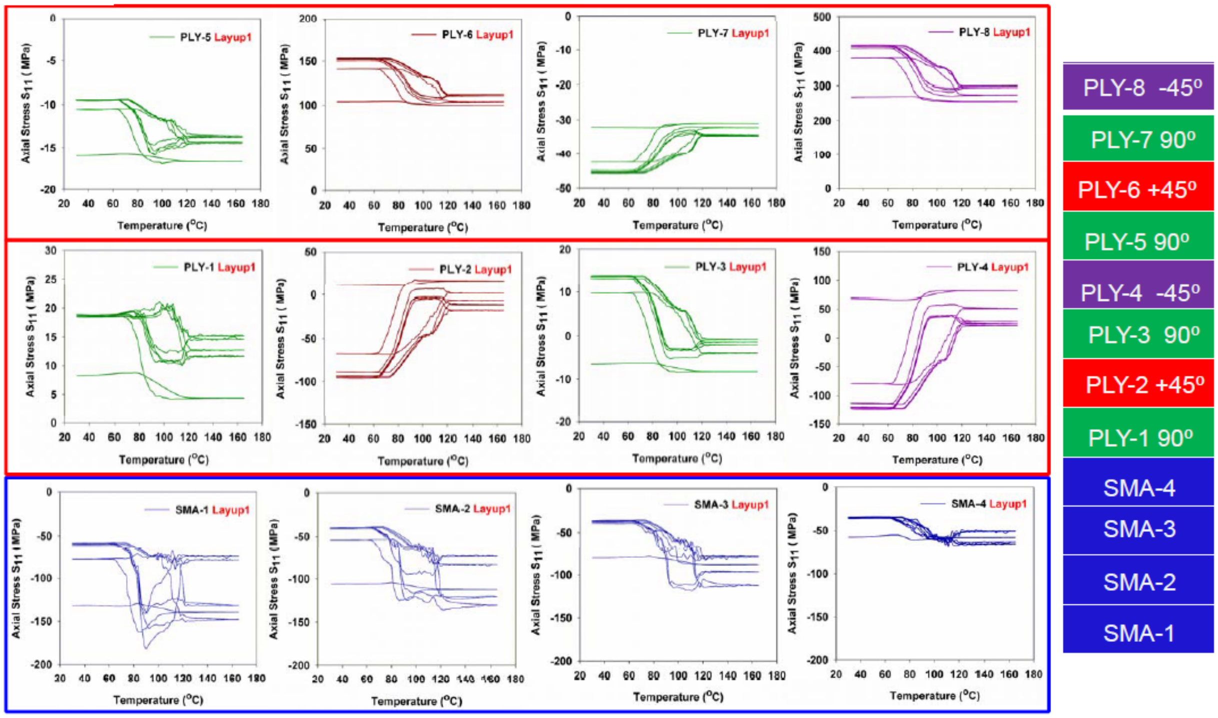

Figure 29.—SMA/Elastic interaction effect, showing the variation of temperature with axial stress for each layup.

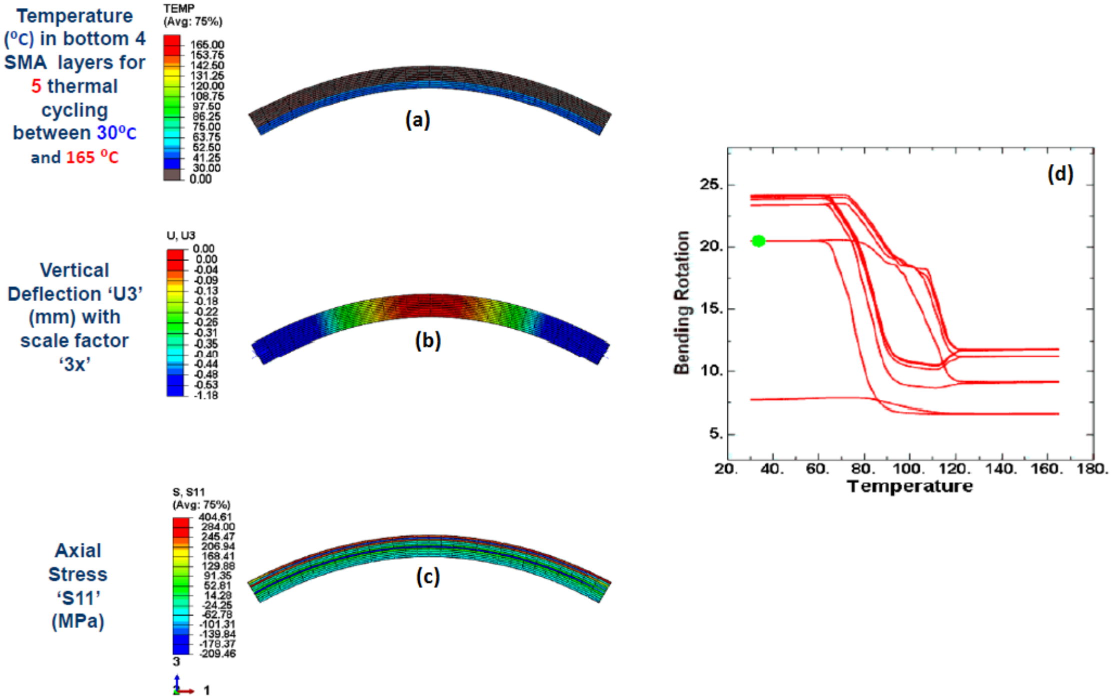

Figure 30.—(a) The variation of temperature within the panel, (b) variation of vertical deflection at the end of 5 cycles (c) the axial stress variation in the composite panel.

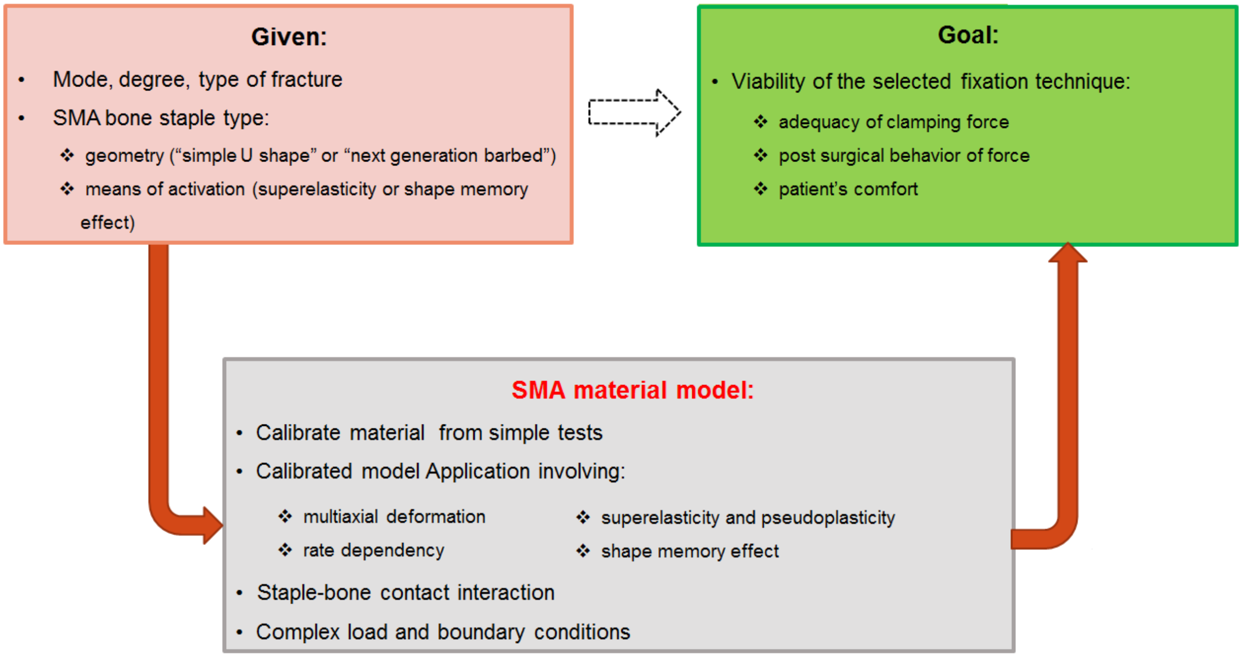

Figure 31.—Flow chart of the overall simulation approach for the SMA stapling surgery.

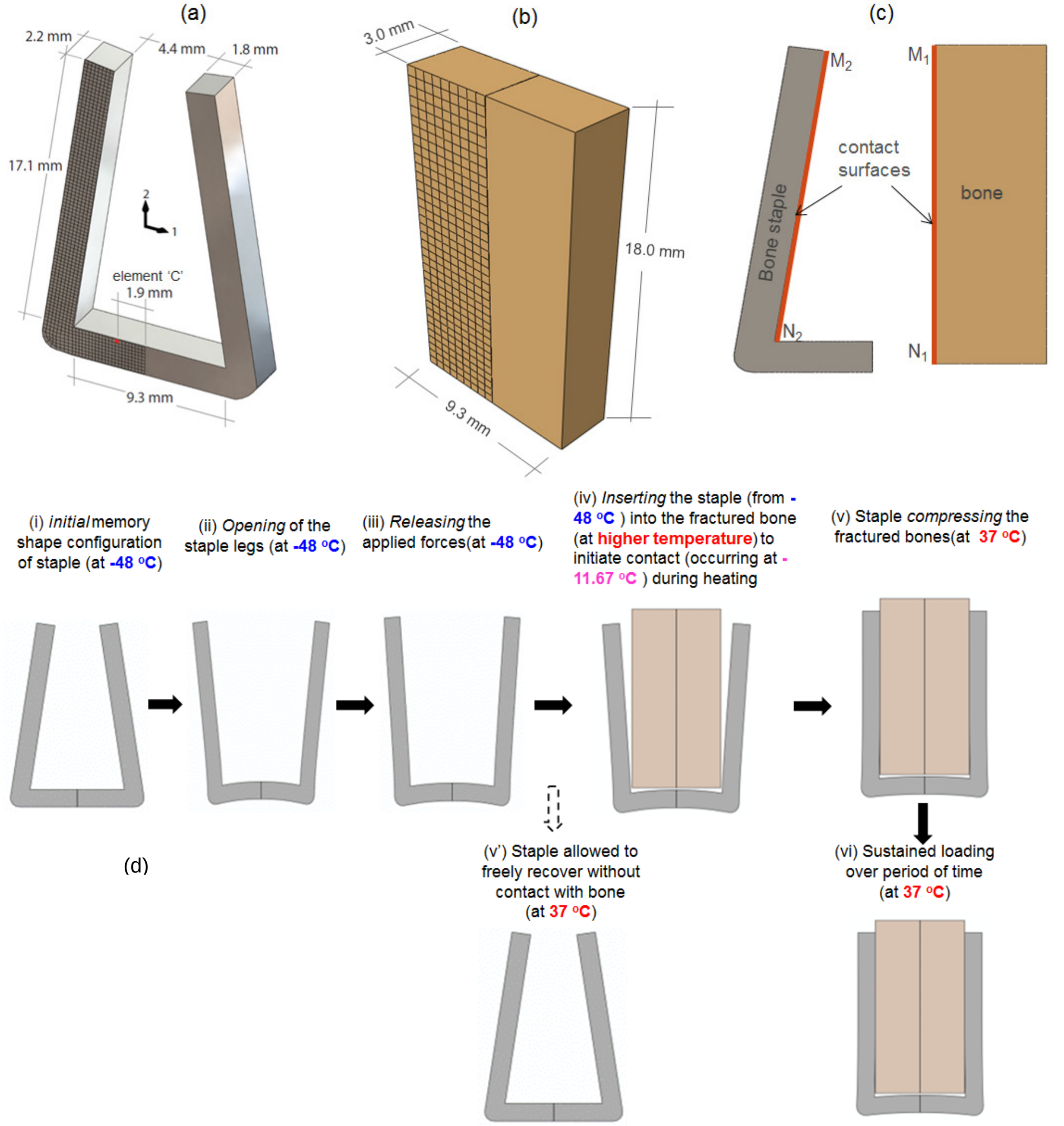

Figure 32.—(a) Details of the bone staple geometry. Element 'C' is located at the top of the staple back at a distance of 1.9 mm from the centerline of the staple, and it was chosen to highlight the significant stress and strain developed in the base of the staple in the different stages of the surgery (b) geometry of the bone, (c) surfaces of the bone (N_1-M_1) that can potentially interact (through frictionless normal contact) with the staple (N_2-M_2) during the thermal activation of the SMA staple and (d) Specifics of the thermo-mechanical controls of the simulated body-temperature-activated SMA stapling procedure

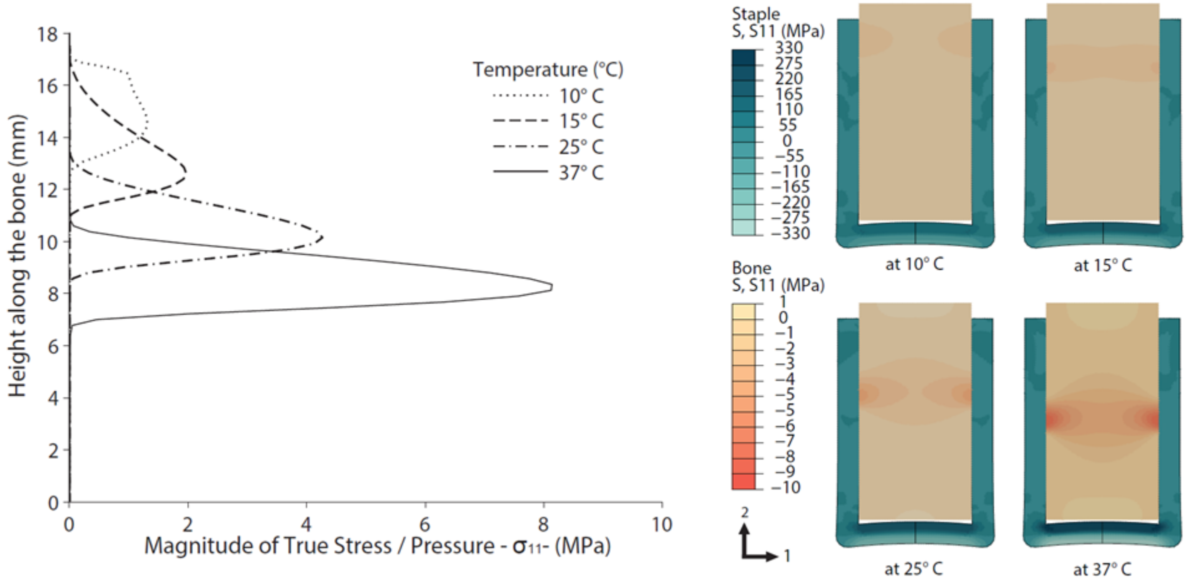

Figure 33.—Transition of the contact stress/pressure (σ_{11}) along the bone height (left) with the distribution of stress contours (σ_{11}) in the 'contact-release' case showing 'constrained- OWSME' for the bone staple (in blue) and bone segment (in tan) at four different temperatures at four different temperatures. To compare with the experimental results, the stress along the bone at 24 °C was integrated to determine the contact force. The model predicts a force of 30.1 N which corresponds well to the experimentally determined force of 33.1 N from Krone et al. (2005).

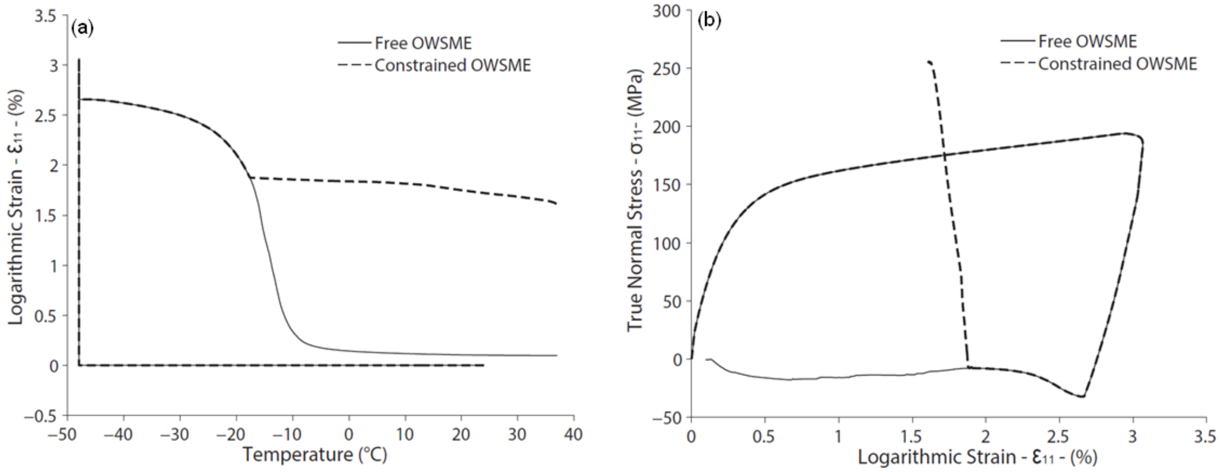

Figure 34.—(a) Logarithmic normal strain (ε_{11})-temperature diagram and (b) True normal stress-logarithmic strain diagram for element 'C' (see Figure 26) comparing the response between the 'free-OWSME' case and the 'constrained- OWSME' case, where the staple clamps into the bone, restricting the full recovery of the NiTi SMA staple. This stress then translates into the contact force at the inserted location in the bone.

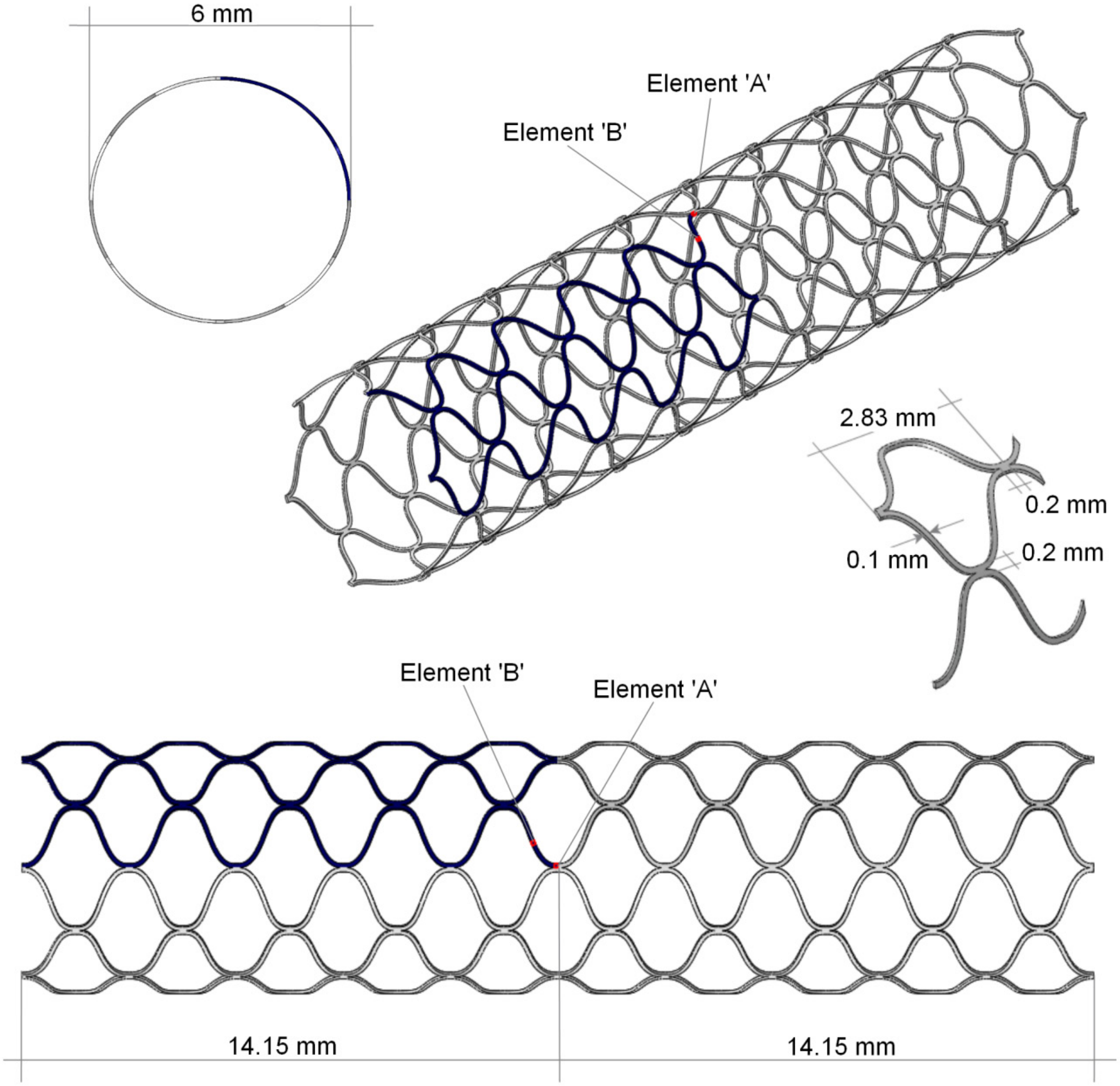

Figure 35.—Geometric details of the memory configuration of the bare-metal, honeycomb stent. Elements ‘A’ and ‘B’ are located at the joint and the mid of the strut near the centerline of the stent and were chosen to highlight the key stress-strain responses in the simulation.

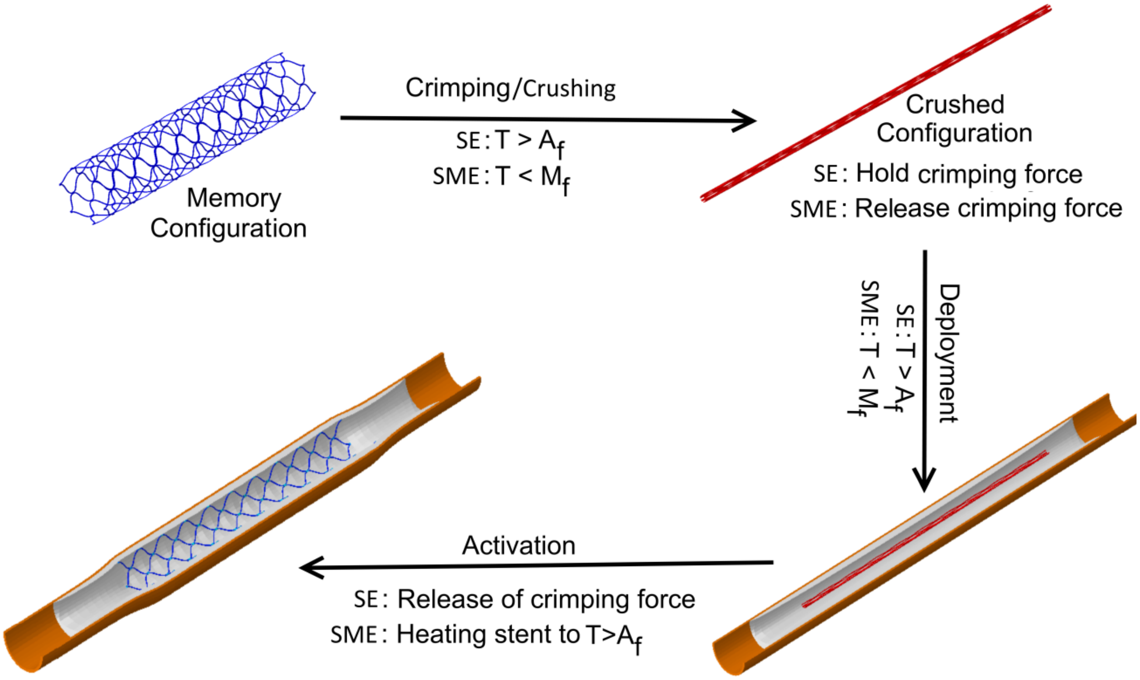

Figure 36.—General schematic showing two alternative schemes of the stenting surgical procedure utilizing Superelasticity or shape memory effect of the self-expanding SMA stent. In this, the following abbreviations are used: ‘SE’ for superelasticity, ‘SME’ for shape memory effect, ‘T’ for Temperature, ‘Af’ for austenite finish temperature, and ‘Mf’ for martensite finish temperature.

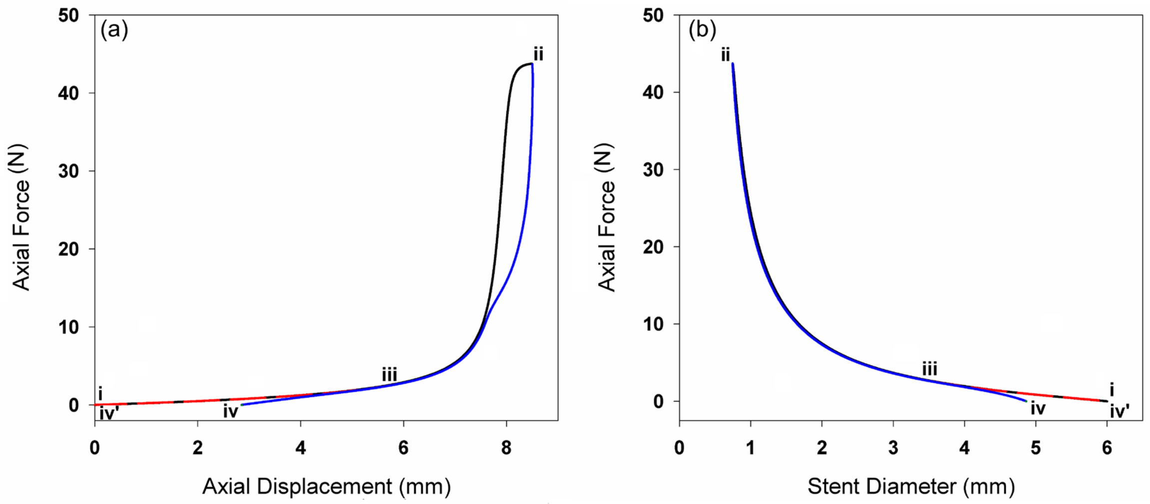

Figure 37.—Case 1 stenting procedure: (a) axial ‘crimping’ force versus axial displacement and (b) axial ‘crimping’ force versus stent diameter at 24 °C.

Spring Used in Modeling

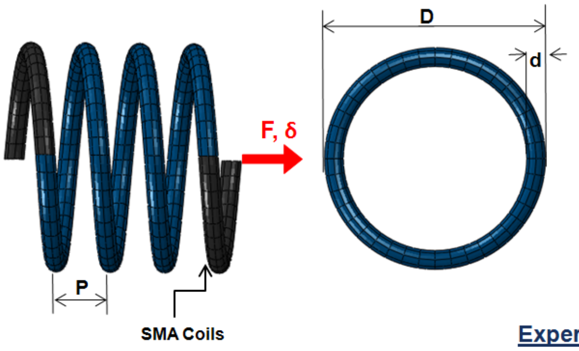

External Coil diameter, D = 25.26 mm
Wire diameter, d= 0.085in =2.16 mm
Mean Coil diameter, D_m = D-d = 23.1mm
Pitch height, P = 6 mm
Pitch angle, α = arctan(P/πD_m) ~ 4.7º
Spring Index, I = D_m/d ~ 10.7
No. of Active coils, n ~ 3
Applied: Iso-force= F=8.8N
Response: Axial Displacement = δ

Spring Used in Experiment

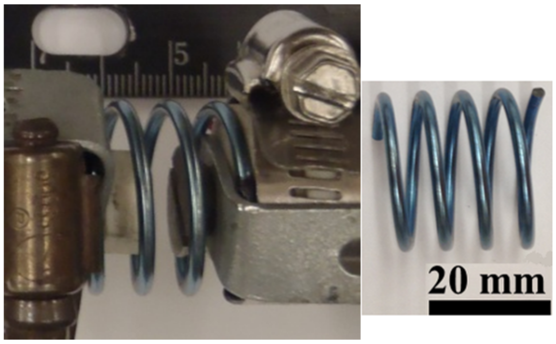

Experimental Procedure:

- ✓ Spring fabricated from $Ni_{49.9}Ti_{50.1}$ EDM wire diameter 2.16 mm
- ✓ Springs shape set at 450°C for 30 min and then furnace cooled
- ✓ Two no-load thermal cycles were performed after the springs were installed into the setup
- ✓ 10 load-bias cycled (spring ends rotationally constrained) were performed with following parameters:
  Load = 8.8 N→ Initial Effective Stress (calculated) =100 MPa
  Initial Displacement (result) = 7.2 mm
  LCT=35ºC
  UCT=165ºC
  Initial Moment = 0 N·mm3.

Figure 38.—Geometric and loading details of SMA helical spring used in experimental validation of SMA Model response (Experiment was conducted at University of Central Florida).

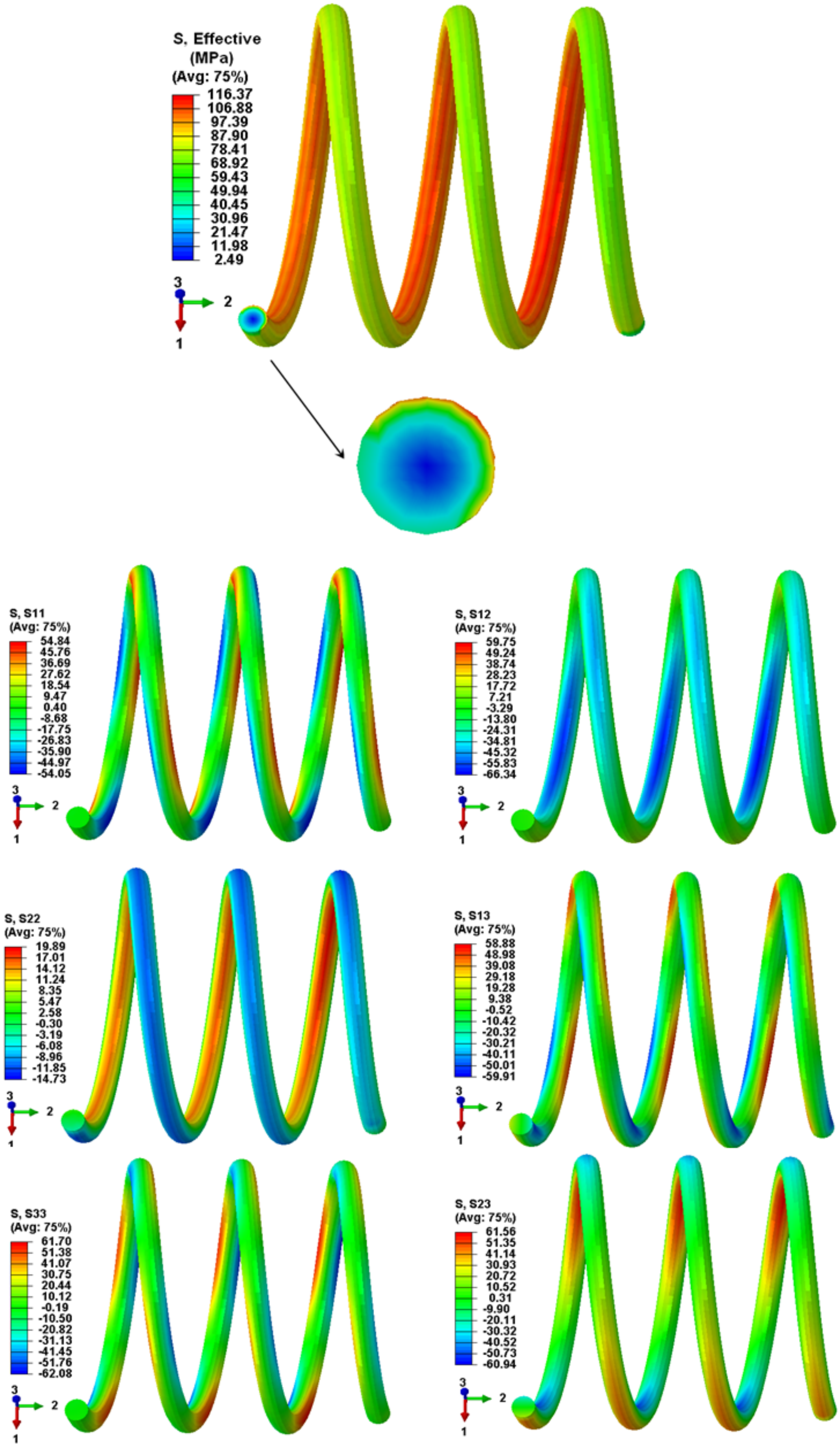

Figure 39.—Distribution of effective stress and the component of the stress state in SMA coils at the end of load up. Note that this demonstrates a significant nonuniformity/ inhomogeneity in different parts of the coils, and especially over the cross section of the wire and the three-dimensionality of the stress state.

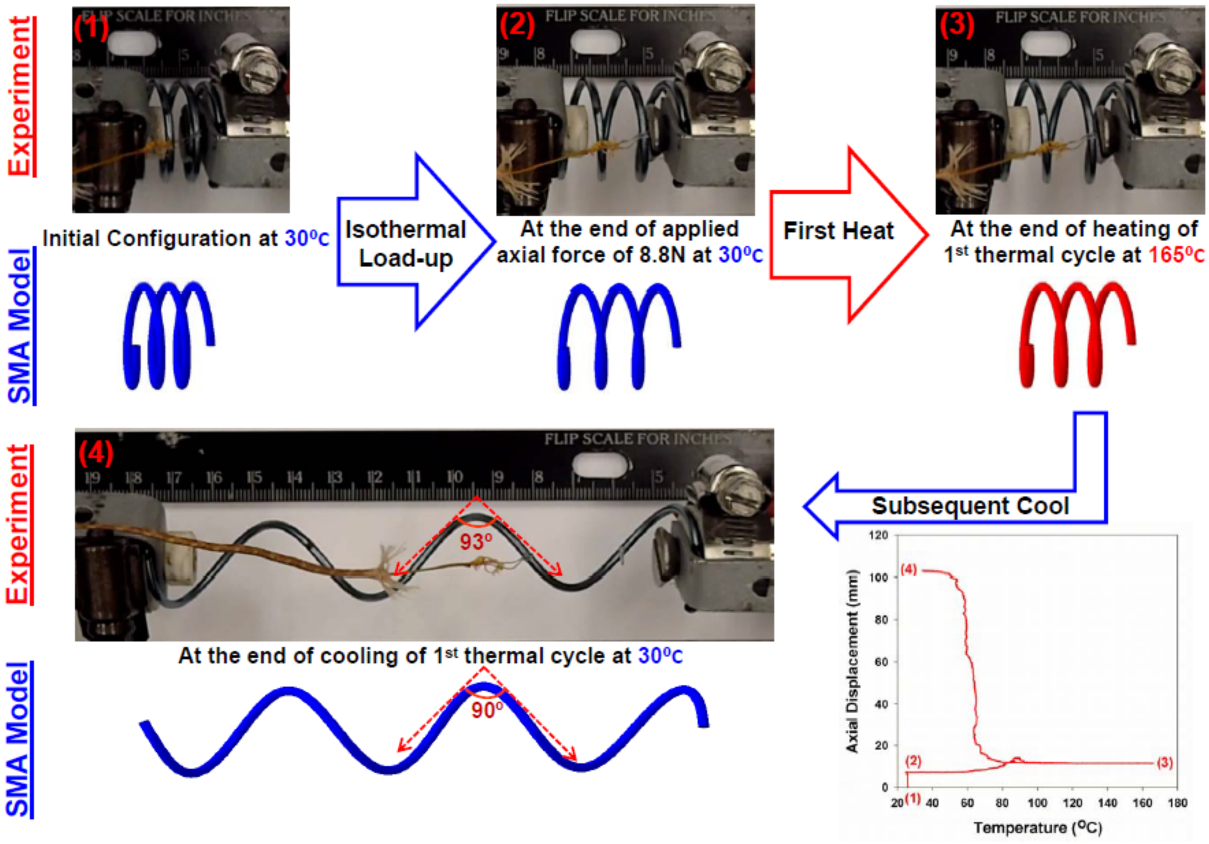

Figure 40.—Experimental and simulated evolutionary deformation response for the helical-coil actuator from: (1) initial undeformed configuration at 30 °C → (2) deformed configuration at the end of isothermal load-up at 30 °C→ (3) deformed configuration at the austenite state (165 °C) at end of 1st heat → (4) deformed configuration at the martensite state (30 °C) at the end of subsequent cool.

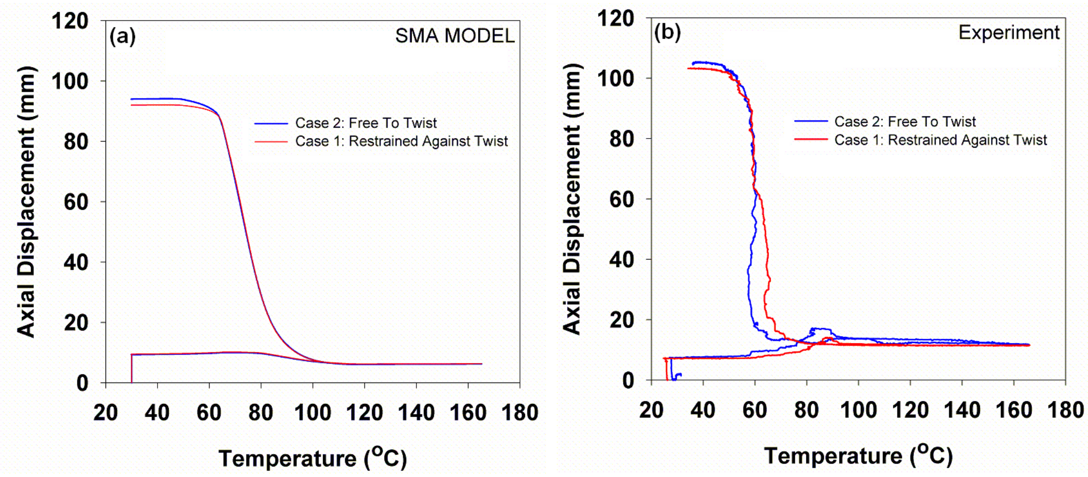

Figure 41.—Axial Displacement versus temperature response for the transient deformation of Case (1) and Case (2) (see text for details): (a) SMA Model and (b) experiment.

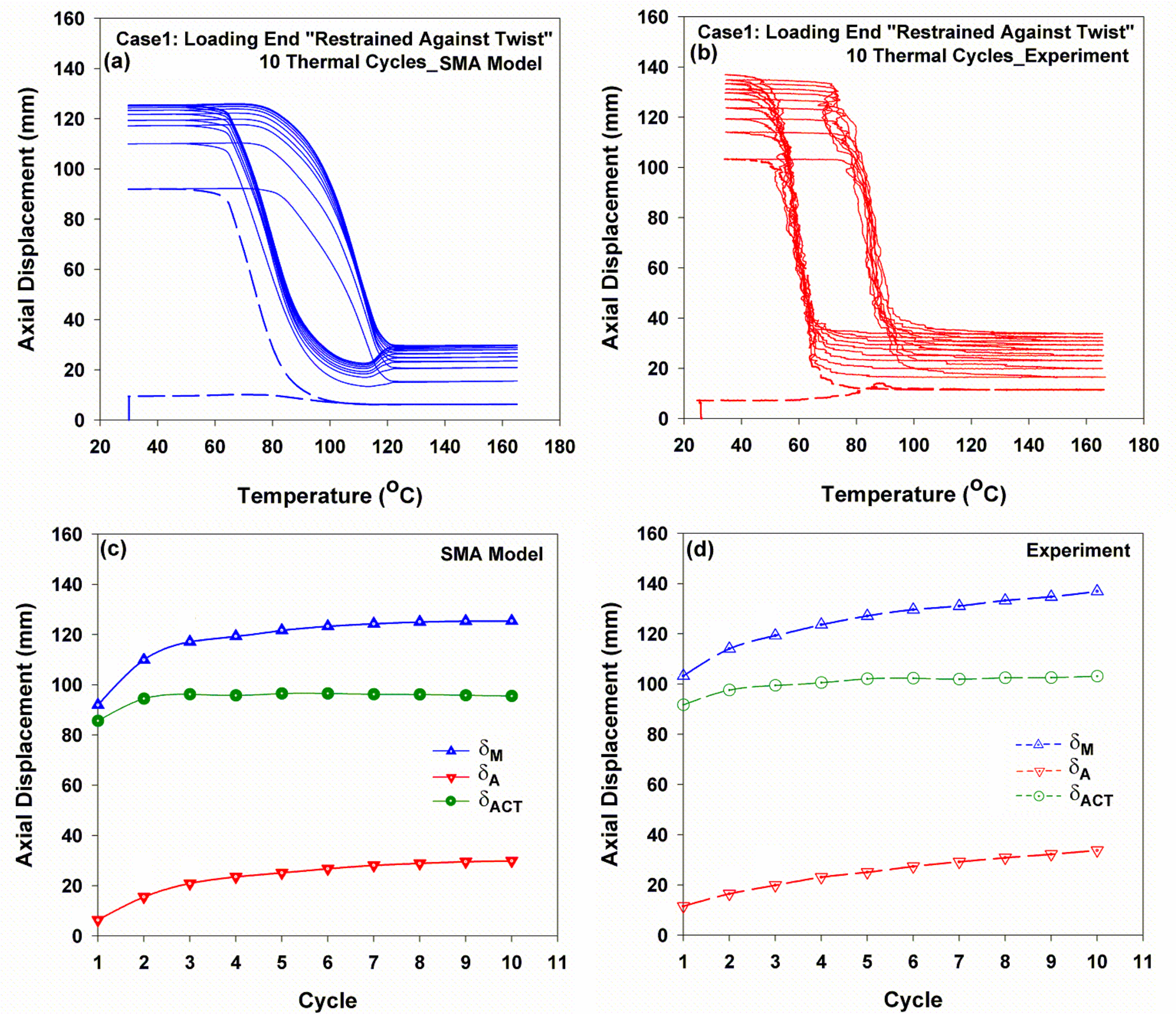

Figure 42.—The axial displacement versus temperature response and summary of axial displacements at the martensite, austenite states, and corresponding actuation displacement “stroke” in Case (1) for 10 thermal cycles: (a), (c) SMA Model and (b), (d) Experiment, respectively.

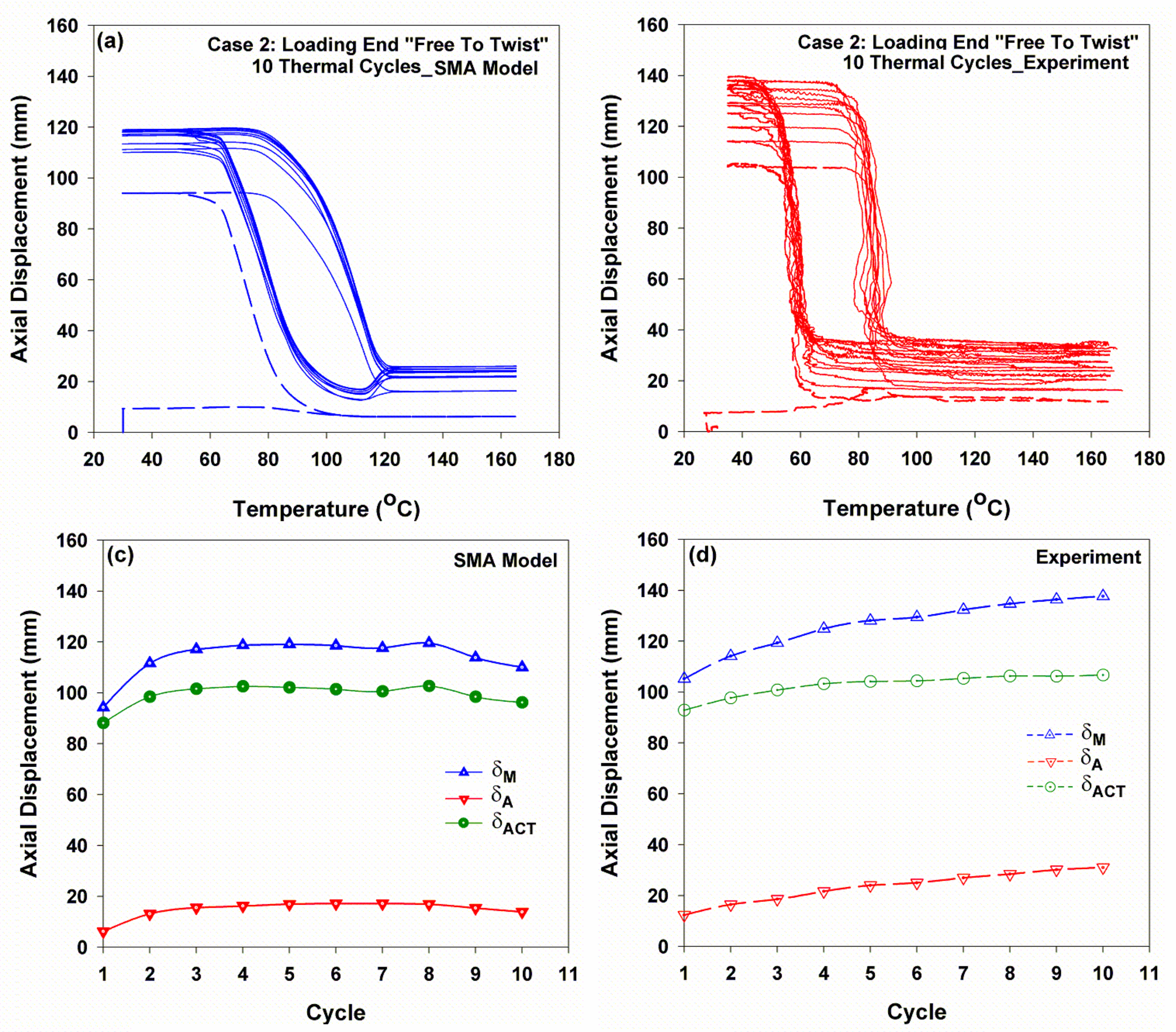

Figure 43.—The axial displacement versus temperature response and summary of axial displacements at the martensite, austenite states, and corresponding actuation displacement “stroke” in Case (2) for 10 thermal cycles: (a), (c) SMA Model and (b), (d) Experiment, respectively.

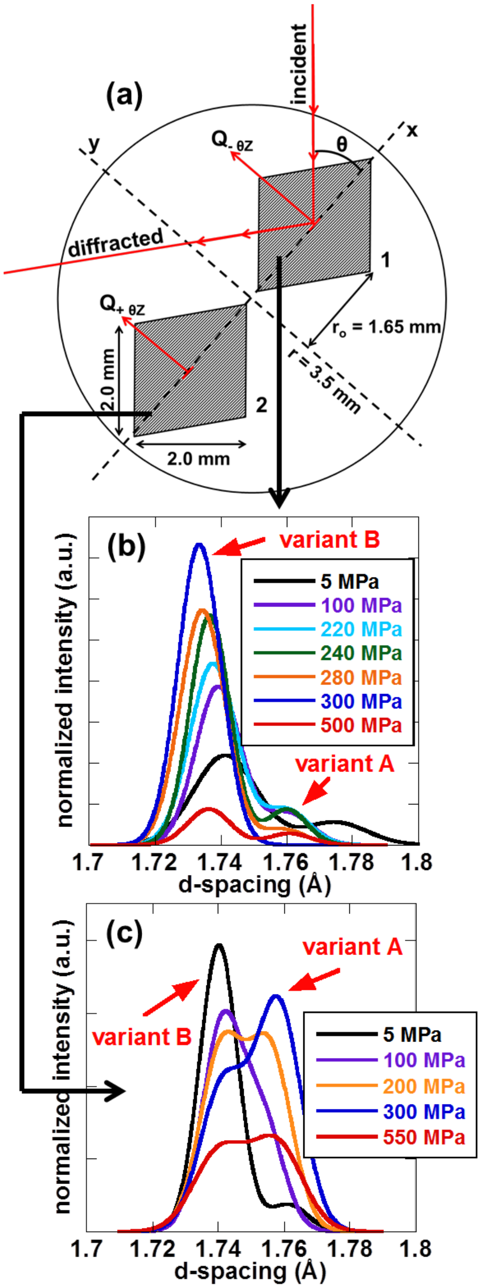

Figure 44.—Neutron diffraction of principle stress directions under pure torsional loading at room temperature: (a) cross-section of cylindrical specimens and the cross-section of the two diffraction gauge volumes. The load frame was tilted to 43° (about the x-axis) to produce reflections from lattice planes near perpendicular to the directions of maximum (location 1, $Q_{-\theta z}$) and minimum (location 2, $Q_{+\theta z}$) normal stress. Also, shown are the corresponding sections of normalized neutron diffraction spectra acquired from (b) location 1 and (c) location 2. All stress values shown represent the applied shear stress at the surface the specimen.

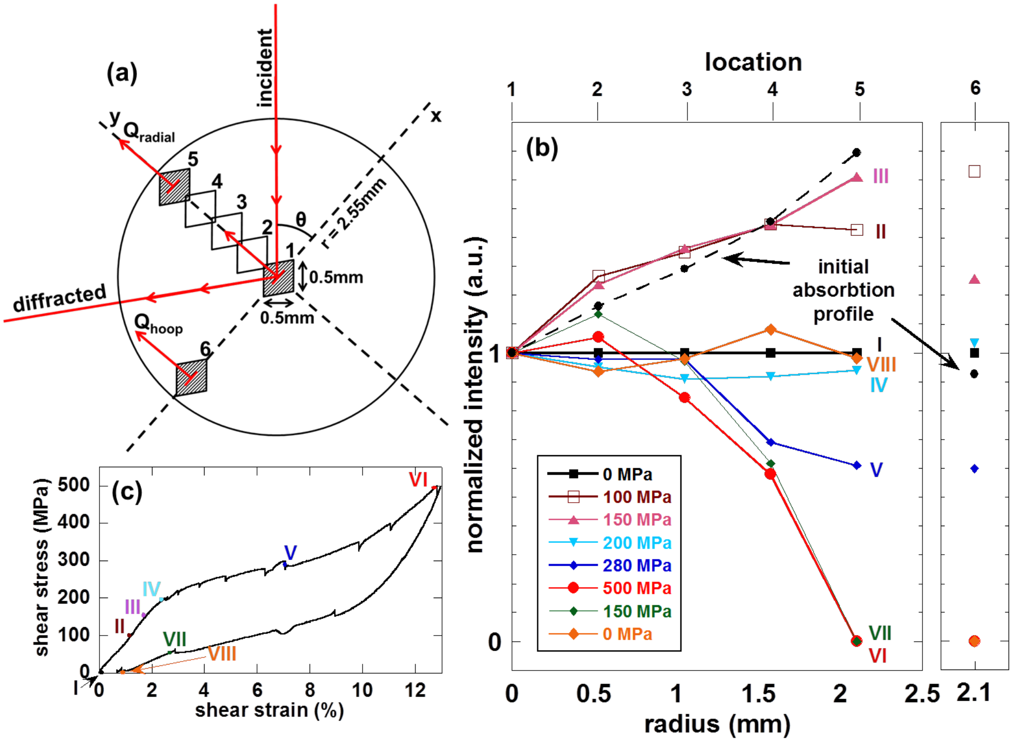

Figure 45.—Neutron diffraction of radial and hoop directions under pure torsional loading at room temperature: (a) cross-section of the cylindrical specimen showing outlines of the six diffraction gauge volumes within the cylinder. The load frame was positioned vertical to produce reflections from lattice planes perpendicular to the radial (location 1-5, Q_{radial}) and hoop (location 6, Q_{hoop}) directions of the specimen. (b) Normalized intensity of variant B (w.r.t. $<111>_A$ austenite) as function of the radial (mm) distance from the center of the sample to the centroid of the diffraction volumes. (c) The macroscopic stress-strain response (stresses for which neutron data is presented are labeled I-VIII). All stress values shown represent the applied shear stress at the surface the specimen.

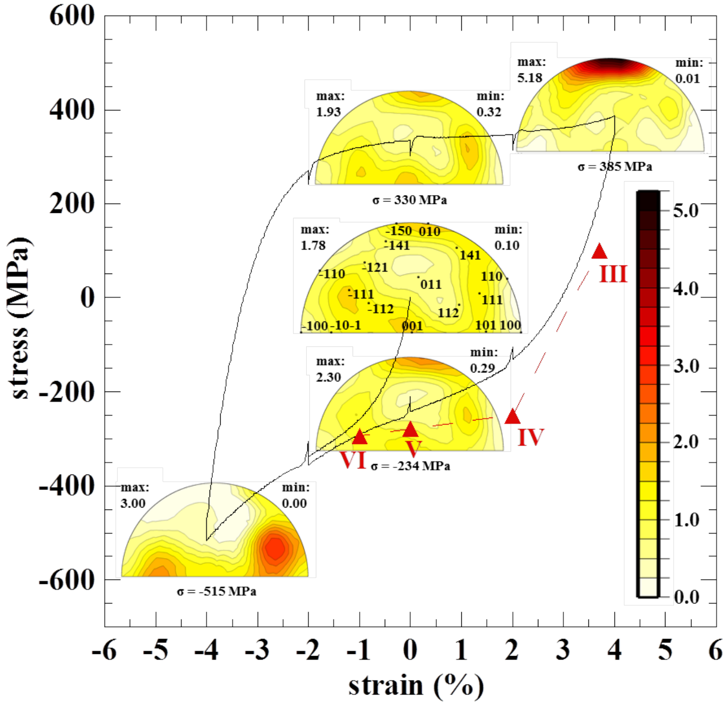

Figure 46.—Inverse pole figures (IPFs) for the loading direction and corresponding macroscopic response of B19′ martensitic NiTi under isothermal compressive followed by tensile, then compressive reverse loading (as shown by the solid black line). Also shown are the macroscopic positions of Points III-VI of Figure 45 (as indicated by ▲). For clarity in presentation, the scale chosen is unique to this figure.

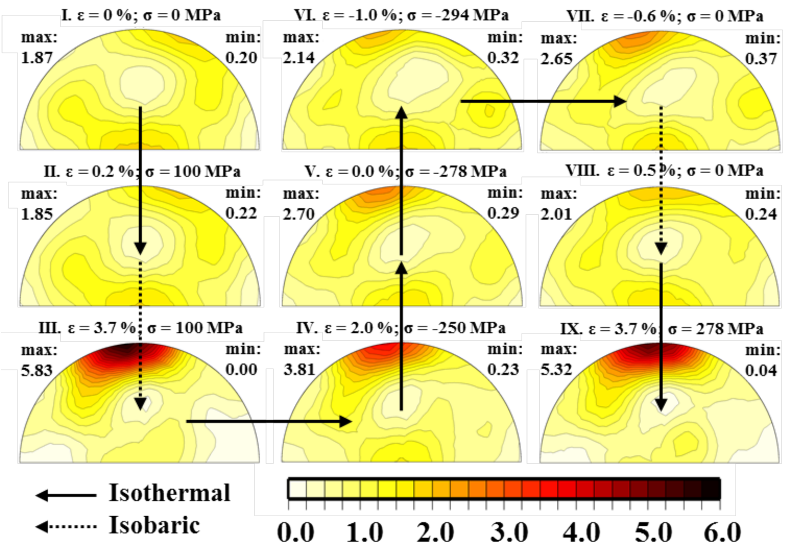

Figure 47.—Inverse pole figures (IPFs) for the loading direction corresponding to mixed isothermal (indicated by solid arrows) and isobaric (indicated by dashed arrows) loading in the same experiment. During isobaric loading the sample was thermally cycled to temperatures above and below the room temperature, once from Points II to III and twice from Points VII to VIII. The corresponding macroscopic position is given above each IPF. For clarity in presentation, the scale chosen is unique to this figure.

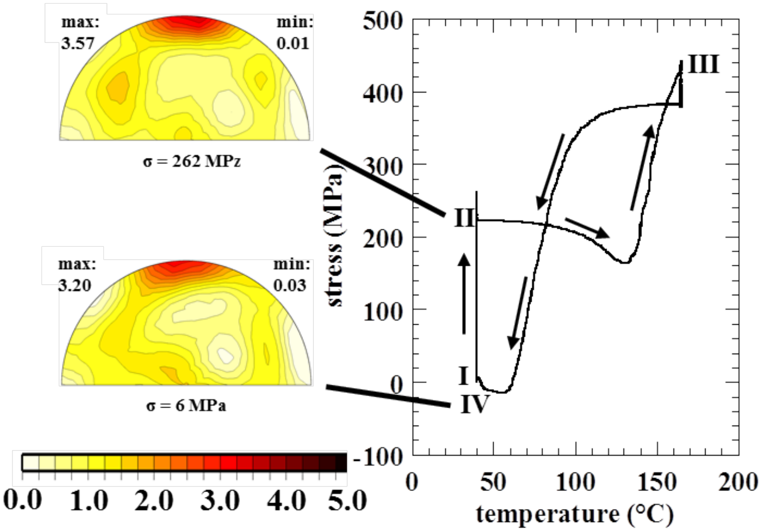

Figure 48.—Inverse pole figures (IPFs) for the loading direction and corresponding macroscopic response of B19′ martensitic NiTi at before (Point II) and after (Point IV) one thermal cycle to temperatures above and below the phase transformation under a constant strain of 2%. For clarity in presentation, the scale chosen is unique to this figure.

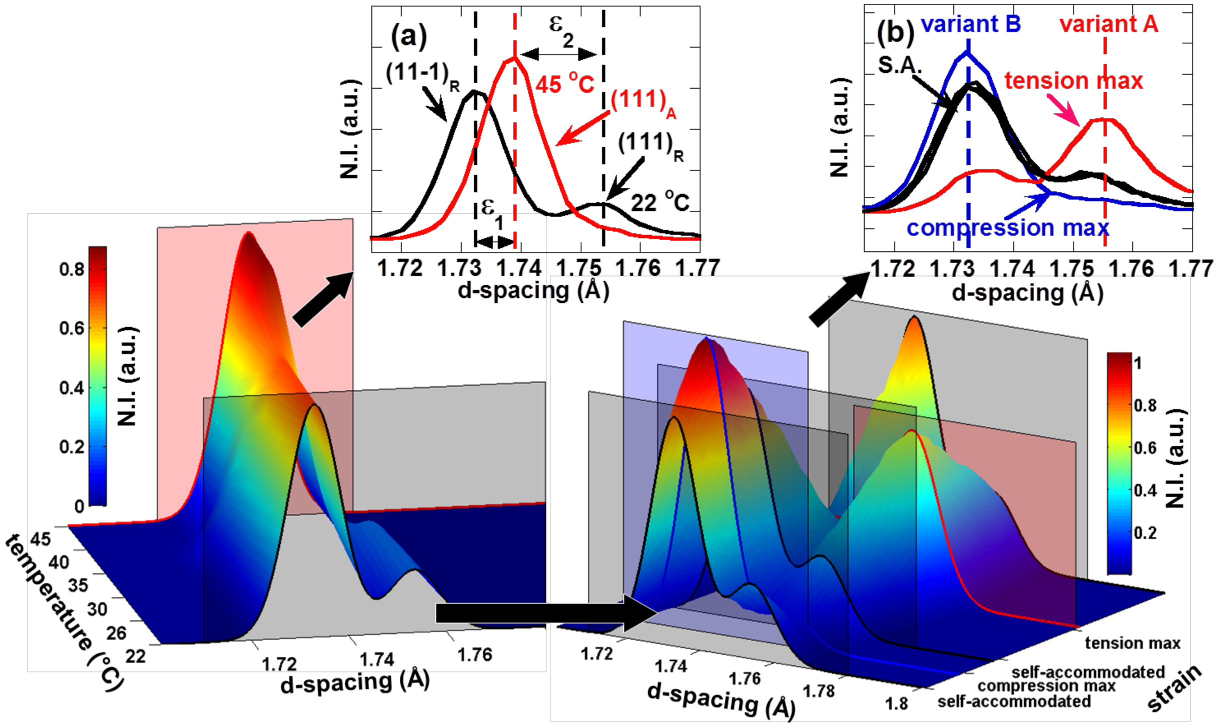

Figure 49.—Section of normalized neutron diffraction spectra acquired during a) isobaric cooling from cubic austenite (B2) to trigonal R-phase under no stress and b) isothermal uniaxial tension-compression reverse cyclic loading of trigonal R-phase at room temperature in NiTi. Red and black planes/lines indicate cubic austenite and trigonal R-phase, respectively, in a). Black, blue and red planes/lines indicate self-accommodated (–0.175%), maximum compressive (-0.5%) and maximum tensile (0.5%) strain, respectively, in b). Reflections are from crystallographic planes perpendicular to the length of the sample.

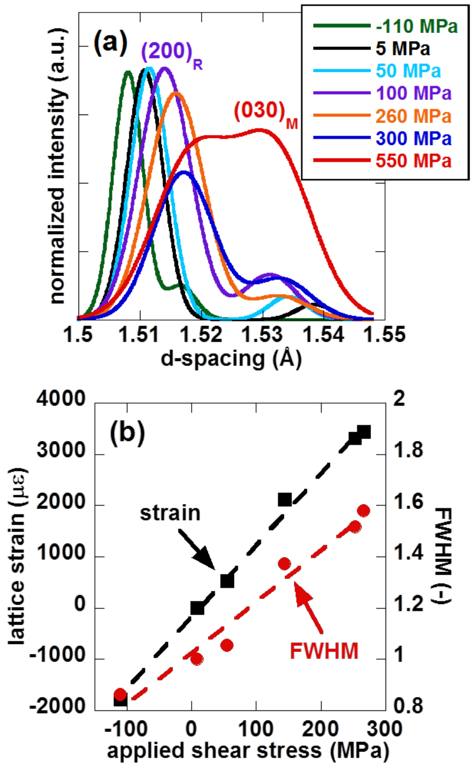

Figure 50.—(a) An additional section of normalized neutron diffraction spectra acquired from location 1 in Figure 5(a) under pure torsional loading at room temperature. (b) Strains (indicated by ■) and Full Width at Half Maximum (FWHM, indicated by ●) determined from changes in d-spacing and peak breadth, respectively, of the $(200)_R$ peaks shown in (a)). All stress values shown represent the applied shear stress at the surface the specimen.

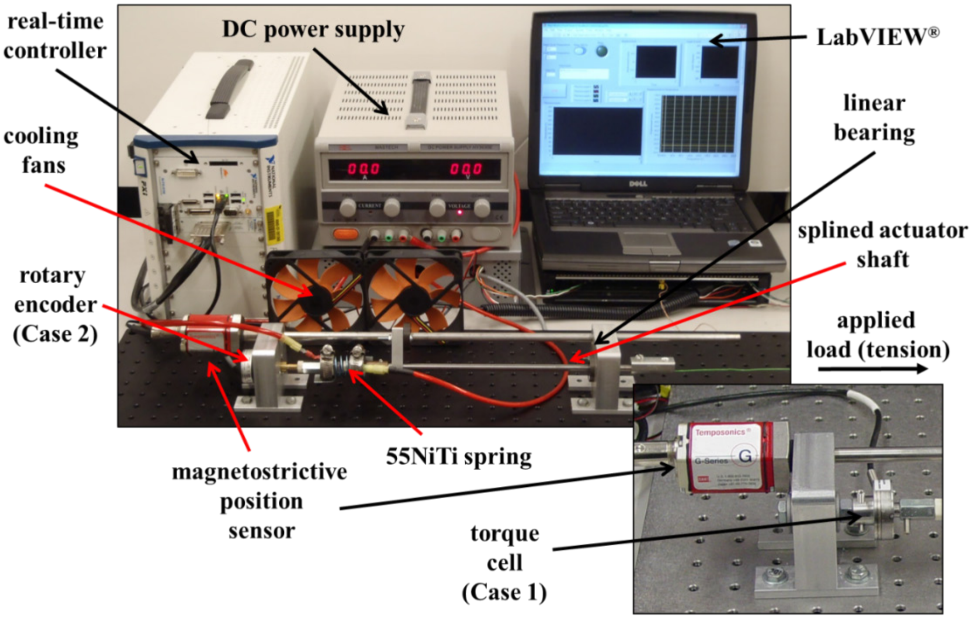

Figure 51.—Modular experimental setup for thermomechanical testing of 55NiTi shape memory alloy helical-coil actuators. Configurations are shown for case (1) and case (2).

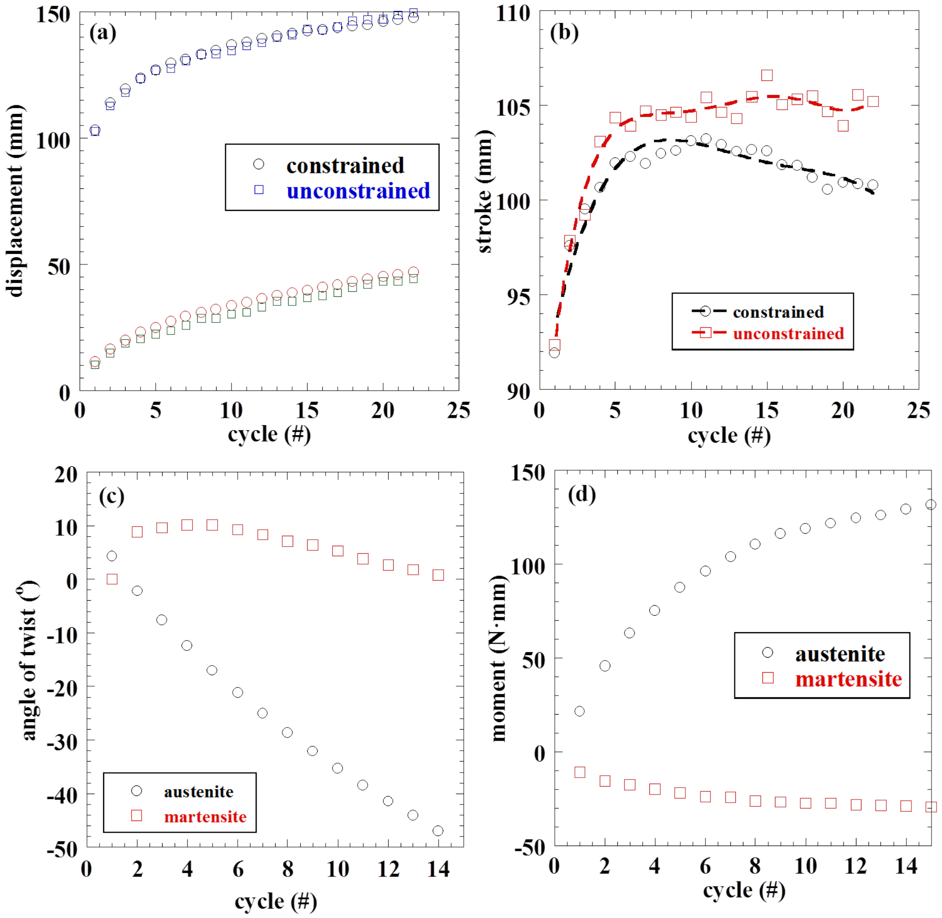

Figure 52.—Thermal cycling of a 55NiTi spring actuator under 8.8 N. Comparison of the cases in which the ends of the spring are rotationally constrained and unconstrained: (a) displacement versus cycle for austenite and martensite; and (b) actuation displacement (stroke) versus cycle. The secondary responses are also shown: (c) angle of twist versus cycle for the rotationally unconstrained; and (d) moment versus cycle for the rotationally constrained.